Republic of Iraq
Ministry of Higher Education and Scientific Research
University of Al-Qadisiyah
College of Science
Department of Chemistry

Synthesis and Characterization of Novel Transition Metal Oxide-Nitride Perovskites for Solar Cell Applications

A Thesis

Submitted to the College of Sciences – University of Al-Qadisiyah in Partial Fulfillment of the Requirements for the Degree of Master of Science in Chemistry

By

Zahraa Ali Rahman

(BSc. Chemistry, 2021)

Supervised by

Prof. Dr. Ahmed Kadhim Al-Saffar

1448 A.H. **2026 A.D.**

بِسْمِ اللَّهِ الرَّحْمَنِ الرَّحِيمِ

﴿أَلَمْ تَرَوْا كَيْفَ خَلَقَ اللَّهُ سَبْعَ سَمَاوَاتٍ طِبَاقًا ﴿١٥﴾ وَجَعَلَ

الْقَمَرَ فِيهِنَّ نُورًا ﴿١٦﴾ وَجَعَلَ الشَّمْسَ سِرَاجًا ﴿١٧﴾﴾

صدق الله العظيم

سورة نوح، الآيات (١٥–١٧)

Dedication

To the memory of my beloved mother, whose soul and prayers remain my guiding light.

To my dear father, without whose tireless efforts, hard work, and sacrifices I would not have reached where I am today.

To my dear sisters and brother, for their love, encouragement, and for always being by my side.

To my stepmother, for her kindness, care, and continuous support throughout my journey.

To my dear friends, for their companionship, motivation, and unforgettable moments.

I dedicate this humble work to all of you with heartfelt love and gratitude.



Zahraa Ali Rahman

Acknowledgments

First and foremost, I would like to thank Allah Almighty for granting me the strength, patience, and ability to complete this work.

I express my deepest gratitude to my loving family for their continuous prayers, endless support, and constant encouragement throughout my academic journey.

I would like to express my sincere appreciation to my supervisor, **Prof. Dr. Ahmed Kadhim Al-Saffar**, for his valuable guidance, continuous support, constructive suggestions, and scientific advice throughout the course of this research. His encouragement, patience, and insightful comments have been invaluable in the completion of this thesis.

My sincere thanks are also extended to the Deanship of the College of Science at the University of Al-Qadisiyah, and particularly to the Head of the Chemistry Department, **Prof. Dr. Bassam Faron Abed**, for his support, kindness, and understanding during a difficult time, which helped me overcome those challenges and continue my path.

I am deeply grateful to all members of the Department of Chemistry for their cooperation and support during my study.

Special thanks go to my colleague, Mr. Ali, for his helpful assistance whenever needed, and to my dear friends for their moral support and for always standing by my side.

Finally, I would like to express my gratitude to all my peers and to everyone who supported me, directly or indirectly, and contributed in any way to the completion of this thesis.

SUMMARY

This study investigated the synthesis and characterization of twelve transition-metal oxynitride nanomaterials based on Ba, Ca, Mg, and Pb at the A-site, with Cu, Co, or equimolar Cu/Co at the B-site, using the sol–gel method. The materials were characterized by X-ray diffraction (XRD), field-emission scanning electron microscopy coupled with energy-dispersive X-ray spectroscopy (FESEM–EDS), atomic force microscopy (AFM), Fourier-transform infrared spectroscopy (FTIR), ultraviolet–visible spectroscopy (UV–Vis), thermogravimetric analysis coupled with differential thermogravimetric analysis (TGA/DTG), Hall-effect measurements, and current density–voltage (J–V) measurements. The results showed that the structural, morphological, optical, thermal, electrical, and photovoltaic properties were strongly affected by the A-site and B-site compositions. XRD revealed the highest crystallinity for $PbCoO_2N$ (88.81%) and the lowest for $BaCu_{0.5}Co_{0.5}O_2N$ (64.1%), with nanoscale particle sizes. UV–Vis analysis showed band gaps of 1.63–3.25 eV, while TGA/DTG revealed composition-dependent thermal behaviour, with the highest activation energy for $MgCuO_2N$ (362.19 kJ/mol). Hall-effect measurements confirmed p-type behaviour; $BaCoO_2N$ showed the highest electrical conductivity (8.05 $S \cdot cm^{-1}$), whereas $MgCu_{0.5}Co_{0.5}O_2N$ exhibited the highest carrier mobility (4.85×10^3 $cm^2 \cdot V^{-1} \cdot s^{-1}$). Photovoltaic measurements showed efficiencies of 8.44–15.77%. $BaCoO_2N$ achieved the highest efficiency (15.77%) and high electrical conductivity, making it the most favourable material for the investigated photovoltaic application, whereas $MgCu_{0.5}Co_{0.5}O_2N$ showed the lowest efficiency (8.44%) and short-circuit current density (11.83 mA/cm^2). $PbCu_{0.5}Co_{0.5}O_2N$ also showed high photovoltaic performance, with an efficiency of 15.08%. Overall, the results demonstrate that controlling the A-site cation and Cu/Co composition at the B-site effectively tunes the properties and photovoltaic performance of transition-metal oxynitride nanomaterials.

Table of Contents

Number	Subject	Page NO.
	Summary	I
	Table of Contents	II
	List of Figures	V
	List of Tables	VII
	List of Characters and Abbreviations	IX
Chapter One		
1	Introduction	1
1.1	Solar Cells	2
1.1.1	Solar Cell Generations	3
1.1.2	Perovskite Solar Cells (PSCs)	4
1.2	Nanomaterials	5
1.2.1	Nanomaterials Classifications	6
1.2.1.1	Dimensional-based Nanomaterials	6
1.2.1.2	Material-based Nanomaterials	8
1.3	Synthesis Methods of Nanomaterials	10
1.4	Semiconductors	12
1.4.1	Intrinsic Semiconductors	13
1.4.2	Extrinsic Semiconductors	13
1.5	Crystalline Semiconductors	14
1.5.1	Single Crystal Semiconductors	14
1.5.2	Polycrystalline Semiconductors	15
1.6	Copper-based Perovskites	15
1.7	Cobalt-based Perovskites	15
1.8	Characterization Techniques of Semiconductors	16
1.8.1	Principles of X-ray Diffraction (XRD)	16
1.9	Morphological Properties	17
1.9.1	Field Emission Scanning Electron Microscopy (FESEM)	17
1.9.2	Energy-Dispersive X-ray Spectroscopy (EDS)	17
1.9.3	Atomic Force Microscopy (AFM)	18
1.10	Hall Effect	18
1.11	Literature Survey	19
1.12	Aims of the Research	24

Chapter Two		
2	Experimental Methodology	26
2.1	Chemicals used	26
2.2	Instruments	27
2.3	Preparation of Oxynitride Nanoparticles by Sol–gel method	28
2.3.1	Ba-Based Oxynitride Perovskites	28
2.3.2	Ca-Based Oxynitride Perovskites	29
2.3.3	Mg-Based Oxynitride Perovskites	30
2.3.4	Pb--Based Oxynitride Perovskites	31
2.4	Thin Film Deposition and Hall Effect Measurements	33
Chapter Three: Results and Discussion		
3	Results and Discussion	37
3.1	Structural and Microstructural Analysis	37
3.1.1	X-ray Diffraction of Ba-based Oxynitride Perovskites	37
3.1.2	X-ray Diffraction of Ca-based Oxynitride Perovskites	41
3.1.3	X-ray Diffraction of Mg-based Oxynitride Perovskites	45
3.1.4	X-ray Diffraction of Pb-based oxynitride perovskites	48
3.2	Morphological and Elemental Characterization	52
3.2.1	FESEM-EDS of Ba-Based Oxynitride Perovskites	52
3.2.2	FESEM-EDS of Ca-Based Oxynitride Perovskites	55
3.2.3	FESEM-EDS of Mg-Based Oxynitride Perovskites	58
3.2.4	FESEM-EDS of Pb-Based Oxynitride Perovskites	60
3.3	Atomic Force Microscope Analysis (AFM)	63
3.3.1	Ba-Based Oxynitride Perovskites	63
3.3.2	Ca-Based Oxynitride Perovskites	66
3.3.3	Mg-Based Oxynitride Perovskites	69
3.3.4	Pb-Based Oxynitride Perovskites	72
3.4	FTIR Spectroscopy Analysis	76
3.4.1	Ba-Based Oxynitride Perovskites	76
3.4.2	Ca-Based Oxynitride Perovskites	79
3.4.3	Mg-Based Oxynitride Perovskites	82

3.4.4	Pb-Based Oxynitride Perovskites	85
3.5	Optical Properties	88
3.5.1	UV-Vis Spectroscopy	88
3.5.1.1	Ba-Based Oxynitride Perovskites	88
3.5.1.2	Ca-Based Oxynitride Perovskites	90
3.5.1.3	Mg-Based Oxynitride Perovskites	93
3.5.1.4	Pb-Based Oxynitride Perovskites	95
3.6	Thermogravimetric Analysis (TGA)	98
3.6.1	Ba-Based Oxynitride Perovskites	98
3.6.2	Ca-Based Oxynitride Perovskites	102
3.6.3	Mg-Based Oxynitride Perovskites	105
3.6.4	Pb-Based Oxynitride Perovskites	110
3.7	Hall Effect	114
3.7.1	Ba-Based Oxynitride Perovskites	114
3.7.2	Ca-Based Oxynitride Perovskites	115
3.7.3	Mg-Based Oxynitride Perovskites	117
3.7.4	Pb-Based Oxynitride Perovskites	119
3.8	Solar Cell Applications	120
3.8.1	Ba-Based Oxynitride Perovskites	120
3.8.2	Ca-Based Oxynitride Perovskites	123
3.8.3	Mg-Based Oxynitride Perovskites	126
3.8.4	Pb-Based Oxynitride Perovskites	129
3.9	Conclusions	133
3.10	Recommendations	134
3.11	References	135

List of Figures

Figure No.	Subject	Page No.
	Chapter one: Introduction	
1.1	Best Research-Cell Efficiency Chart	2
1-2	Silicon and Perovskite Solar Cells	5
1-3	Classifications of Nanomaterials	9
1-4	Synthesis Methods of Nanomaterials	12
1-5	Intrinsic Semiconductors	13
1-6	N-type and P-type Semiconductor	14
	Chapter Two: Experimental Methodology	
2-1	Schematic Flow Diagram of the General Sol-gel Method	33
2-2	Solar Cell Testing System Process	35
	Chapter Three: Result and Discussion	
3-1	X-ray Diffraction Patterns of the Synthesized Ba-Based Oxynitride Perovskite via Sol–gel Technique	38
3-2	X-ray Crystal Structures of Synthesized Ba-Based Oxynitride Perovskite via Sol–gel Auto-Combustion Technique.	40
3-3	X-ray Diffraction Patterns of the Synthesized Ca-Based Oxynitride Perovskite via Sol–gel Technique	42
3-4	X-ray Crystal Structures of Synthesized Ca-Based Oxynitride Perovskite via Sol–gel Auto-Combustion Technique	44
3-5	X-ray Diffraction Patterns of the Synthesized Mg-Based Oxynitride Perovskites via Sol–gel Auto-Combustion Technique	46
3-6	X-ray Crystal Structures of Synthesized Mg-Based Oxynitride Perovskite via sol–gel Auto-Combustion Technique.	48
3-7	X-ray Diffraction Patterns of the Synthesized Pb-Based Oxynitride Perovskite via Sol–gel Auto-Combustion Technique.	50
3-8	X-ray Crystal Structures of Synthesized Pb-Based Oxynitride Perovskite via Sol–gel Auto-Combustion Technique.	52
3-9	FESEM Micrographs of $BaCuO_2N$, $BaCoO_2N$, and $BaCu_{0.5}Co_{0.5}O_2N$ Oxynitride Perovskites Synthesized by the Sol–gel Auto-Combustion Technique.	54
3-10	FESEM Micrographs of $CaCuO_2N$, $CaCoO_2N$, and $CaCu_{0.5}Co_{0.5}O_2N$ Oxynitride Perovskite Synthesized by the Sol–gel Auto-Combustion Technique.	57

3-11	FESEM Micrographs of $MgCuO_2N$, $MgCoO_2N$, and $MgCu_{0.5}Co_{0.5}O_2N$ Oxynitride Perovskites Synthesized by the Sol–gel Auto-Combustion Technique.	59
3-12	FESEM Micrographs of $PbCuO_2N$, $PbCoO_2N$, and $PbCu_{0.5}Co_{0.5}O_2N$ Oxynitride Perovskite Synthesized by Sol–gel Auto-Combustion Technique	62
3-13	AFM Images of $BaCuO_2N$, $BaCoO_2N$ and $BaCu_{0.5}Co_{0.5}O_2N$ Oxynitride Perovskites Synthesized by the Sol–gel Auto-Combustion Technique	64
3-14	AFM Images of $CaCuO_2N$, $CaCoO_2N$ and $CaCu_{0.5}Co_{0.5}O_2N$ Oxynitride Perovskites Synthesized by the Sol–gel Auto-Combustion Technique.	67
3-15	AFM Images of $MgCuO_2N$, $MgCoO_2N$ and $MgCu_{0.5}Co_{0.5}O_2N$ Oxynitride Perovskites Synthesized by the Sol–gel Auto-Combustion Technique.	70
3-16	AFM Images of $PbCuO_2N$, $PbCoO_2N$ and $PbCu_{0.5}Co_{0.5}O_2N$ Oxynitride Perovskites Synthesized by the Sol–gel Auto-Combustion Technique.	73
3-17	FTIR Spectra of $BaCuO_2N$, $BaCoO_2N$ and $BaCu_{0.5}Co_{0.5}O_2N$ Oxynitride Perovskites Synthesized by the Sol–gel Auto-Combustion Technique.	78
3-18	FTIR Images of $CaCuO_2N$, $CaCoO_2N$ and $CaCu_{0.5}Co_{0.5}O_2N$ Oxynitride Perovskites Synthesized by the Sol–gel Auto-Combustion Technique.	81
3-19	FTIR Images of $MgCuO_2N$, $MgCoO_2N$ and $MgCu_{0.5}Co_{0.5}O_2N$ Oxynitride Perovskites Synthesized by the Sol–gel Auto-Combustion Technique.	84
3-20	FTIR Images of $PbCuO_2N$, $PbCoO_2N$ and $PbCu_{0.5}Co_{0.5}O_2N$ Oxynitride Perovskites Synthesized by the Sol–gel Auto-Combustion Technique.	87
3-21	UV–Vis spectra and Tauc plots of $BaCuO_2N$, $BaCoO_2N$ and $BaCu_{0.5}Co_{0.5}O_2N$ Oxynitride Perovskites Synthesized by the Sol–gel Auto-Combustion Technique.	89
3-22	UV–Vis spectra and Tauc plots of $CaCuO_2N$, $CaCoO_2N$ and $CaCu_{0.5}Co_{0.5}O_2N$ Oxynitride Perovskites Synthesized by the Sol–gel Auto-Combustion Technique.	92
3-23	UV–Vis spectra and Tauc plots of $MgCuO_2N$, $MgCoO_2N$ and $MgCu_{0.5}Co_{0.5}O_2N$ Oxynitride Perovskites Synthesized by the Sol–gel Auto-Combustion Technique.	94
3-24	UV–Vis spectra and Tauc plots of $PbCuO_2N$, $PbCoO_2N$ and $PbCu_{0.5}Co_{0.5}O_2N$ Oxynitride Perovskites Synthesized by the Sol–gel Auto-Combustion Technique.	97

3-25	TGA Thermograms of $BaCuO_2N$, $BaCoO_2N$ and $BaCu_{0.5}Co_{0.5}O_2N$ Oxynitride Perovskites Synthesized by the Sol–gel Auto-Combustion Technique.	100
3-26	TGA Thermograms of $CaCuO_2N$, $CaCoO_2N$ and $CaCu_{0.5}Co_{0.5}O_2N$ Oxynitride Perovskites Synthesized by the Sol–gel Auto-Combustion Technique.	104
3-27	TGA Thermograms of $MgCuO_2N$, $MgCoO_2N$ and $MgCu_{0.5}Co_{0.5}O_2N$ Oxynitride Perovskites Synthesized by the Sol–gel Auto-Combustion Technique.	108
3-28	TGA Thermograms of $PbCuO_2N$, $PbCoO_2N$ and $PbCu_{0.5}Co_{0.5}O_2N$ Oxynitride Perovskites Synthesized by the Sol–gel Auto-Combustion Technique	112
3-29	J-V Curves of $BaCuO_2N$, $BaCoO_2N$ and $BaCu_{0.5}Co_{0.5}O_2N$ Oxynitride Perovskites Synthesized by the Sol–gel Auto-Combustion Technique.	122
3-30	J-V Curves of $CaCuO_2N$, $CaCoO_2N$ and $CaCu_{0.5}Co_{0.5}O_2N$ Oxynitride Perovskites Synthesized by the Sol–gel Auto-Combustion Technique.	125
3-31	J-V Curves of $MgCuO_2N$, $MgCoO_2N$ and $MgCu_{0.5}Co_{0.5}O_2N$ Oxynitride Perovskites Synthesized by the Sol–gel Auto-Combustion Technique.	128
3-32	J-V Curves of $PbCuO_2N$, $PbCoO_2N$ and $PbCu_{0.5}Co_{0.5}O_2N$ Oxynitride Perovskites Synthesized by the Sol–gel Auto-Combustion Technique.	131

List of Tables

Table NO.	Subject	Page NO.
2-1	Chemicals	26
2-2	Instruments	27
3-1	X--ray data of $BaCuO_2N$, $BaCoO_2N$, and $BaCu_{0.5}Co_{0.5}O_2N$ Oxynitride Perovskites Synthesized by the Sol–gel Auto-Combustion Technique	40
3-2	X--ray Data of $CaCuO_2N$, $CaCoO_2N$, and $CaCu_{0.5}Co_{0.5}O_2N$ Oxynitride Perovskites Synthesized by the Sol–gel Auto-Combustion Technique	44
3-3	X-ray Data of $MgCuO_2N$, $MgCoO_2N$, and $MgCu_{0.5}Co_{0.5}O_2N$ Oxynitride Perovskites Synthesized by the Sol–gel Auto-Combustion Technique	47

3-4	X-ray Data of $PbCuO_2N$, $PbCoO_2N$, and $PbCu_{0.5}Co_{0.5}O_2N$ Oxynitride Perovskites Synthesized by the Sol–gel Technique	51
3-5	AFM Data of $BaCuO_2N$, $BaCoO_2N$ and $BaCu_{0.5}Co_{0.5}O_2N$ Oxynitride Perovskites Synthesized by the Sol–gel Auto-Combustion Technique	65
3-6	AFM Data of $CaCuO_2N$, $CaCoO_2N$ and $CaCu_{0.5}Co_{0.5}O_2N$ Oxynitride Perovskites Synthesized by the Sol–gel Auto-Combustion Technique	68
3-7	AFM Data of $MgCuO_2N$, $MgCoO_2N$ and $MgCu_{0.5}Co_{0.5}O_2N$ oxynitride perovskites synthesized by the sol–gel Auto-Combustion technique.	71
3-8	AFM Data of $PbCuO_2N$, $PbCoO_2N$ and $PbCu_{0.5}Co_{0.5}O_2N$ Oxynitride Perovskites Synthesized by the Sol–gel Auto-Combustion Technique	75
3-9	Thermodynamic Data of $BaCuO_2N$, $BaCoO_2N$ and $BaCu_{0.5}Co_{0.5}O_2N$ Oxynitride Perovskites Synthesized by the Sol–gel Auto-Combustion Technique	101
3-10	Thermodynamic Data of $CaCuO_2N$, $CaCoO_2N$ and $CaCu_{0.5}Co_{0.5}O_2N$ Oxynitride Perovskites Synthesized by the Sol–gel Auto-Combustion Technique	105
3-11	Thermodynamic Data of $MgCuO_2N$, $MgCoO_2N$ and $MgCu_{0.5}Co_{0.5}O_2N$ Oxynitride Perovskites Synthesized by the Sol–gel Auto-Combustion Technique.	109
3-12	Thermodynamic data of $PbCuO_2N$, $PbCoO_2N$ and $PbCu_{0.5}Co_{0.5}O_2N$ Oxynitride Perovskites Synthesized by the Sol–gel Auto-Combustion Technique.	113
3-13	Hall Effect data of $BaCuO_2N$, $BaCoO_2N$ and $BaCu_{0.5}Co_{0.5}O_2N$ Oxynitride Perovskites Synthesized by the Sol–gel Auto-Combustion Technique.	115
3-14	Hall Effect data of $CaCuO_2N$, $CaCoO_2N$ and $CaCu_{0.5}Co_{0.5}O_2N$ Oxynitride Perovskites Synthesized by the Sol–gel Auto-Combustion Technique	116
3-15	Hall Effect data of $MgCuO_2N$, $MgCoO_2N$ and $MgCu_{0.5}Co_{0.5}O_2N$ Oxynitride Perovskites Synthesized by the Sol–gel Auto-Combustion Technique	118
3-16	Hall Effect data of $PbCuO_2N$, $PbCoO_2N$ and $PbCu_{0.5}Co_{0.5}O_2N$ Oxynitride Perovskites Synthesized by the Sol–gel Auto-Combustion Technique.	120
3-17	Parameters of $BaCuO_2N$, $BaCoO_2N$ and $BaCu_{0.5}Co_{0.5}O_2N$ Solar Cells	123
3-18	Parameters of $CaCuO_2N$, $CaCoO_2N$ and $CaCu_{0.5}Co_{0.5}O_2N$ Solar Cells	126

3-19	Parameters of $MgCuO_2N$, $MgCoO_2N$ and $MgCu_{0.5}Co_{0.5}O_2N$ Solar Cells.	129
3-20	Parameters of $PbCuO_2N$, $PbCoO_2N$ and $PbCu_{0.5}Co_{0.5}O_2N$ Solar Cells.	132

List of characters abbreviations

Symbol	Meaning
°C	Degree Celsius
A	Absorbance
AFM	Atomic Force Microscopy
cm^3	Cubic Centimetre
D	Crystallite Size
D*	Specific Detectivity
DC	Direct Current
DMSO	Dimethyl Sulfoxide
EDX / EDS	Energy-Dispersive X-ray Spectroscopy
Eg	Optical Energy Band Gap
EQE (%)	External Quantum Efficiency
Ev	Electron Volt
FESEM	Field Emission Scanning Electron Microscopy
FF	Fill Factor
FTIR	Fourier-Transform Infrared Spectroscopy
FWHM	Full Width at Half Maximum
g	Gram
I_{ph}	The Net Photocurrent
J_{dark}	The Dark Current Density
Jmax	Current Density at Maximum Power
Jsc	Short-Circuit Current Density
K	Kelvin
mA	Milliampere
nm	Nanometer
P	Power Density
PCE	Power Conversion Efficiency
PSC	Perovskite Solar Cell
PV	Photovoltaic
R	Reflectance / Reflectivity
RH	Hall Coefficient
Rs	Sheet Resistance
T	Transmittance

TGA	Thermogravimetric Analysis
UV-Vis	Ultraviolet–Visible Spectroscopy
V_{av}	Average Voltage
V_H	Hall Voltage / Potential Difference
Vmax	Voltage at Maximum Power
V_{oc}	Open-Circuit Voltage
XRD	X-ray Diffraction
α	Absorption Coefficient
β	Structural line broadening (FWHM) / Diffraction angle
θ	Diffraction Angle
λ	X-ray Wavelength

Chapter One

Introduction

1. Introduction

The global energy sector currently faces significant challenges associated with increasing energy demand, environmental degradation, and the finite nature of fossil fuel resources. To address these challenges, solar photovoltaic (PV) technology has become an important renewable-energy technology for electricity generation, through the photovoltaic effect, which enables semiconductor materials to convert incident solar radiation directly into electrical energy [1,2]. Within this field, Perovskite Solar Cells (PSCs) have emerged as a promising class of photovoltaic devices, owing to their rapidly increasing power conversion efficiencies and the potential for low-cost fabrication.

As shown in Fig. (1-1), the power conversion efficiency of perovskite solar cells has increased substantially since their initial development. The reported PCE of single-junction perovskite solar cells increased from approximately 3.8% in 2009 to 26.95% at the laboratory scale [3]. Moreover, silicon/perovskite tandem cells have also achieved PCE values exceeding 34.85% [4]. Perovskite/CIGS tandem solar cells have also demonstrated PCE values of approximately 26.3% [3].

However, the practical use of perovskite solar cells has been hindered by stability problems. Therefore, increasing attention has been given to the development of alternative inorganic and nanostructured perovskite materials as a possible approach to improve material stability. Among these materials, transition-metal oxynitride perovskites have attracted interest because they contain oxygen and nitrogen in their crystal structure and may have tunable structural and electronic properties. These materials may provide new opportunities for their use in photovoltaic applications [5,3].

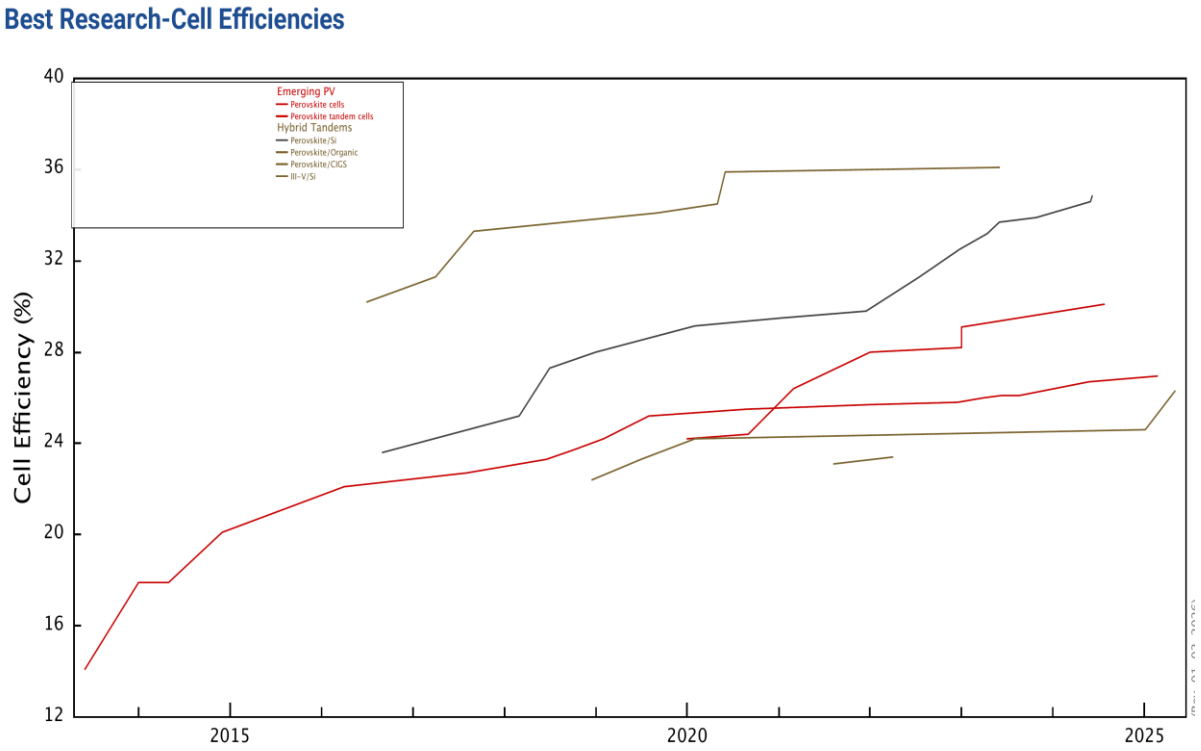


Fig. (1-1): Best research-cell efficiency chart for emerging solar technologies (2013–2025)[3].

1.1 Solar Cells

Photovoltaic solar cells directly convert sunlight into electrical energy through the photovoltaic effect in semiconductor materials[6]. The photovoltaic effect was first observed by Edmond Becquerel in 1839, when he discovered that light could generate an electric current in an electrochemical system[7]. The first solid-state solar cell was developed in 1883 by Charles Fritts using selenium, but it exhibited very low efficiency of less than 1%[6,8]. Silicon-based solar cells became the dominant photovoltaic technology due to their high stability and improved efficiency[9]. Solar cells operate by absorbing photons, which generate electron–hole pairs that are separated by an internal electric field to produce direct current (DC)[9]. Solar cells are commonly classified into three generations: crystalline silicon technologies (first generation), thin-film technologies (second generation), and emerging technologies such as

perovskite, organic, and dye-sensitized solar cells (third generation)[10]. Perovskite solar cells have shown a rapid increase in efficiency, rising from about 3.8% in 2009 to over 26% in laboratory-scale devices[11].

1.1.1 Solar Cell Generations

Solar cells are generally classified into three major generations according to the type of materials used, fabrication techniques, efficiency, and technological development[10,12]. Continuous advancements in photovoltaic technologies have significantly improved power conversion efficiency, reduced manufacturing costs, and enhanced the operational stability of solar cells, making them among the most promising renewable energy technologies[13,10].

a. First-Generation Solar Cells

First-generation solar cells are mainly based on crystalline silicon technology and include monocrystalline silicon and polycrystalline silicon solar cells[14]. These cells are considered the most commercially mature photovoltaic technology due to their high efficiency, long-term operational stability, and well-established manufacturing infrastructure. However, their fabrication requires highly purified silicon and energy-intensive processing techniques, resulting in relatively high production costs [14,15].

b. Second-Generation Solar Cells

Second-generation solar cells were developed to reduce manufacturing costs and material consumption through thin-film technologies. This generation includes cadmium telluride (CdTe),

copper indium gallium selenide (CIGS), and amorphous silicon (a-Si) solar cells[16]. Thin-film solar cells are characterized by lower material consumption, lightweight structures, and flexible fabrication processes; however, their power conversion efficiencies are generally lower than those of crystalline silicon solar cells[17].

c. Third-Generation Solar Cells

Third-generation solar cells represent emerging photovoltaic technologies designed to overcome the efficiency limitations of conventional solar cells while simultaneously reducing fabrication costs. This generation includes organic solar cells, dye-sensitized solar cells (DSSCs), quantum dot solar cells, and perovskite solar cells (PSCs). These technologies provide several advantages, including tunable optical properties, solution-processable fabrication methods, and compatibility with flexible substrates[16,18,19].

1.1.2 Perovskite Solar Cells (PSCs)

Perovskite materials exhibit a high absorption coefficient, extended carrier diffusion length, and adjustable band gap, facilitating effective light harvesting in thin layers[20]. A common perovskite solar cell (PSC) comprises an electron transport layer (ETL), a perovskite absorber, a hole transport layer (HTL), and electrodes to facilitate efficient charge separation and transmission[21]. Despite their benefits, PSCs face stability challenges when exposed to moisture, heat, and ultraviolet radiation, as well as concerns regarding lead toxicity[22]. Recent studies concentrate on enhancing stability and performance through the utilization of nanomaterials and metal oxide frameworks. Nanomaterials can influence

charge transfer, recombination, and structural properties, potentially affecting PSC performance[23].

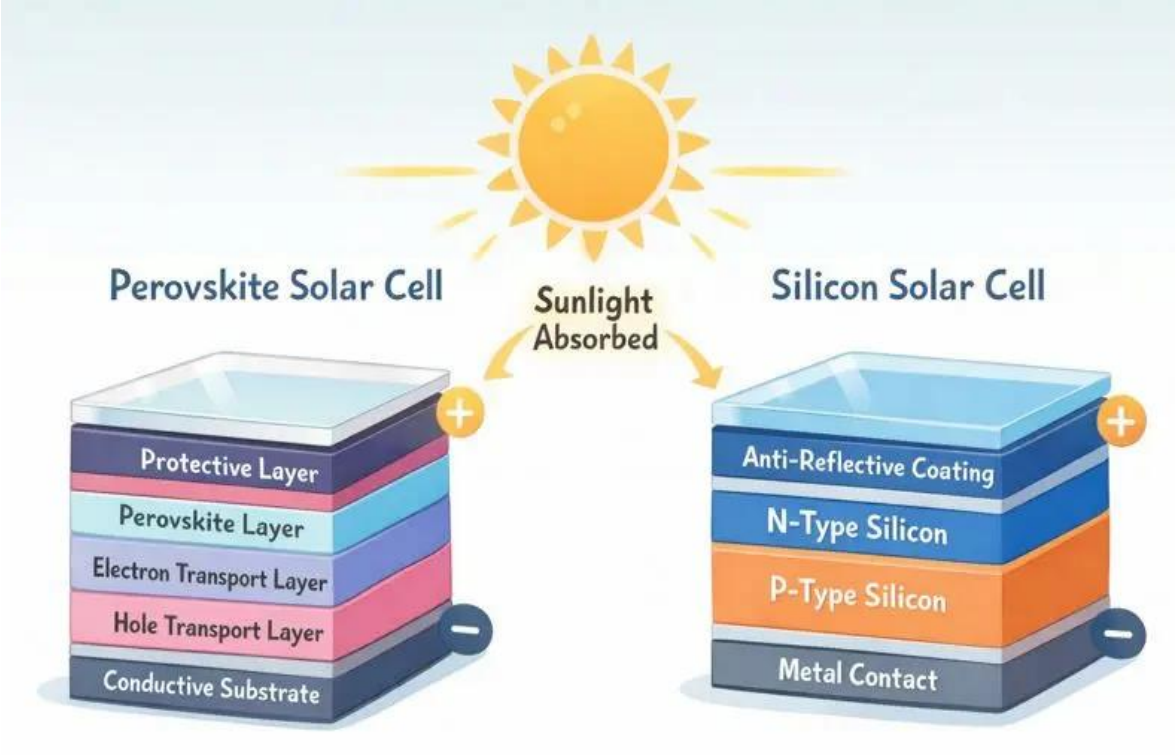


Fig. (1-2): A comparison between silicon and perovskite solar cells[24].

1.2 Nanomaterials

The term "nano" refers to a scale of one billionth of a meter (10^{-9} m), and nanotechnology refers to the interdisciplinary science focused on the development, characterization, and synthesis of materials by controlling their dimensions and forms at the nanoscale[25]. This class of material is characterized by at least one dimension ranging from 1-100 nm[26]. Its essential importance lies in the emergence of unique physical and chemical properties of materials when their dimensions are reduced to the nanoscale.

This is primarily due to two physical phenomena: the increase in the surface-to-volume ratio and quantum confinement effects[27]**.** This importance is evident in the field of renewable energy and perovskite cells through improved light absorption, which increases energy conversion efficiency. Furthermore, the ability to precisely adjust the band gap by controlling the size and shape of nanoparticles and reducing the distance travelled by charge carriers (electrons and holes), which can facilitate charge transport and improve charge collection, thereby potentially reducing recombination losses and increasing the generated current[28].

1.2.1 Nanomaterials Classifications

Nanomaterials can be categorized by various criteria, such as composition, structure, synthesis method, and applications[29]**.** They are also classified into four main categories (0D, 1D, 2D, 3D) based on the number of dimensions that fall outside the nanoscale (i.e., dimensions that are greater than 100 nanometres) as shown in Fig. (1-3):

1.2.1.1 Dimensional-Based Nanomaterials

- **Zero-Dimensional (0D) Nanomaterials:** Are a category of nanomaterials that are confined in all three spatial dimensions at the nanoscale. Include: Quantum Dots (GQDs)[30], carbon quantum dots (CQDs)[31], fullerene (C60)[32], inorganic quantum dots (QDs)[33], magnetic nanoparticles (MNPs)[34], noble metal nanoparticles[35], upconversion nanoparticles (UCNPs)[36], polymer dots (Pdots), etc.[37]. Despite the variety of zero-dimensional materials, perovskite quantum dots (PQDs) are important materials for solar energy applications due to their favourable optical properties[38].

- **One-Dimensional (1D) Nanomaterials:** 1D nanomaterials restricted to two dimensions and maintain one degree of freedom for the carriers. The dimensions of one-dimensional magnetic nanomaterials are confined to less than 100 nm along two of the three axes[39,40]. Nanowires and nanorods are the most prevalent types of 1D magnetic nanomaterials. These are long, thin structures that can reach lengths of several μm and diameters of a few nm to several hundred nm. Nanotubes can vary in length and have nanometre-scale dimensions. Compared to nanowires, nanorods are longer structures with a greater length-to-diameter ratio[41].

- **Two-Dimensional (2D) Nanomaterials:** are characterized by quantum confinement in one dimension and two degrees of freedom for charge carriers. The thickness of 2D nanomaterials is limited to the nanoscale (typically below 100 nanometres) along one axis, while charge carriers are free to move along the other two axes. 2D nanomaterials include Nanosheets and Graphene[39,40,42].

- **Three-Dimensional (3D) Nanomaterials:** 3D nanomaterials are structures in which the nanoscale features extend in all three dimensions, while the overall structure may have dimensions larger than 100 nm. They can be formed through the assembly or intimate contact of 0D, 1D, and 2D structural elements. 3D nanomaterials include nanostructured bulk materials, nanocomposites, and porous materials with nanoscale structural features [43]. As shown in Fig. (1-3).

1.2.1.2 Material-Based Nanomaterials

Nanomaterials are mainly categorized by their composition into four principal types: carbon-based materials, metal-based materials, dendrimers (branched polymers), and composites.

- **Carbon-based Nanomaterials:** consist primarily of carbon and often manifest as hollow spheres (fullerenes), ellipsoids, or tubes (nanotubes)[44].
- **Metal-based Nanomaterials**: metal particles with size ranging (1-100 nm) such as nanogold and nanosilver, exhibit unique optoelectronic properties[45].
- **Polymer-based Nanomaterials:** such as dendrimers that are often used in drug delivery, these nanoscale polymers are constructed from branching units[46].
- **Composites Nanomaterials:** a combination of nanoparticle with other nanoparticles or with bulk materials to enhance properties[47].

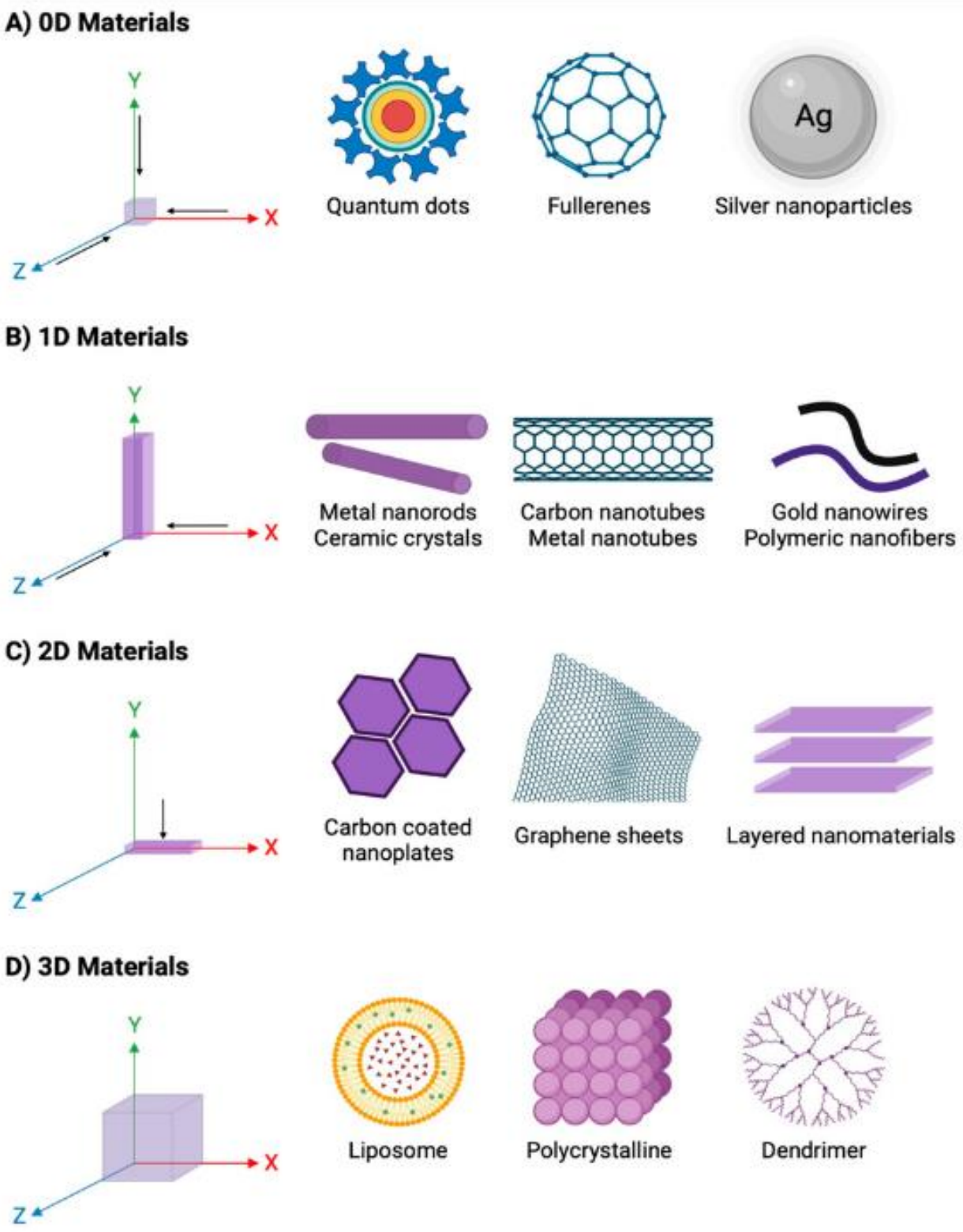


Fig. (1-3): Classifications of Nanomaterials Based on the Dimensions[48].

1.3 Synthesis Methods of Nanomaterials

1.3.1 Sol-gel auto-combustion method: The sol–gel auto-combustion method is a solution-based synthesis technique in which dissolved precursor materials undergo complexation and gel formation, followed by auto-combustion to produce a fine and homogeneous precursor powder. The obtained powder can then be subjected to calcination to remove residual organic components and promote the formation of the desired crystalline phase [49].

1.3.2 Chemical Vapor Deposition (CVD): This method creates a thin film or nanomaterial by breaking down precursor gases on a substrate. It is frequently used to generate semiconductor nanowires, graphene, and carbon nanotubes[50].

1.3.3 Chemical Precipitation: This method involves the precipitation of solution ions by adding a precipitating agent while controlling several factors such as temperature, pH and concentration. This method is used in the manufacture of metal oxide nanoparticles and metal nanoparticles[51].

1.3.4 Hydrothermal: This method is carried out in an autoclave (steel pressure vessel) at high temperature and using an aqueous solution in a sealed reaction vessel, followed by the precipitation of small particles. This method is based on the reaction of the solution, where water is used as the solvent. It is used to prepare solids such as microporous crystals, thin films and nanoparticles[52,53]**.**

1.3.5 Pyrolysis: Pyrolysis is a thermal decomposition method used for the synthesis of nanomaterials, in which a precursor (liquid or solid) is thermally decomposed at high temperature to produce nanomaterials[54].

1.3.6 Sputtering: This method involves deposition of nanomaterials on the surface of substrate by particle ejection using high energy ions[55].

1.3.7 Green Synthesis: It is a method for preparing materials, especially nanoparticles, using natural or environmentally friendly materials such as plants, enzymes, or biological extracts, with the aim of reducing or eliminating the use of toxic and polluting chemicals. It relies on green chemistry principles to achieve a safe, environmentally friendly, and industrially applicable process[56].

1.3.8 Mechanical Milling: Often referred to as ball milling, this process reduces particle size to the nanoscale by mechanically grinding bulk materials while milling media is present. It is frequently employed to create alloy and metallic nanoparticles[57].

1.3.9 Laser Ablation: In laser ablation, a target material in a liquid or gas environment is exposed to a high-energy laser beam, which causes vaporization and subsequent condensation to produce nanoparticles. This process is frequently employed to create carbon-based materials and metal nanoparticles[58].

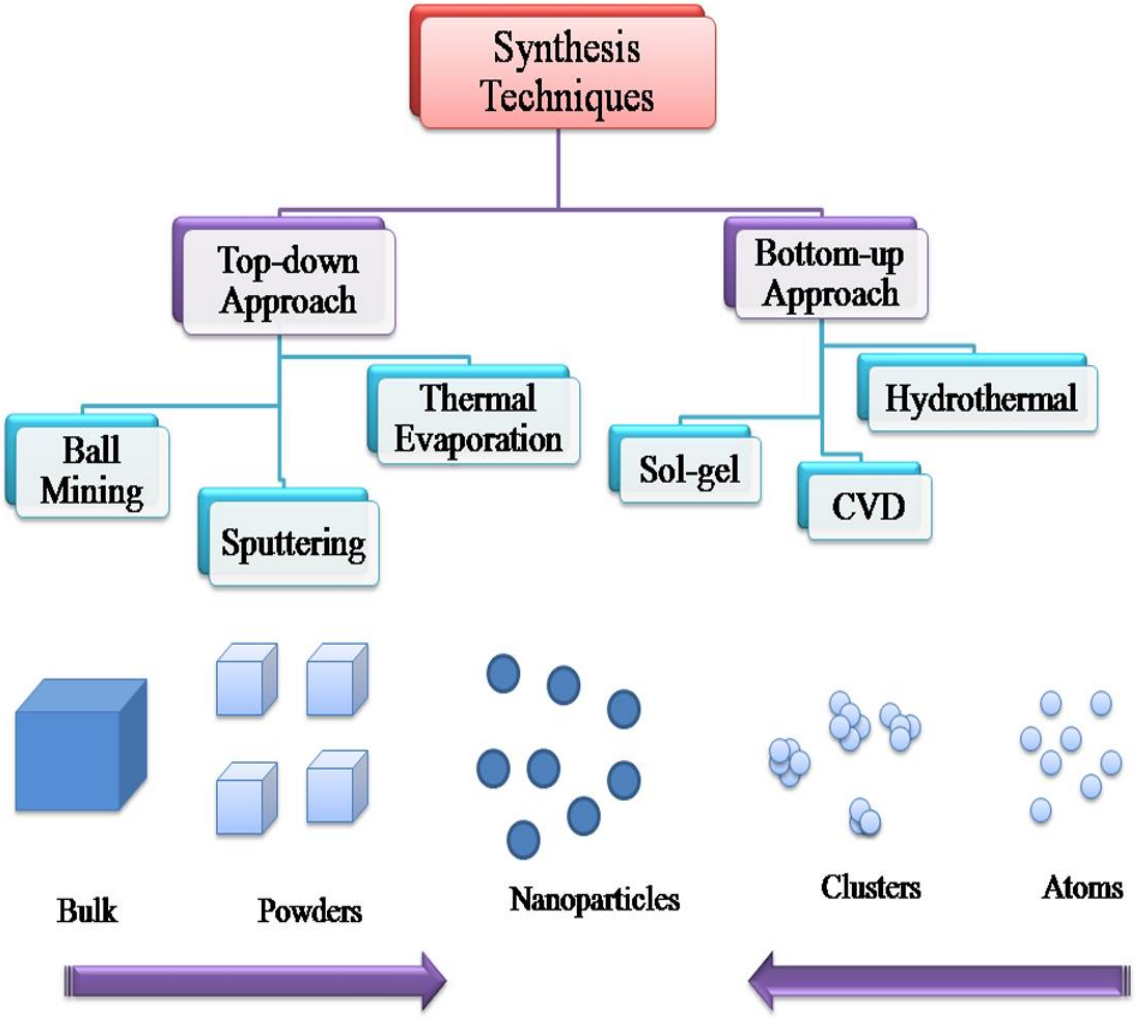


Fig. (1-4): Synthesis methods of nanomaterials[59].

1.4 Semiconductors: Are materials that occupy an intermediate position between conductors and insulators. semiconductors electrical conductivity can be controlled through doping or changing the temperature. The electrical conductivity of semiconductors depends on the concentration and mobility of charge carriers and the electronic band structure of the material[60]. Silicon is the most widely used semiconductor, and is widely used in computers, automobiles, and networks[60].

Semiconductors are divided into two main categories based on their purity:

1.4.1 Intrinsic Semiconductors: Intrinsic semiconductors are semiconductors composed of a pure material[61]. Intrinsic semiconductors have electrical properties that result solely from their crystalline structure, without the influence of external impurities. Silicon (Si) and germanium (Ge) are among the most common intrinsic semiconductors[62]. In this type of semiconductor, the valence band is filled with electrons while the conduction band is empty at low temperatures. As the temperature rises, some electrons gain enough energy to move into the conduction band. This results in the formation of electron-hole pairs, which contribute to electrical conductivity[62,63]. As shown in fig. (1-5).

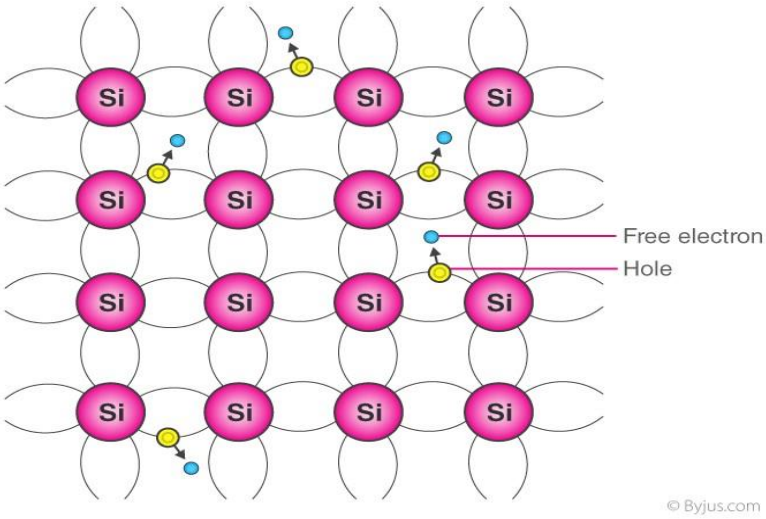


Figure (1-5): Intrinsic Semiconductors.

1.4.2 Extrinsic Semiconductors: These are semiconductors whose conductivity has been altered by doping. They are separated into two categories[61]:

- **N-type:** A pure semiconductor doped with pentavalent atoms (such as P or As), which increases the number of free electrons that are the primary charge carriers.

- **P-type**: A pure semiconductor doped with trivalent atoms (such as B or Al). This creates holes that act as the primary positive charge carriers.

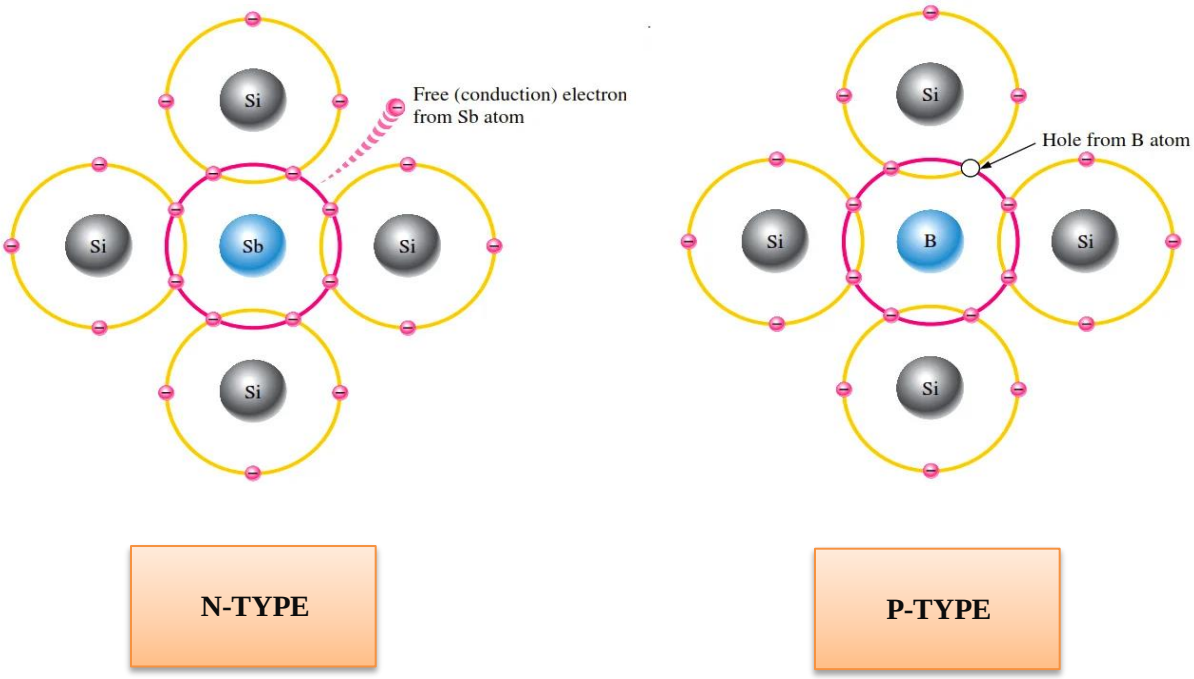


Fig. (1-6): N-type and P-type Semiconductor.

1.5 Crystalline Semiconductors: Materials that have a regular and repeating atomic arrangement within a crystal lattice, and this arrangement is the primary reason for their distinctive electrical properties**.**

1.5.1 Single Crystal Semiconductors: Are defined as semiconductor materials consisting of a single, homogeneous crystal. All atoms are

arranged in a fixed periodic pattern within the crystal lattice, such as silicon[64].

1.5.2 Polycrystalline Semiconductors: defined as materials composed of a large number of small crystals (granules), where each crystal within the material has a regular atomic arrangement, although the direction of this arrangement varies from grain to grain[65].

1.6 Copper-Based Perovskites: Copper-based perovskites have attracted attention because of their distinctive electronic and optical properties, which are related to the electronic configuration and variable oxidation states of copper. Cu-containing perovskite and perovskite-like materials have been investigated for applications in optoelectronics, photovoltaics, and other energy-related technologies. In particular, copper-based materials have been explored as alternatives to lead-containing materials because of the abundance of copper and their tunable electronic properties[66].

1.7 Cobalt-Based Perovskites: Are characterized by diverse electronic, magnetic, and electrical properties arising from the variable oxidation states and spin states of cobalt. The coexistence of different cobalt valence states, such as Co^{2+}, Co^{3+}, and Co^{4+}, together with different spin configurations, can strongly influence the structural, magnetic, and charge-transport properties of cobalt-containing perovskites. Consequently, cobalt perovskites have been extensively investigated for their magnetic, electrical, thermoelectric, and energy-related properties[67]**.**

1.8 Characterization Techniques of Semiconductors

1.8.1 Principles of X-ray Diffraction (XRD)

X-rays are electromagnetic waves located between ultraviolet and gamma rays, with wavelengths ranging from 0.01 to 10 nm. They are widely used in X-ray diffraction (XRD) because their wavelengths are comparable to interatomic distances in crystal lattices, making them suitable for studying crystal structure, phase identification, and interplanar spacing[68].

Diffraction in crystals depends mainly on the crystal structure and the wavelength of the incident beam. Constructive interference occurs when the path difference between the incident and reflected X-rays is an integer multiple of the wavelength, which is described by Bragg's Law[69]:

$$n\lambda = 2d \sin\theta \quad \ldots\ldots\ldots (1)$$

Where:

- n: is the diffraction order.
- λ: is the X-ray wavelength.
- d: is the interplanar spacing.
- θ: is the diffraction angle.

Another important parameter obtained from XRD data is the crystallite size, which is estimated using Scherrer's equation[70]:

$$D = \frac{K\lambda}{\beta \cos\theta} \quad \ldots\ldots\ldots (2)$$

Where:

- D: is the crystallite size.
- K: is the shape factor (~0.9).

- β: is the full width at half maximum (FWHM).
- θ: is the diffraction angle.

This equation is used to estimate the average crystallite size from peak broadening in XRD patterns[70].

1.9 Morphological Properties

1.9.1 Field Emission Scanning Electron Microscopy (FESEM)

Is a high-resolution technique used to examine the surface morphology and topography of materials at the nanoscale, offering high magnification and a large depth of field suitable for advanced material characterization. Compared to conventional SEM, FESEM provides higher spatial resolution and better image quality due to its field emission electron source, which produces a highly focused beam with reduced noise. The accelerating voltage typically ranges from 0.5 to 30 kV, allowing low-voltage operation that reduces charging effects and sample damage. The technique works by scanning the sample surface with a focused electron beam, while emitted signals are collected to generate detailed images of surface features[71].

1.9.2 Energy-Dispersive X-ray Spectroscopy (EDS)

Energy-dispersive X-ray spectroscopy (EDS), one of the commonly used analytical techniques for the analysis of the elemental composition of solid matter, has recently become very important in terms of its application to the chemical analysis of nanoparticles, particularly when used in conjunction with a scanning electron microscope (SEM) and the transmission operation mode of SEM (STEM-in-SEM). The advancement of highly sensitive EDS detectors, which allow for the rapid EDS inspection of individual nanoparticles at a SEM, was the primary driver of

this breakthrough. In addition to the high-resolution information on the sample within the same scanned area that the electron microscope provides, qualitative information on elemental composition with a spatial resolution of roughly 10 nm can be obtained. in addition to the SEM's high-resolution pictures. Therefore, even though there are certain restrictions that could compromise the accuracy of the data, EDS is an essential instrument for characterizing nanomaterials and researching their structural characteristics[72].

1.9.3 Atomic Force Microscopy (AFM)

A high-resolution method for examining the topography and surface morphology of materials at the nanoscale is atomic force microscopy, or AFM. The method involves using a sharp tip attached to a sensitive cantilever to scan the sample surface. The cantilever deflects as a result of the interaction forces between the tip and the surface. A laser beam and a photodetector device are used to detect this deflection and produce high-resolution surface images. Because AFM is not constrained by visible light diffraction, it can achieve significantly better spatial resolution than optical microscopy. AFM can be utilized in several operating modes to examine the mechanical, electrical, and surface characteristics of materials in addition to surface imaging[73].

1.10 Hall Effect

The Hall effect is a basic scientific phenomenon that explains how an electric current flowing through an electrical conductor under the influence of a magnetic field perpendicular to the current direction creates a voltage differential across the conductor, known as the Hall voltage. This effect is caused by the Lorentz force deflecting charge carriers like electrons or

holes. Important electrical characteristics of materials, such as carrier concentration, carrier type, mobility, and conductivity, are frequently determined by Hall effect studies[74].

1.11 Literature Survey

In 2017, Hosono et al. reported flux-assisted liquid-phase sintering of $SrTaO_2N$ using $BaCN_2$ at ~900 °C, which prevented thermal decomposition and eliminated the need for post-ammonolysis. The obtained material showed relative dielectric constants of 68–90 with low loss (<0.11). The study also observed the formation of $Sr_{1-x}Ba_xTaO_2N$ solid-solution crystals, indicating enhanced grain growth and compositional variation due to flux-assisted crystal growth[77].

In 2018, Kobayashi et al. reviewed the recent developments in mixed-anion perovskite-type oxides, emphasizing the structural and functional diversity introduced by incorporating a second anionic species, such as nitride, fluoride, or hydride. The authors highlighted those variations in anionic charge, ionic radius, covalency, and local coordination geometry offer effective pathways to manipulate charge-carrier density, electronic transport, and chemical reactivity. Their findings provide a solid theoretical framework for utilizing anion-substitution strategies, particularly in oxynitride perovskites, to synergistically optimize bandgap structure, dielectric behavior, and optical responsiveness for advanced functional applications[75].

In 2019, Haydous et al. conducted a comparative study on particle-based and thin film photocatalysts using different perovskite oxynitride materials for solar water splitting. The results showed that particle-based systems

exhibit higher overall photoelectrochemical activity due to better light absorption and larger surface area, while thin films demonstrate improved charge separation and carrier mobility because of their more controlled morphology. The study highlights that both forms are complementary, and their performance depends strongly on the balance between surface area effects and charge transport properties in oxynitride photocatalysts[78].

In 2020, Xu and Jiang investigated anion ordering in perovskite oxynitrides AMO_2N (A = Ba, Sr, Ca; M = Ta, Nb) using first-principles calculations combined with cluster expansion and Monte Carlo simulations. The study showed that anion arrangement strongly depends on both composition and temperature, where Ba- and Sr-based compounds favour cis-type ordering at low temperatures, while Ca-based systems tend to exhibit phase separation and stabilize only at higher temperatures. The work also reported that Nb and Ta oxynitrides exhibit similar but not identical interaction behaviours, leading to noticeable differences in anion ordering. Furthermore, calculated band gaps using the HSE06 method were in good agreement with experimental data, and the materials were confirmed to be promising dielectric candidates, highlighting the importance of anion ordering in tuning their physical properties[79].

In 2020, Wakasugi et al. reported the heteroepitaxial growth of $CaTaO_2N$ thin films on $SrTiO_3$ substrates using reactive RF magnetron sputtering. The study demonstrated that epitaxial films with different crystallographic orientations ((100) pc, (110) pc, and (111) pc can be successfully grown, with film crystallinity strongly depending on surface orientation and substrate symmetry. Among them, (110) pc-oriented films showed the highest crystallinity due to reduced domain mismatch. Improved structural quality and surface morphology were also achieved on $DyScO_3$ substrates,

highlighting the importance of lattice and symmetry matching in obtaining high-quality perovskite oxynitride thin films[80].

In 2020, Bubeck et al**.** investigated perovskite-type oxynitrides $LaTa_{1-x}Co_x(O,N)_3-\delta$ (x = 0.01, 0.03, 0.05) as potential diluted high-temperature ferromagnetic materials. The synthesized powders exhibited Curie temperatures above 600 K, with phase-pure compositions confirmed by comprehensive characterization. Magnetic measurements indicated the presence of intermediate-spin Co^{3+} ions within the ferromagnetic host matrix. The observed magnetic behaviour was associated with the interplay between the crystal structure, anionic vacancies, and the introduced cobalt ions, demonstrating the potential of cobalt-substituted perovskite oxynitrides for high-temperature ferromagnetic applications[81]**.**

In 2022, Sakata et al. synthesized solid solutions of strontium-tantalum oxynitride (SrTaO2N) and strontium-titanium oxide (SrTiO3) perovskites via a sol–gel method using alkoxide-derived Ta–Ti binary oxide gel precursors and urea as a nitriding agent. The study demonstrated that the use of sol–gel binary oxide precursors facilitate the formation of single-phase solid solutions with a highly homogeneous atomic distribution, while eliminating the use of harmful ammonia gas during nitridation. The resulting materials exhibited tunable optical band gaps and chromatic characteristics depending on the titanium content, alongside strong thermal and chemical resistance. This highlights the effectiveness of precursor design in sol–gel routes for modulating the structural, optical, and physical functionalities of multi-cation perovskite oxynitrides [82].

In 2024, Jeongsuk Seo and Kazunari Domen reviewed perovskite $AB(O,N)_3$ and layered perovskite oxynitrides as promising semiconductor

materials for visible-light-driven artificial photosynthesis and solar energy conversion. The study reported that these materials exhibit strong visible-light absorption (up to ~750 nm) and suitable band structures for photocatalytic reactions such as water splitting and hydrogen evolution. It also highlighted that defect engineering, doping, substitution, and surface modification play key roles in improving charge separation, reducing recombination, and enhancing photocatalytic efficiency and stability[83].

In 2024, Mohammadi et al. investigated Cu-containing lanthanum manganite perovskites (LaCuxMn1−xO3) to evaluate the influence of Cu incorporation and calcination temperature on their structural and redox properties. The study demonstrated that Cu incorporation modified the metal–perovskite phase boundary and promoted oxygen-vacancy formation, which influenced the redox behaviour and catalytic activity of the materials. The authors also showed that the Cu–perovskite interface played an important role in the catalytic reduction of NO by CO. These findings demonstrate that Cu incorporation into perovskite structures can significantly modify their defect chemistry, redox behaviour, and structural properties, providing useful supporting evidence for the incorporation of Cu into transition-metal perovskite systems.

In 2025, Saravanan et al. developed copper-doped barium tantalum oxynitride (Cu-doped $BaTaO_2N$) for electrochemical energy-storage applications. The material was synthesized using a soft urea synthesis method and characterized in terms of its crystal structure, morphology, and dopant composition. Defect-energy calculations were also performed to evaluate lattice stability and nitrogen fixation. The Cu-doped $BaTaO_2N$ exhibited a specific capacitance of 944 $F.g^{-1}$ at 1 $A.g^{-1}$, with a maximum energy density of 24 $Wh.kg^{-1}$ and power density of 9.8 $Kw.kg^{-1}$,

demonstrating its potential as a transition-metal-doped perovskite oxynitride for supercapacitor applications[84].

In 2025, Ravikumar et al. synthesized single-phase cobalt oxynitride (CON) to demonstrate the impacts of mixed-anion engineering. XRD, Raman, and HR-TEM analyses confirmed the co-existence of Co–O and Co–N bonding environments, while DFT calculations established optimal thermodynamic stability via body-diagonal nitrogen placement. Driven by the hybridization of O 2p and N 2p orbitals, the optical bandgap was reduced from 2.62 eV (for the parent oxide) to 2.41 eV. This orbital integration enhanced photo-induced charge dynamics, allowing the CON system to achieve ~92% dye degradation, alongside elevated H2 (1748.6 μmol g^{-1} h^{-1}) and NH3 (411.2 μmol g^{-1} h^{-1}) evolution rates, significantly outperforming individual oxide and nitride counterparts[76].

1.12 Aims of the Research

1. To synthesize novel transition-metal perovskite oxynitride compounds based on Ba, Ca, Mg, and Pb, incorporating Cu, Co, and mixed $Cu_{0.5}Co_{0.5}$ cations at the B-site using the sol–gel auto-combustion method.
2. To investigate the relationships between the composition, structural characteristics, and physical properties of the synthesized oxynitride perovskites.
3. To evaluate the potential of the synthesized perovskite oxynitrides for solar-cell applications through photovoltaic device performance.

Chapter Two

Experimental Methodology

2 Experimental Methodology

2.1 Chemicals

Prior to initiating the experimental procedures, all necessary raw chemical substances, starting materials, and organic solvents required for the synthesis were acquired. The specific technical details are tabulated in Table (2-1):

Table (2-1): Chemicals

NO	Substance	Formula	Company	Purity
1	Barium nitrate	$Ba(NO_3)_2$	Himedia	99%
2	Cobalt (II) nitrate hexahydrate	$Co(NO_3)_2.6H_2O$	Himedia	97%
3	Cupric nitrate trihydrate	$Cu(NO_3)_2.3H_2O$	Loba Chemie	95%
4	Magnesium nitrate hexahydrate	$Mg(NO_3)_2.6H_2O$	Himedia	95%
5	Lead (II) nitrate	$Pb(NO_3)_2$	Thomas Baker	99%
6	Calcium nitrate tetrahydrate	$Ca(NO_3)_2.4H_2O$	Tekkim	98%
7	Deionized water	H_2O		
8	Citric acid	$C_6H_8O_7$	ACS Chemicals	99%
9	Urea	$NH_2.CO.NH_2$	Thomas Baker	99%
10	Ethanol	C_2H_5OH	RCI Labscan	99%

2.2 Instruments

The main instruments employed in this study, along with their specifications, are presented below.

Table (2-2): Instruments

NO	Instrument	Model	Company supplied	Location
1	Sensitive Balance	BL 210S	Sartorius, Germany	University of Al Qadisiyah-Iraq
2	Centrifuge	CL008	Labtech, Korea	University of Al Qadisiyah-Iraq
3	Muffle Furnace	K-MF03	K&K scientific supplier, Korea	University of Al Qadisiyah-Iraq
4	Ultrasound path	Power sonic 405	Hwashin, Korea	University of Al Qadisiyah-Iraq
5	Hot plate & Magnetic stirrer	LMS-1003	Labtech, Korea	University of Al Qadisiyah-Iraq
6	UV-Visible Spectrophotometer	PC 1650	Shimadzu, Japan	University of Al Qadisiyah-Iraq
7	Oven	K-MF03	K&K scientific supplier, Korea	University of Al Qadisiyah-Iraq
8	Energy Diseper x-ray Spectroscopy (EDX)	Mira (III)	Czech Republic (Tescen)	Phi NanoScience Center-Iraq
9	X-Ray Diffractometer (XRD)	D2 Phaser	Bruker AXS Gmbh, Germany	Phi NanoScience Center-Iraq
10	Field Emission Scanning Electronmicroscope (FE-SEM)	MIRA3	Tescan, China	Phi NanoScience Center-Iraq
11	Hall Effect	HMS-3000	Ecopia South Korea	Phi NanoScience Center-Iraq
12	I-V Characterization	Keithley 2400	Keithley/USA	Phi NanoScience Center-Iraq

2.3 Synthesizee of Oxynitride Nanoparticles by Sol–gel Method

All twelve oxynitride nanoparticles were synthesized via the sol–gel auto-combustion method. Citric acid was employed as a chelating agent at a 1:1 molar ratio relative to total metal cations, while urea was incorporated at a high molar ratio of 10:1 urea was used as a combustion fuel and was intended to provide an in-situ nitrogen source during thermal treatment.

2.3.1 Ba-Based Oxynitride Perovskites

$BaCuO_2N$, $BaCoO_2N$, and $BaCu_{0.5}Co_{0.5}O_2N$ nanoparticles were synthesized via a urea-assisted sol–gel auto-combustion route. In the preparation of $BaCuO_2N$, 7.41 g of barium nitrate and 6.85 g of copper nitrate trihydrate were dissolved in 100 mL of deionized water, followed by the addition of 10.89 g of citric acid. Subsequently, 34.52 g of urea was gradually introduced while the mixture was maintained under continuous magnetic stirring at 50 °C. For $BaCoO_2N$, 7.55 g of barium nitrate, 8.41 g of cobalt nitrate hexahydrate, and 11.10 g of citric acid were dissolved under identical conditions, followed by the addition of 34.72 g of urea. For the mixed-metal composition $BaCu_{0.5}Co_{0.5}O_2N$, 7.88 g of barium nitrate, 3.64 g of copper nitrate trihydrate, and 4.39 g of cobalt nitrate hexahydrate were dissolved in 100 mL of deionized water. Then, 11.60 g of anhydrous citric acid and 36.23 g of urea were added successively. The resulting solutions were stirred at 50 °C until complete homogenization.

Following homogenization, each precursor solution was heated to 110 °C with continuous stirring, allowing gradual evaporation of water, gel formation, and subsequent self-combustion to produce porous precursor powders. The powders were gently ground in an agate mortar and transferred to covered alumina crucibles. Thermal treatment was

performed in a laboratory muffle furnace without an external gas flow. The samples were first heated at 5 °C min^{-1} to 400 °C and maintained at this temperature for 2 h. The temperature was then increased at the same rate to 700 °C and held for 3 h. The excess urea functioned as the combustion fuel and was intended to act as an in-situ nitrogen source during the thermal treatment. After completion of the 700 °C treatment, the furnace was turned off, and the covered crucibles remained inside the furnace for natural cooling to room temperature until the following day. The obtained powders were finally collected and finely ground prior to characterization.

2.3.2 Ca-Based Oxynitride Perovskites

The Ca-based oxynitride perovskite nanoparticles, $CaCuO_2N$, $CaCoO_2N$, and $CaCu_{0.5}Co_{0.5}O_2N$, were obtained through the same urea-assisted sol–gel auto-combustion approach, with calcium nitrate used as the A-site precursor. For $CaCuO_2N$, 12.34 g of calcium nitrate, 12.65 g of copper nitrate trihydrate, and 20.13 g of citric acid were dissolved in 100 mL of deionized water. A quantity of 62.92 g of urea was then added gradually while the solution was continuously stirred at 50 °C. In the case of $CaCoO_2N$, the precursor mixture consisted of 12.81 g of calcium nitrate, 15.79 g of cobalt nitrate hexahydrate, and 20.85 g of citric acid dissolved in 100 mL of deionized water, followed by the addition of 65.16 g of urea. For $CaCu_{0.5}Co_{0.5}O_2N$, 12.56 g of calcium nitrate was combined with 6.43 g of copper nitrate trihydrate and 7.74 g of cobalt nitrate hexahydrate in 100 mL of deionized water. After dissolution, 20.45 g of anhydrous citric acid and 63.92 g of urea were incorporated. All precursor systems were maintained under stirring at 50 °C until uniform solutions were obtained.

The homogenized solutions were subsequently heated to 110 °C while stirring was continued. This stage promoted solvent evaporation, formation of the gel, and auto-combustion, resulting in porous precursor materials. After

cooling, the precursor powders were pulverized with an agate mortar and pestle and loaded into covered alumina crucibles. The thermal processing was carried out in a laboratory muffle furnace under conditions without external gas flow. Initially, the powders were heated from room temperature to 400 °C at 5 °C min^{-1} and held for 2 h. They were then heated to 700 °C at the same rate and maintained for a further 3 h. During this process, the excess urea acted as the combustion fuel and was intended to supply nitrogen in situ. Upon completion of the heat treatment, the furnace was switched off, and the crucibles were allowed to cool naturally inside the furnace to room temperature until the next day. The final powders were then recovered and subjected to further grinding before characterization.

2.3.3 Mg-Based Oxynitride Perovskites

$MgCuO_2N$, $MgCoO_2N$, and $MgCu_{0.5}Co_{0.5}O_2N$ were synthesized using a urea-assisted sol–gel auto-combustion method. For the $MgCuO_2N$ composition, 13.41 g of magnesium nitrate, 12.63 g of copper nitrate trihydrate, and 20.09 g of citric acid were dissolved in 100 mL of deionized water. Subsequently, 62.75 g of urea was added gradually while the mixture was stirred continuously at 50 °C. The $MgCoO_2N$ precursor was prepared by dissolving 13.89 g of magnesium nitrate, 15.77 g of cobalt nitrate hexahydrate, and 20.81 g of citric acid in 100 mL of deionized water, followed by the addition of 65.06 g of urea under continuous stirring. For the bimetallic $MgCu_{0.5}Co_{0.5}O_2N$ composition, 13.64 g of magnesium nitrate, 6.43 g of copper nitrate trihydrate, and 7.74 g of cobalt nitrate hexahydrate were dissolved in 100 mL of deionized water. The solution was then supplemented with 20.45 g of anhydrous citric acid and 63.92 g of urea. In each preparation, stirring at 50 °C was continued until the precursor components were completely homogenized.

The resulting precursor solutions were transferred to the gelation stage by increasing the temperature to 110 °C under continuous magnetic stirring. Evaporation of the solvent at this temperature led to gel formation followed by self-combustion, producing porous precursor powders. These powders were subsequently crushed and homogenized using an agate mortar and pestle before being placed in covered alumina crucibles. The powders underwent a two-step thermal treatment in a laboratory muffle furnace without external gas flow. The first step involved heating to 400 °C at a rate of 5 °C min^{-1} and maintaining this temperature for 2 h. In the second step, the temperature was raised to 700 °C at 5 °C min^{-1} and held for 3 h. The excess urea present in the precursor served as the combustion fuel and was intended to provide an in-situ nitrogen source during heating. At the end of the 700 °C treatment, the furnace was switched off, and the covered crucibles were retained inside the furnace for gradual cooling to room temperature until the following day. The synthesized powders were subsequently collected and finely ground in an agate mortar before characterization.

2.3.4 Pb-Based Oxynitride Perovskites

$PbCuO_2N$, $PbCoO_2N$, and $PbCu_{0.5}Co_{0.5}O_2N$ nanoparticles were prepared through a urea-assisted sol–gel auto-combustion process. For $PbCuO_2N$, 7.32 g of lead nitrate, 5.34 g of copper nitrate trihydrate, and 8.49 g of citric acid were dissolved in 100 mL of deionized water. Then, 26.54 g of urea was gradually added to the solution while magnetic stirring was maintained at 50 °C. $PbCoO_2N$ was synthesized from 7.43 g of lead nitrate, 6.53 g of cobalt nitrate hexahydrate, and 8.62 g of citric acid dissolved in the same volume of deionized water, followed by the incorporation of 26.94 g of urea under the same stirring conditions. For $PbCu_{0.5}Co_{0.5}O_2N$, 7.39 g of lead nitrate, 2.75 g of copper nitrate trihydrate, and 3.24 g of cobalt nitrate hexahydrate were dissolved in 100 mL of deionized water. Afterward, 8.57 g of anhydrous citric

acid and 26.80 g of urea were added. The precursor mixtures were stirred continuously at 50 °C until homogeneous solutions were obtained.

The prepared solutions were then subjected to heating at 110 °C under continuous stirring. Water evaporation at this stage resulted in gel formation and subsequent self-combustion, yielding porous precursor powders. The powders were ground using an agate mortar and pestle and subsequently placed in covered alumina crucibles for thermal treatment. Calcination was conducted in a laboratory muffle furnace without the introduction of an external gas. The temperature was increased at 5 °C min^{-1} to 400 °C, where it was maintained for 2 h, and was subsequently raised at the same heating rate to 700 °C and held for 3 h. The excess urea served as the combustion fuel and was intended to contribute nitrogen in situ during the thermal treatment. Following the 700 °C heating stage, the furnace was switched off, and the covered crucibles were left inside the furnace to cool naturally to room temperature until the following day. The obtained products were finally collected and ground thoroughly using an agate mortar and pestle before characterization.

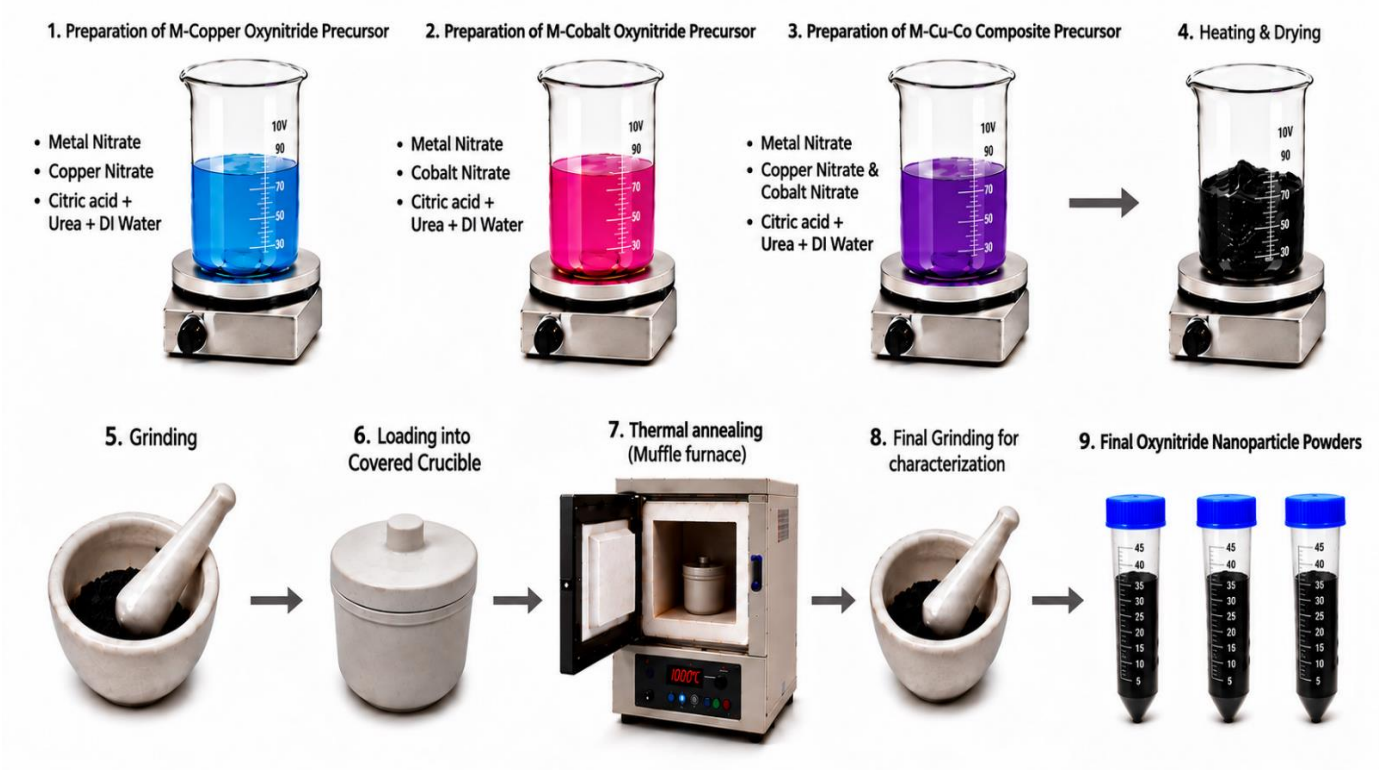


Fig. (2-1): Schematic Flow Diagram of the General Sol-Gel Methodology for Synthesizing Various Oxynitride Perovskites (M = Ba, Ca, Mg, Pb).

2.4 Thin Film Deposition and Hall Effect Measurements

For each composition, 50 mg of the oxynitride nanoparticles was dispersed in 10 mL of dimethyl sulfoxide (DMSO) and ultrasonicated for 60 min before the commercial 2 × 2 cm^2 n-type silicon substrates were sequentially cleaned with deionized water, ethanol and acetone and dried. The suspensions were sonicated for a short time prior to deposition to re-suspend settled particles. An amount of about 150 µL of each suspension was dropped on the centre of the substrate and spin-coated for 60 s at 2000 rpm. 5 cycles of coating/drying were performed at 100 °C for 10 minutes. The films were then left at 100 °C for 30 min and allowed to cool down to room temperature without any further treatment at high temperature.

The positive Hall coefficients indicated p-type semiconducting behavior of the synthesized oxynitrides nanoparticles which has been exploited to form oxynitride/n-Si heterojunctions using the synthesized oxynitride films deposited on the n-type Si substrates. After deposition of the oxynitride films on the silicon substrates, aluminum (Al) electrodes were deposited onto the surface of the oxynitride films using a dedicated mask for solar-cell fabrication. Copper wires were then connected to the electrodes using a thin layer of conductive silver adhesive to establish electrical contact. The photovoltaic characteristics of the fabricated oxynitride-based devices were evaluated from current density–voltage (J–V) measurements using a Keithley 2400 source-measure unit. A tungsten–halogen lamp was used as the light source, and the incident light intensity was set to 100 mW cm^{-2}. The voltage was swept from 0 to 1 V. The J–V characteristics were used to determine the short-circuit current density (Jsc), open-circuit voltage (Voc), maximum current density (Jmax), maximum voltage (Vmax), fill factor (FF), and power conversion efficiency (PCE).

The fill factor was calculated using equation (1):

$$FF = (Jmax \times Vmax)/(Jsc \times Voc) \ldots\ldots (1)$$

The power conversion efficiency was calculated using equation (2):

$$PCE (\%) = (Jsc \times Voc \times FF/P_{in}) \times 100 \ldots\ldots (2)$$

where P_{in} is the incident optical power density.

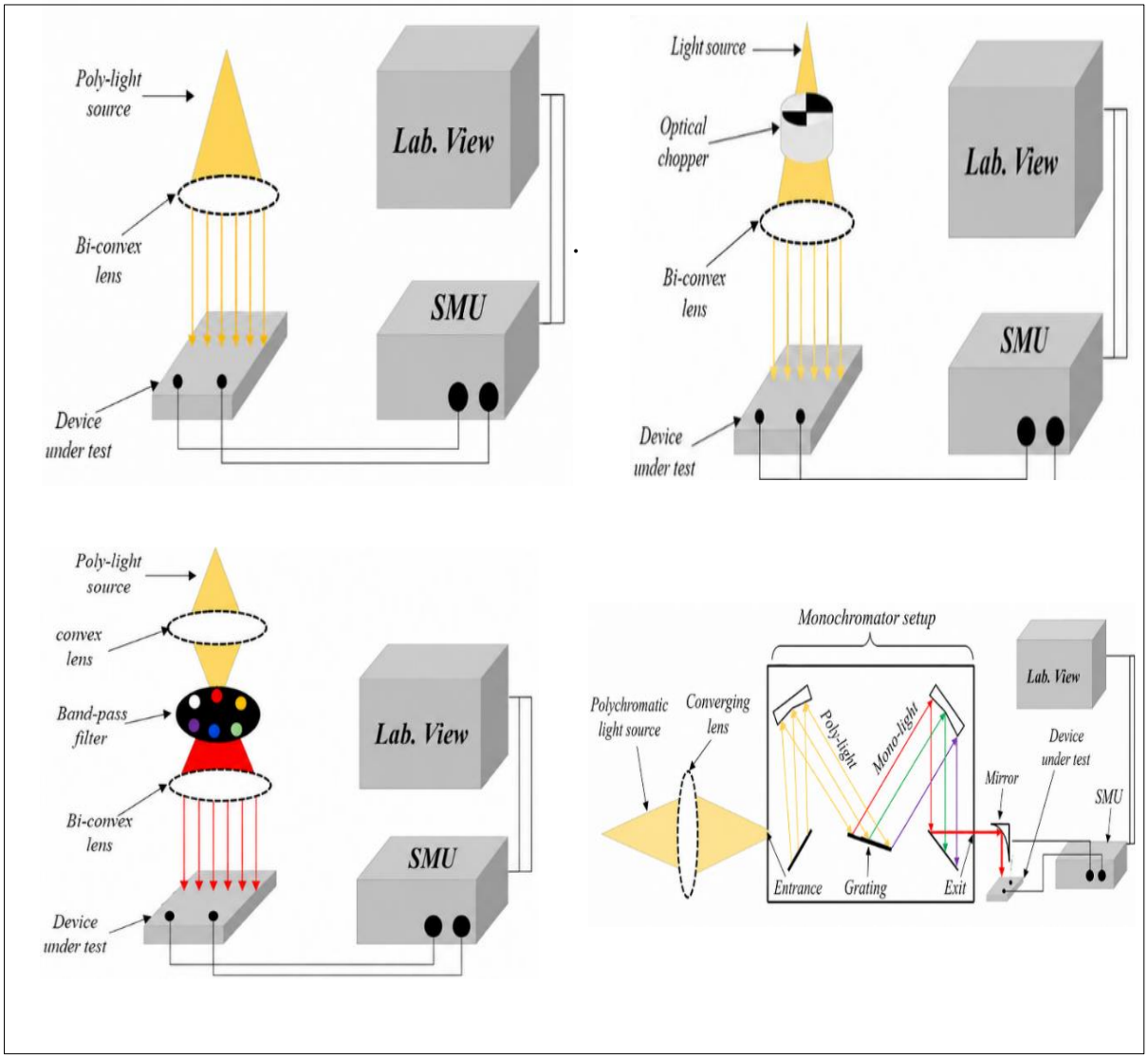


Fig. (2-2): Solar cell testing system process.

Chapter Three
Results and Discussion

3. Results and Discussion

3.1 Structural and Microstructural Analysis

3.1.1 X-ray Diffraction of Ba-based Oxynitride Perovskites

The XRD diffractograms of the synthesized Ba-based and Ca-based oxynitride perovskite powders are displayed in Fig. (3-1). For the barium series, $BaCuO_2N$ exhibited a maximum diffraction reflection peak at $2\theta = 23.47844°$ (d = 3.78602 Å) corresponding to the (2 1 0) plane. $BaCoO_2N$ showed its primary peak at $2\theta = 23.93842°$ (d = 3.71430 Å) assigned to the (1 -1 1) plane, while the mixed $BaCu_{0.5}Co_{0.5}O_2N$ exhibited its maximum peak at $2\theta = 23.89408°$ (d = 3.72110 Å) related to the (1 1 0) plane.

The change in the diffraction peak positions and the different indexed crystal structures indicate that changing the B-site composition affected the crystal lattice. $BaCuO_2N$ and $BaCoO_2N$ were indexed in the triclinic P1 space group, whereas $BaCu_{0.5}Co_{0.5}O_2N$ was indexed in the monoclinic P2/m space group. This change in symmetry can be attributed to the different structural arrangement produced by the simultaneous presence of Cu and Co at the B-site. Similar XRD studies of perovskite systems have shown that substitution at the B-site can modify lattice parameters and, in some cases, induce a change in crystal symmetry[85].

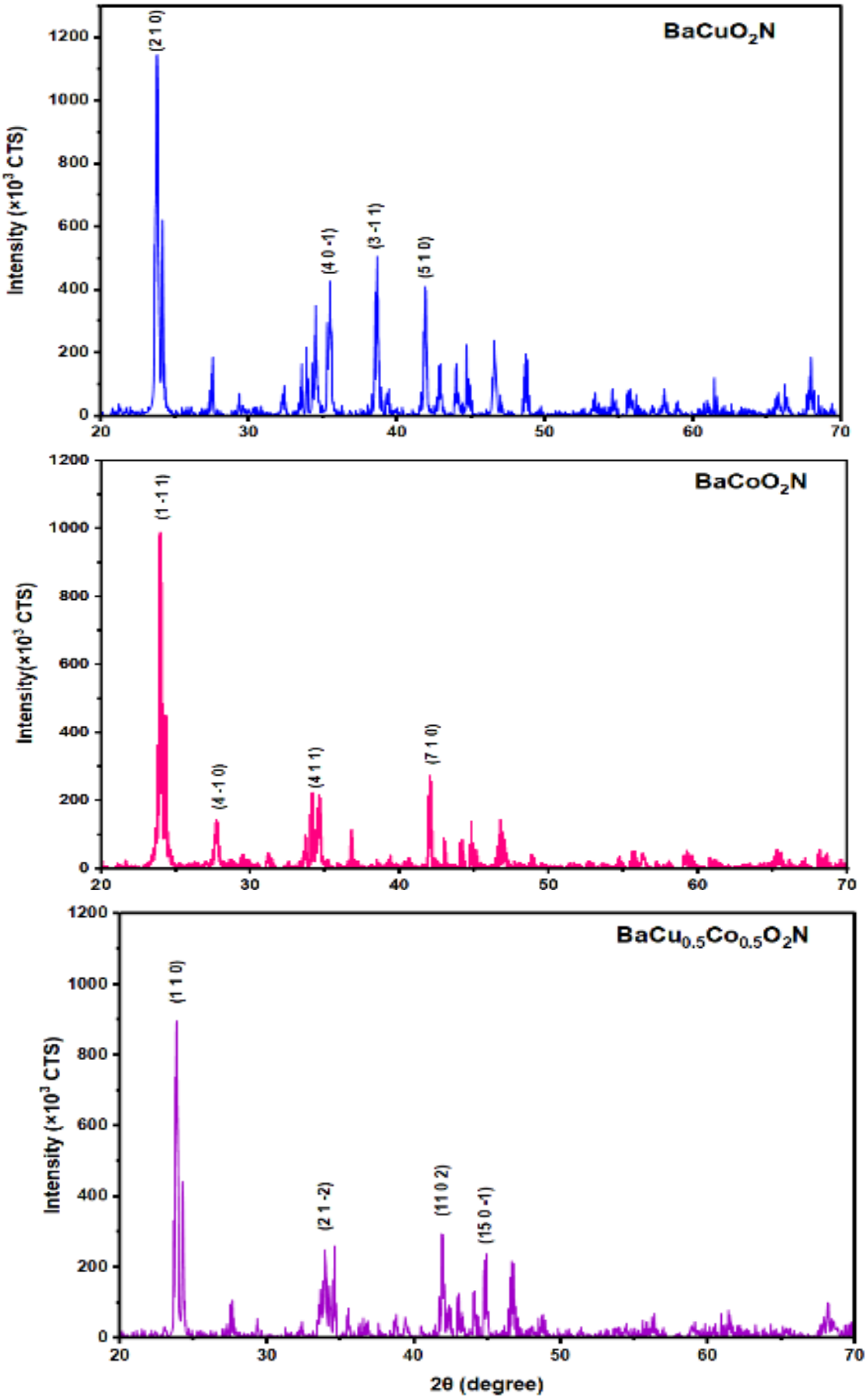


Fig. (3-1): X-ray Diffraction Patterns of the Synthesized Ba-Based Oxynitride Perovskite via Sol–Gel Auto-Combustion Technique.

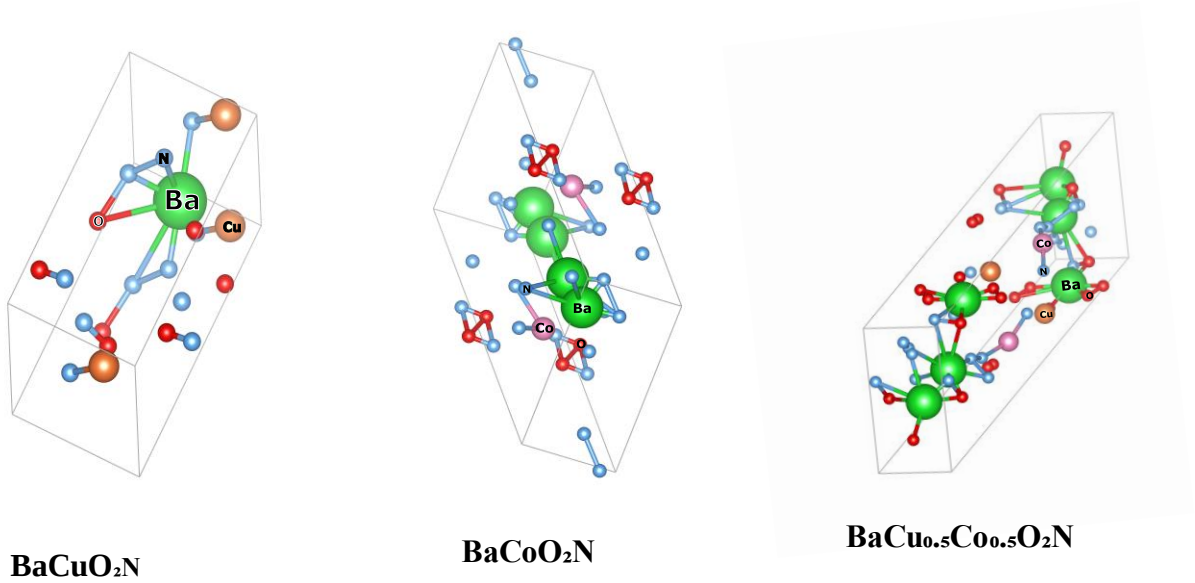
The structural change in the mixed composition is also reflected in the calculated unit-cell parameters. The unit-cell volume increased from 229.65 Å^3 for $BaCuO_2N$ to 554.53 Å^3 for $BaCoO_2N$ and 937.41 Å^3 for $BaCu_{0.5}Co_{0.5}O_2N$. Thus, the change from a single B-site cation to the mixed Cu/Co composition is associated with a substantially different unit-cell geometry. The XRD results therefore indicate that the incorporation of Cu and Co in different oxynitrides modifies the lattice dimensions and crystal symmetry of the Ba-based oxynitride perovskites.

The crystallinity values were 66.9%, 80.5%, and 64.1% for $BaCuO_2N$, $BaCoO_2N$, and $BaCu_{0.5}Co_{0.5}O_2N$, respectively. The higher crystallinity of $BaCoO_2N$ indicates a more pronounced crystalline ordering under the applied synthesis conditions, whereas the lower value for the mixed composition indicates comparatively lower crystalline ordering. The mixed composition also exhibited a slightly higher dislocation density (1.33×10^{-5} nm^{-2}) than $BaCoO_2N$ (1.29×10^{-5} nm^{-2}), which is consistent with the difference in their crystallinity values. XRD crystallinity and structural parameters are commonly evaluated from the intensity, position, and profile of diffraction peaks.

The calculated density decreased from 3.57 g·cm^{-3} for $BaCuO_2N$ to 3.15 g·cm^{-3} for $BaCoO_2N$ and 3.03 g·cm^{-3} for $BaCu_{0.5}Co_{0.5}O_2N$. This variation accompanies the differences in the calculated unit-cell parameters and volumes among the three oxynitrides

Table (3-1): X-ray Data of $BaCuO_2N$, $BaCoO_2N$, and $BaCu_{0.5}Co_{0.5}O_2N$ Oxynitride Perovskite Synthesized Via Sol–Gel Auto-Combustion Technique.

Parameter	$BaCuO_2N$	$BaCoO_2N$	$BaCu_{0.5}Co_{0.5}O_2N$
Dislocation density (nm^{-2})	1.35×10^{-5}	1.29×10^{-5}	1.33×10^{-5}
Crystallinity %	66.9%	80.5%	64.1%
Space Group	P1	P1	P2/m
Cell parameters	**α** 106.12	95.66	90.00
	β 90.41	96.98	91.03
	Ɣ 88.79	80.07	90.00
	a(Å) 11.89	15.27	33.30
	b(Å) 4.94	8.39	3.75
	c(Å) 4.06	4.43	7.49
Cell volume ($Å^3$)	229.65	554.53	937.41
No. Unit cell	4.58×10^7	2.04×10^7	1.15×10^7
Density ($g.cm^{-3}$)	3.57	3.15	3.03



$BaCuO_2N$ **$BaCoO_2N$** **$BaCu_{0.5}Co_{0.5}O_2N$**

Fig. (3-2): X-ray Crystal Structures of Synthesized Ba-Based Oxynitride Perovskite via Sol–Gel Auto-Combustion Technique.

3.1.2 X-ray Diffraction of Ca-based Oxynitride Perovskites

The XRD patterns of the Ca-based oxynitride perovskites are presented in Fig. (3-3). $CaCuO_2N$ exhibited its predominant diffraction peak at approximately $2\theta = 38.2°$ corresponding to the (1 3 1) plane, while $CaCoO_2N$ showed its predominant peak at approximately $2\theta = 7.2°$ corresponding to the (0 1 0) plane. $CaCu_{0.5}Co_{0.5}O_2N$ exhibited its predominant peak at approximately $2\theta = 35.5°$ corresponding to the (1 0 2) plane. The differences in the peak positions indicate that changing the B-site composition from Cu to Co and to the mixed Cu/Co composition altered the interplanar spacing and lattice arrangement of the Ca-based compounds. Since peak position in XRD is related to interplanar spacing through Bragg's law, the different peak positions reflect differences in the crystal lattice between the oxynitrides.

In contrast to the Ba-based compounds, all three Ca-based oxynitrides were indexed in the triclinic P1 space group. This means that the change in B-site composition did not produce a change in the indexed crystal symmetry for the Ca-based series. However, the lattice parameters and unit-cell volumes changed considerably: 465.52 $Å^3$ for $CaCuO_2N$, 923.60 $Å^3$ for $CaCoO_2N$, and 973.33 $Å^3$ for $CaCu_{0.5}Co_{0.5}O_2N$. Therefore, the substitution of Cu, Co, or Cu/Co affected the lattice dimensions without changing the indexed P1 symmetry. B-site substitution is known to modify lattice parameters and can influence crystal symmetry depending on the structural system[86].

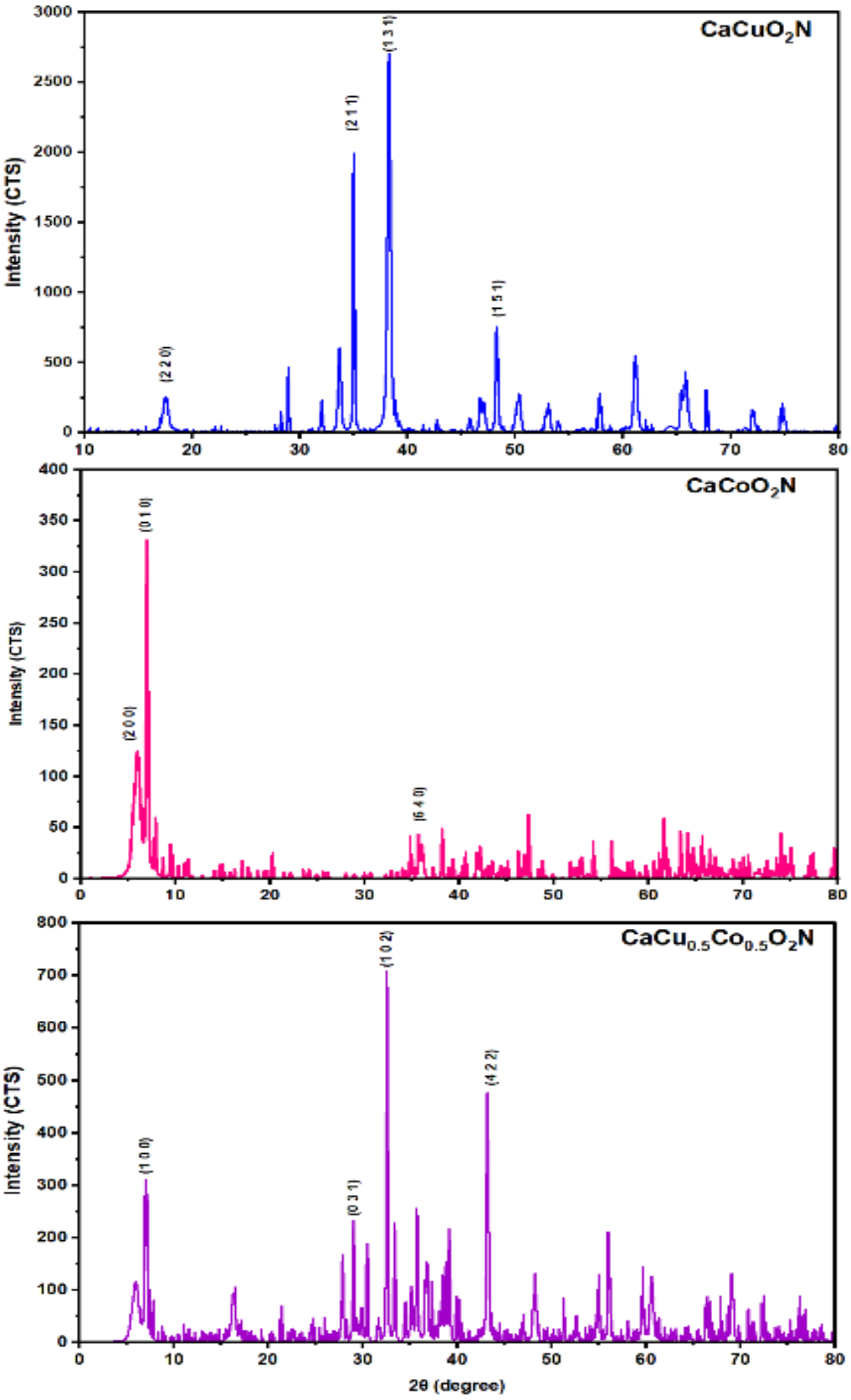


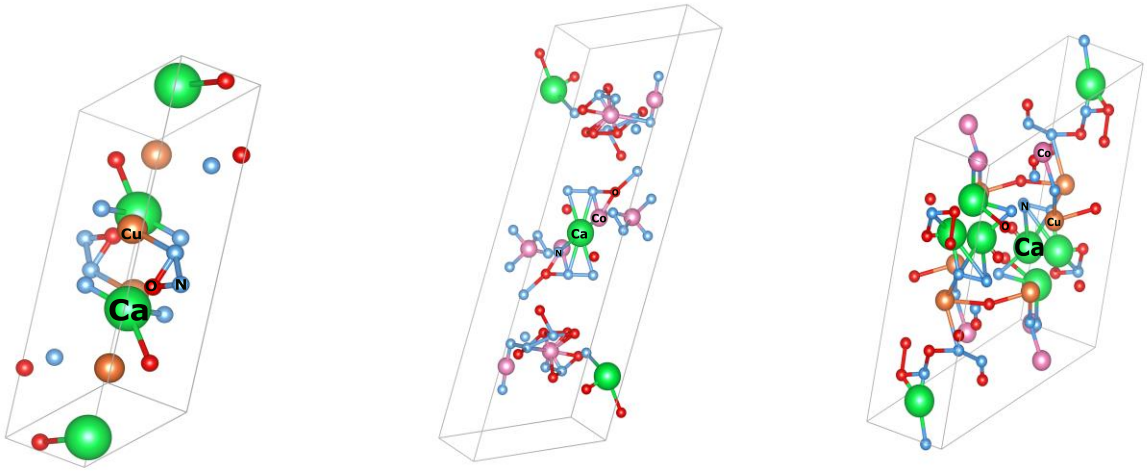
Fig. (3-3): X-ray Diffraction Patterns of the Synthesized Ca-Based Oxynitride Via Sol–Gel Auto-Combustion Technique.

The crystallinity values were 83.05%, 75.65%, and 77.26% for $CaCuO_2N$, $CaCoO_2N$, and $CaCu_{0.5}Co_{0.5}O_2N$, respectively. $CaCuO_2N$ exhibited the highest crystallinity, indicating the most pronounced crystalline ordering among the Ca-based oxynitrides under the applied preparation conditions. $CaCoO_2N$ showed the lowest crystallinity, while the mixed composition showed an intermediate value. The dislocation densities were 4.00×10^{-5}, 3.73×10^{-5}, and 4.01×10^{-5} nm^{-2}, respectively. The relatively small variation in dislocation density indicates that this parameter changed only slightly among the three Ca-based oxynitrides.

The calculated densities were 2.13 $g \cdot cm^{-3}$ for $CaCuO_2N$, 2.08 $g \cdot cm^{-3}$ for $CaCoO_2N$, and 2.26 $g \cdot cm^{-3}$ for $CaCu_{0.5}Co_{0.5}O_2N$. The higher density of the mixed composition occurs together with its larger calculated unit-cell volume (973.33 $Å^3$) and its different lattice parameters, showing that the density variation is associated with the crystallographic characteristics of each composition

Table (3-2): X-ray Data of $CaCuO_2N$, $CaCoO_2N$, and $CaCu_{0.5}Co_{0.5}O_2N$ Oxynitride Perovskite Synthesized by Via Sol–Gel Auto-Combustion Technique.

Parameters	$CaCuO_2N$	$CaCoO_2N$	$CaCu_{0.5}Co_{0.5}O_2N$
Dislocation density (nm^{-2})	4×10^{-5}	3.73×10^{-5}	4.01×10^{-5}
Crystallinity (%)	83.05%	75.65%	77.26%
Space Group	P1	P1	P1
Cell Parameters	**α** 91.25	90.89	101.14
	β 92.70	92.44	95.74
	ɣ 76.12	92.37	63.04
	a(Å) 13.09	26.12	13.88
	b(Å) 12.75	12.59	13.73
	c(Å) 2.87	2.81	5.83
Cell volume ($Å^3$)	465.52	923.60	973.33
No. Unit cell	4.44×10^6	2.49×10^6	2.12×10^6
Density ($g.cm^{-3}$)	2.13	2.08	2.26



$CaCuO_2N$ **$CaCoO_2N$** **$CaCu_{0.5}Co_{0.5}O_2N$**

Fig. (3-4): X-ray Crystal Structures of Synthesized Ca-Based Oxynitride Perovskite Via Sol–Gel Auto-Combustion Technique.

3.1.3 X-ray Diffraction of Mg-Based Oxynitride Perovskites

The XRD patterns of the Mg-based oxynitride nanoparticles ($MgCuO_2N$, $MgCoO_2N$, and $MgCu_{0.5}Co_{0.5}O_2N$), show clear differences in the positions and intensities of the diffraction reflections, indicating changes in the crystal structure with variation in the B-site cation composition. For $MgCuO_2N$, the indexed diffraction pattern corresponds to the P2/m space group, with a crystallinity of 79.22% and a unit-cell volume of 762.69 $Å^3$. When Cu was replaced by Co in $MgCoO_2N$, the space group changed to P1, while the unit-cell volume decreased to 662.18 $Å^3$ and the crystallinity increased to 85.28%. This change indicates that replacing Cu with Co affected the arrangement of the crystal lattice, resulting in a smaller unit cell and a higher calculated crystallinity.

For the mixed $MgCu_{0.5}Co_{0.5}O_2N$ nanoparticles, the structure remained within the P1 space group, while the unit-cell volume decreased further to 450.93 $Å^3$. At the same time, the crystallinity increased to 88.01%, which is the highest value among the three Mg-based oxynitride nanoparticles. The dislocation density also decreased from 3.68×10^{-5} nm^{-2} for $MgCuO_2N$ to 2.98×10^{-5} nm^{-2} for $MgCu_{0.5}Co_{0.5}O_2N$.

These structural changes can be related to the effect of cation composition and O/N ordering on the crystal lattice of perovskite oxynitride nanomaterials. Previous studies have shown that the ordering of oxygen and nitrogen in perovskite oxynitrides can influence the local crystal structure and the arrangement of the metal–anion coordination environment[87]. Therefore, the changes observed in the present Mg-based oxynitride nanoparticles can be associated with changes in the crystal-lattice arrangement resulting from the different Cu/Co oxynitrides.

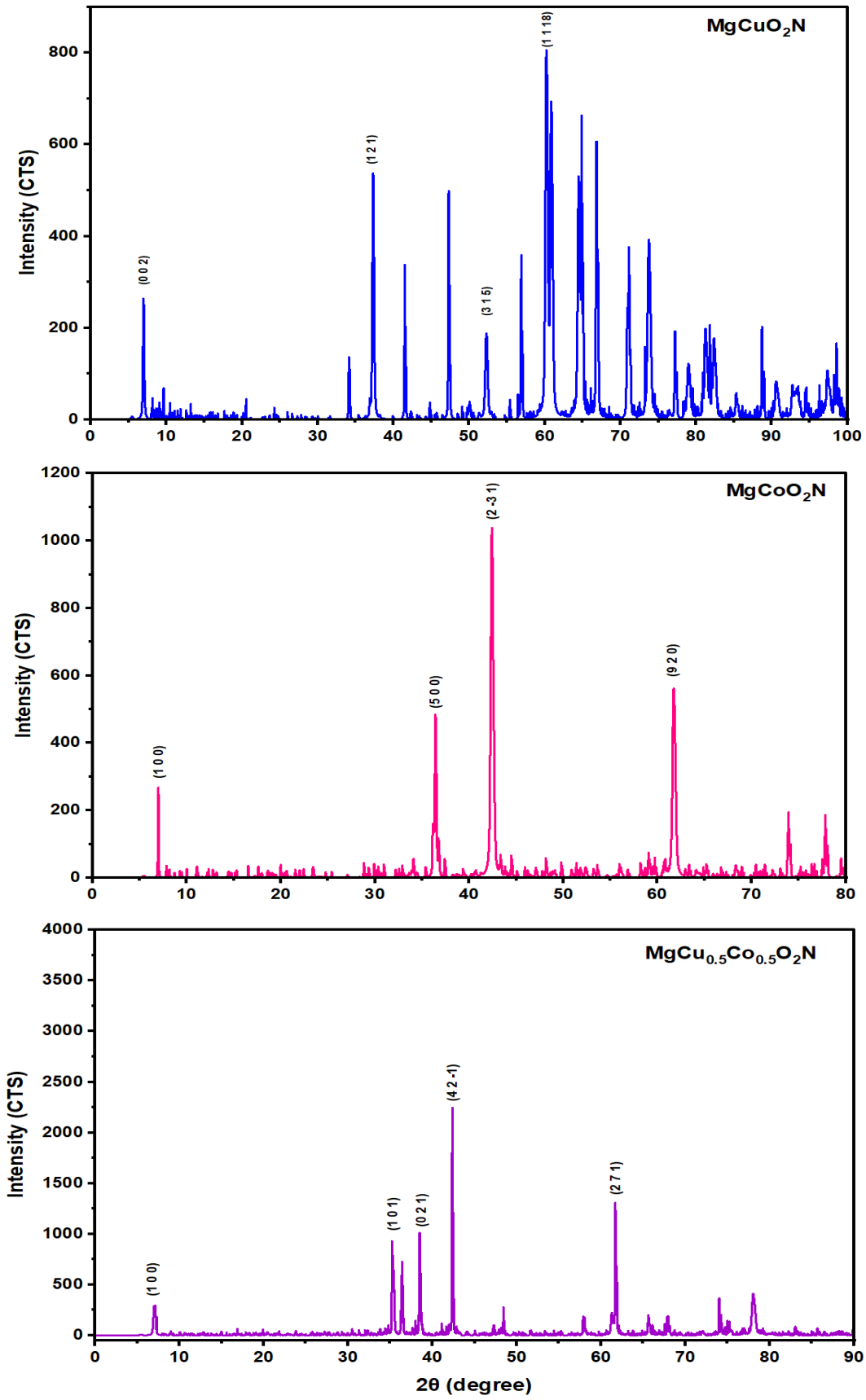
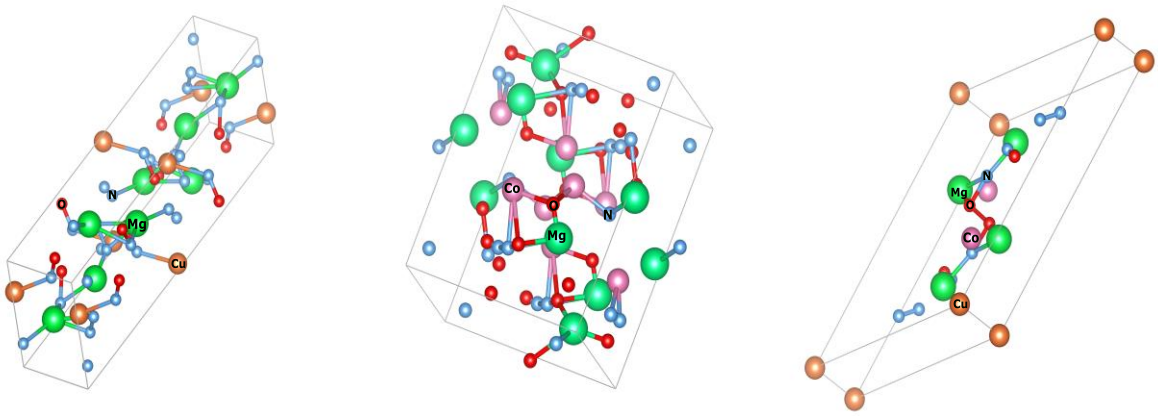


Fig. (3-5): X-ray Diffraction Patterns of the Synthesized Mg-Based oxynitride Perovskites via Sol-Gel Auto-Combustion Technique.

The XRD results indicate that incorporation of Co and the combination of (Cu and Co) produced measurable changes in the crystal structure of the Mg-based oxynitride nanoparticles. The mixed $MgCu_{0.5}Co_{0.5}O_2N$ nanoparticles exhibited the highest calculated crystallinity (88.01%), the lowest dislocation density (2.98×10^{-5} nm^{-2}), and the smallest unit-cell volume (450.93 $Å^3$) among the three Mg-based nanomaterials.

Table (3-3): X-ray data of $MgCuO_2N$, $MgCoO_2N$, and $MgCu_{0.5}Co_{0.5}O_2N$ oxynitride perovskite synthesized via Sol–Gel Auto-Combustion.

Parameters	**$MgCuO_2N$**		**$MgCoO_2N$**	**$MgCu_{0.5}Co_{0.5}O_2N$**
Dislocation density(nm^{-2})	$3.68\ 10^{-5}$		$2.96\ 10^{-5}$	$2.98\ 10^{-5}$
Crystallinity (%)	79.22		85.28%	88.01%
Space group	P2/m		P1	P1
Cell parameters	**α**	90	92.35	94.03
	β	129.18	96.72	91.75
	ɣ	90	63.07	61.69
	a(Å)	33.22	14.32	14.18
	b(Å)	5.26	13.26	13.90
	c(Å)	5.62	3.93	2.60
Cell volume ($Å^3$)	762.69		662.18	450.93
No. Unit cell	3.07×10^6		4.90×10^6	7.13×10^6
Density ($g.cm^{-3}$)	2.33		2.26	2.42



$MgCuO_2N$ **$MgCoO_2N$** **$MgCu_{0.5}Co_{0.5}O_2N$**

Fig. (3-6): X-ray crystal structures of synthesized Mg-Based oxynitride perovskite via sol–gel Auto-Combustion technique.

3.1.4 X-ray Diffraction of Pb-Based Oxynitride Perovskites

The XRD patterns of the Pb-based oxynitride nanoparticles, $PbCuO_2N$, $PbCoO_2N$, and $PbCu_{0.5}Co_{0.5}O_2N$, also show noticeable changes in the diffraction patterns with variation in the Cu/Co composition. For $PbCuO_2N$, the indexed structure belongs to the P1 space group, with a crystallinity of 73.43% and a unit-cell volume of 299.95 $Å^3$.

After replacing Cu with Co, $PbCoO_2N$ retained the P1 space group, while its unit-cell volume decreased to 223.50 $Å^3$. In contrast, the calculated crystallinity increased from 73.43% to 88.81%, while the dislocation density decreased from 4.37×10^{-5} to 3.39×10^{-5} nm^{-2}. These changes indicate that the Cu-to-Co substitution modified the crystal-lattice arrangement of the Pb-based oxynitride nanoparticles.

A more pronounced structural change was observed for the mixed $PbCu_{0.5}Co_{0.5}O_2N$ nanoparticles. In this composition, the space group changed from P1 for the single-Cu and single-Co oxynitrides to P2/m. The unit-cell volume increased substantially to 830.70 $Å^3$, while the dislocation density increased to 1.30×10^{-4} nm^{-2}. The calculated crystallinity was 84.41%, which was lower than that of $PbCoO_2N$ but higher than that of $PbCuO_2N$.

The change in crystal structure observed for the mixed Pb-based nanomaterial can be discussed in terms of the effect of cation composition and anion ordering on the perovskite oxynitride lattice. Previous studies have demonstrated that O/N ordering is an important structural factor in perovskite oxynitrides and that changes in cation composition can influence the preferred anion ordering and crystal structure[88].

In particular, computational studies of perovskite oxynitrides have included Pb-containing oxynitrides and demonstrated that the stability and structural arrangement of these materials depend on the cation combination and anion ordering.

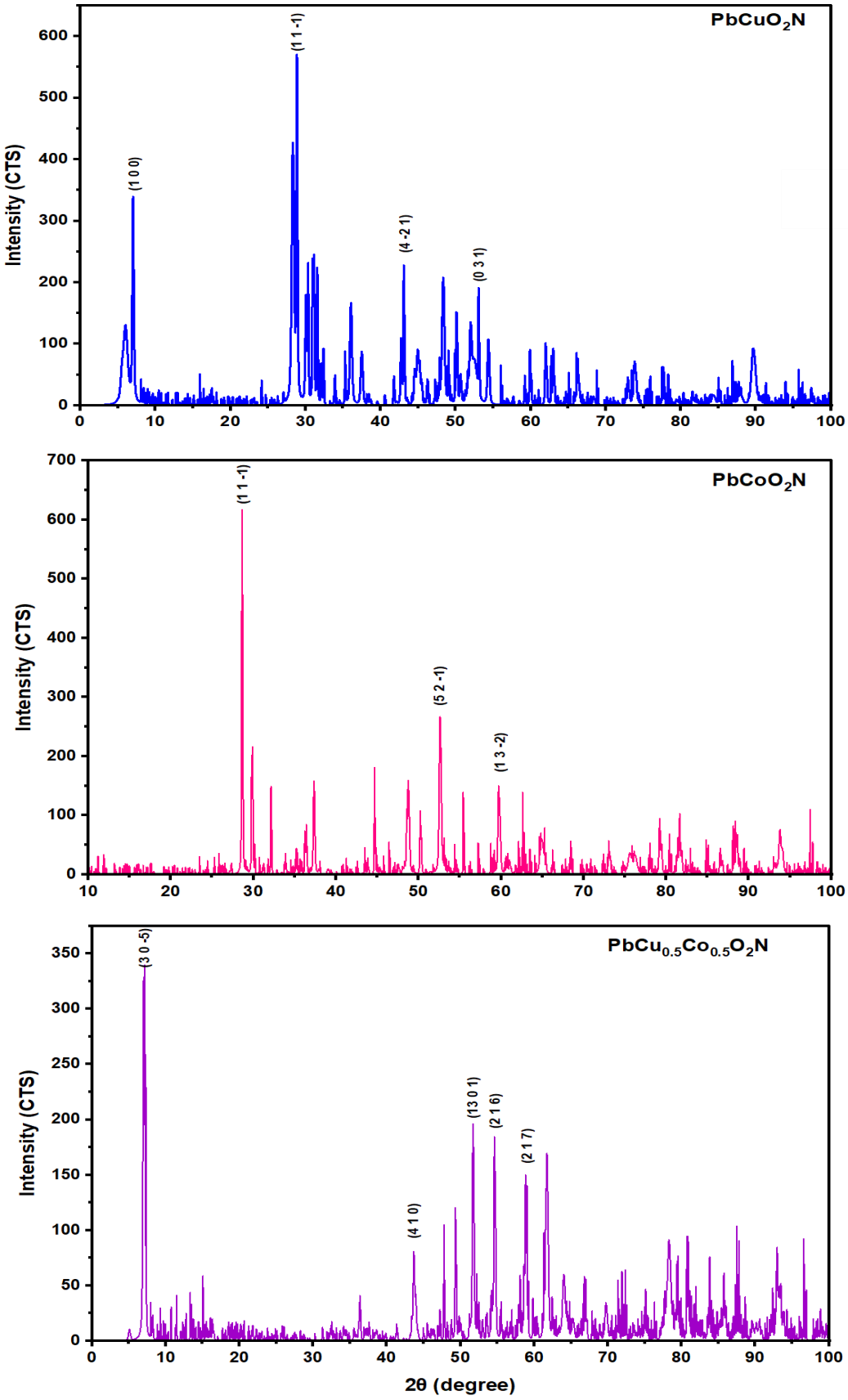


Fig. (3-7): X-ray diffraction patterns of the synthesized Pb-Based oxynitride via Sol–Gel Auto-Combustion

Thus, the XRD results of the present Pb-based oxynitride nanoparticles indicate that Cu/Co substitution and their combination significantly affected the crystal-lattice arrangement. The most evident change occurred in $PbCu_{0.5}Co_{0.5}O_2N$, where the space group changed to P2/m, accompanied by a substantial increase in unit-cell volume and dislocation density.

Table (3-4): X-ray data of $PbCuO_2N$, $PbCoO_2N$, and $PbCu_{0.5}Co_{0.5}O_2N$ oxynitride perovskite synthesized via Sol-gel Auto-Combustion technique.

Parameters	**$PbCuO_2N$**		**$PbCoO_2N$**	**$PbCu_{0.5}Co_{0.5}O_2N$**
Dislocation density(nm^{-2})	4.37×10^{-5}		3.39×10^{-5}	1.30×10^{-4}
Crystallinity (%)	73.43%		88.81%	84.41%
Space group	P1		P1	P2/m
Cell Parameters	**α**	95.03	102.58	90
	β	94.63	92.69	95.56
	Ɣ	99.14	79.27	90
	a(Å)	12.81	12.8	24.46
	b(Å)	7.66	5.69	2.20
	c(Å)	3.12	3.19	15.43
Cell volume ($Å^3$)	299.95		223.50	830.70
No. Unit cell	6.04×10^6		1.19×10^7	4.26×10^5
Density ($g.cm^{-3}$)	5.26		4.63	4.39

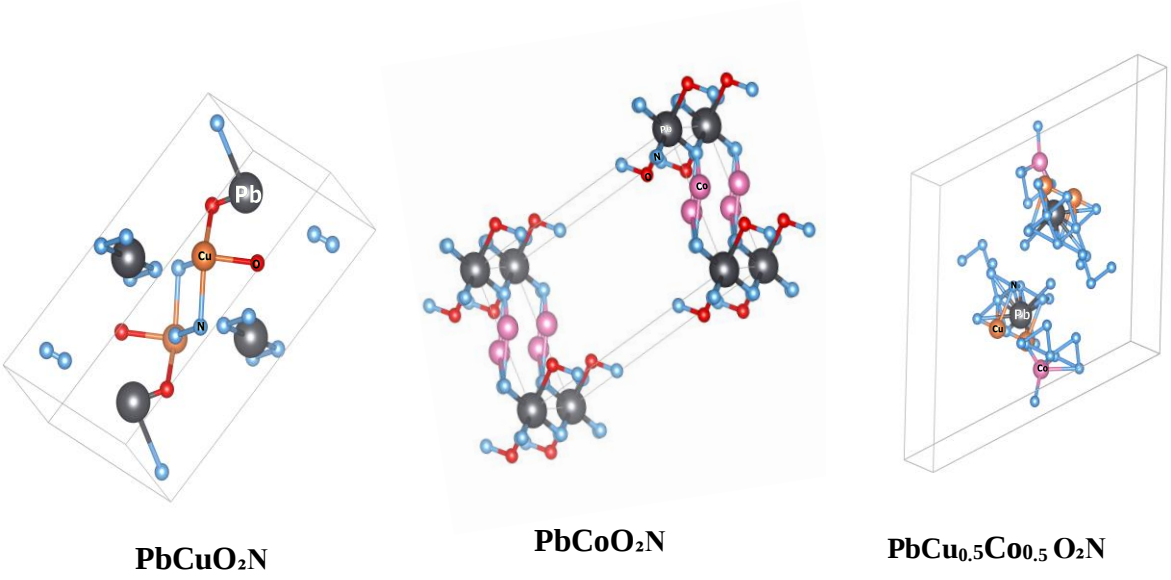


Fig. (3-8): X-ray crystal structures of synthesized Pb-Based oxynitride perovskite via Sol–Gel Auto-Combustion technique.

3.2 Morphological and Elemental Characterization

3.2.1 FESEM-EDS of Ba-based Oxynitride Perovskites

The FESEM images of $BaCuO_2N$, $BaCoO_2N$, and $BaCu_{0.5}Co_{0.5}O_2N$ show agglomerated particles with irregular shapes and different surface morphologies. The measured particle sizes are within the nanometer range, approximately 35–67 nm. The observed agglomeration can be attributed to particle growth and aggregation during the thermal treatment of the synthesized nanoparticles [88]. The presence of particles in the nanometer range indicates that the synthesized materials possess nanoscale morphology.

In addition, interparticle pores and small voids can be observed within the agglomerated regions. These features can be related to the removal of volatile species and gases during the thermal treatment of the sol–gel-derived

precursor[89]. These porous architectures have been shown to be especially important for increasing the content of the active reaction sites which is useful for applications in energy, such as in photocatalysis or solar water splitting[90]. The observed porous morphology indicates the presence of void spaces between the aggregated particles.

The EDS spectra show the presence of Ba, Cu, Co, O, and N in the corresponding samples. For $BaCuO_2N$, the EDS spectrum shows Ba, Cu, O, and N signals, with an N content of 6.1 at.%. For $BaCoO_2N$, the spectrum shows Ba, Co, O, and N signals, with an N content of 8.4 at.%, indicating the presence of the expected constituent elements. For $BaCu_{0.5}Co_{0.5}O_2N$, the simultaneous detection of Cu (4.1 at.%) and Co (4.8 at.%) together with Ba, O, and N indicates the presence of both transition metals in the synthesized material. These elemental results support the compositional results obtained from the XRD analysis.

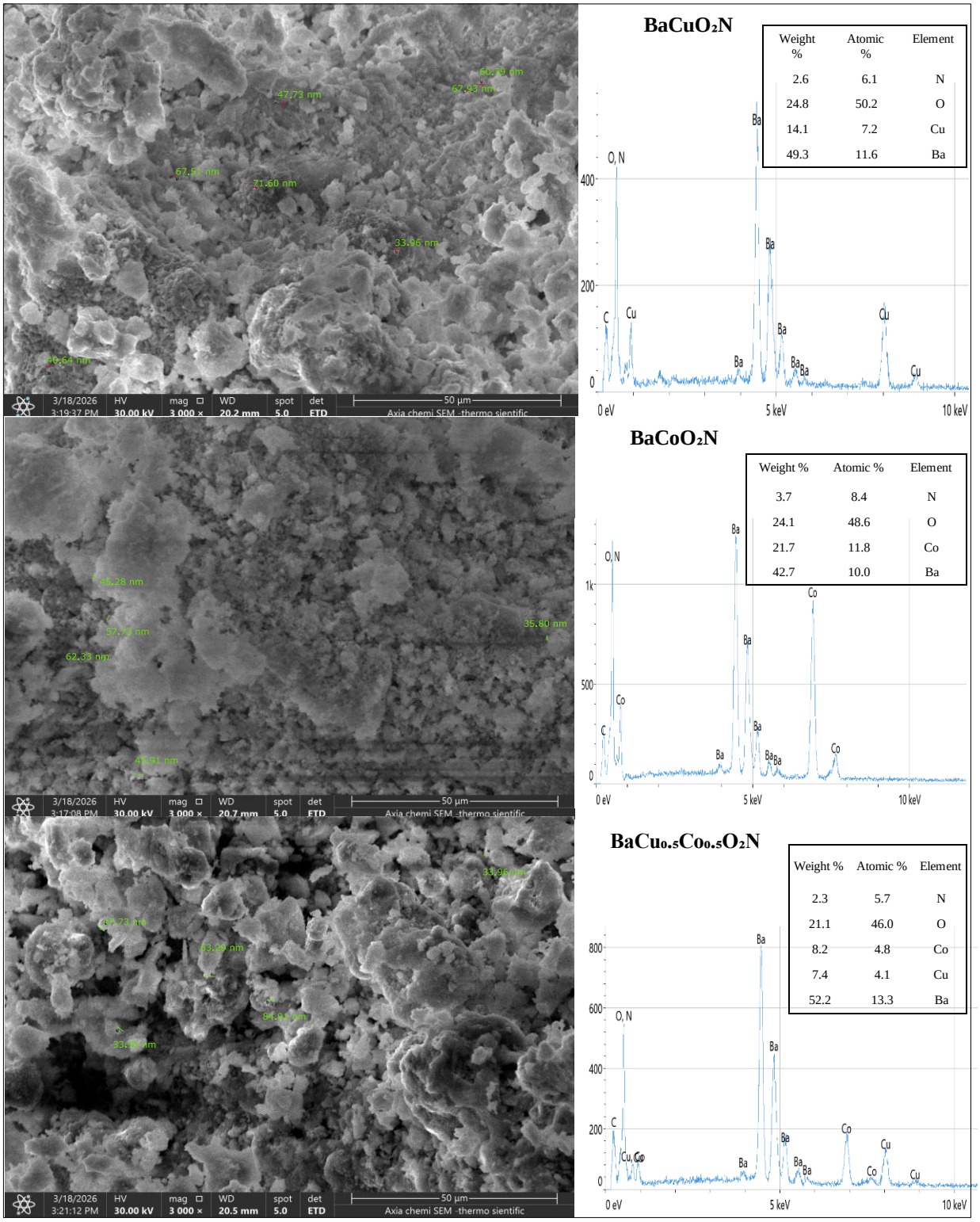


Fig. (3-9): FESEM micrographs of $BaCuO_2N$, $BaCoO_2N$, and $BaCu_{0.5}Co_{0.5}O_2N$ oxynitride perovskites synthesized by the sol–gel Auto-Combustion technique.

3.2.2 FESEM-EDS of Ca-Based Oxynitride Perovskites

The FESEM images were used to examine the morphological features, including the shape, distribution, and size of the particles, of $CaCuO_2N$, $CaCoO_2N$, and $CaCu_{0.5}Co_{0.5}O_2N$. Fig. (3-10) shows the morphology of $CaCuO_2N$, where the particles exhibit irregular to nearly spherical shapes with an agglomerated morphology. The measured particle sizes are within the nanometer range of approximately 38–96 nm. The observed agglomeration can be attributed to particle growth and aggregation during the thermal treatment of the synthesized nanoparticles[91]. The particles are relatively closely distributed throughout the observed area.

$CaCoO_2N$ exhibits a different surface morphology, characterized by plate-like particles with irregular multi-edged features. The particles form interconnected agglomerated regions with visible interparticle voids. The measured particle dimensions are within the nanometer range, approximately 32–85 nm. The observed morphological difference compared with $CaCuO_2N$ indicates a change in particle growth and surface arrangement with the change in transition-metal composition.

The $CaCu_{0.5}Co_{0.5}O_2N$ sample also exhibits irregular and agglomerated nanoparticles, with particle sizes approximately in the range of 43–83 nm. Interparticle voids can be observed between the aggregated particles. The differences in particle morphology and arrangement among the three oxynitrides indicate variations in their microstructural features.

The EDS analysis confirmed the presence of the expected constituent elements in the Ca-based oxynitride samples. The mixed $CaCu_{0.5}Co_{0.5}O_2N$ sample showed the simultaneous presence of Cu and Co, consistent with its mixed transition-metal composition. The nitrogen contents were 3.7 at.% for $CaCuO_2N$,

5.1 at.% for $CaCoO_2N$, and 3.7 at.% for $CaCu_{0.5}Co_{0.5}O_2N$. These results support the elemental composition of the synthesized Ca-based oxynitride samples.

The FESEM results show that $CaCuO_2N$ consists of agglomerated nanoparticles, $CaCoO_2N$ exhibits a plate-like particle morphology, while $CaCu_{0.5}Co_{0.5}O_2N$ shows irregular agglomerated nanoparticles. The differences in morphology and particle arrangement demonstrate variations in the microstructure of the Ca-based oxynitrides.

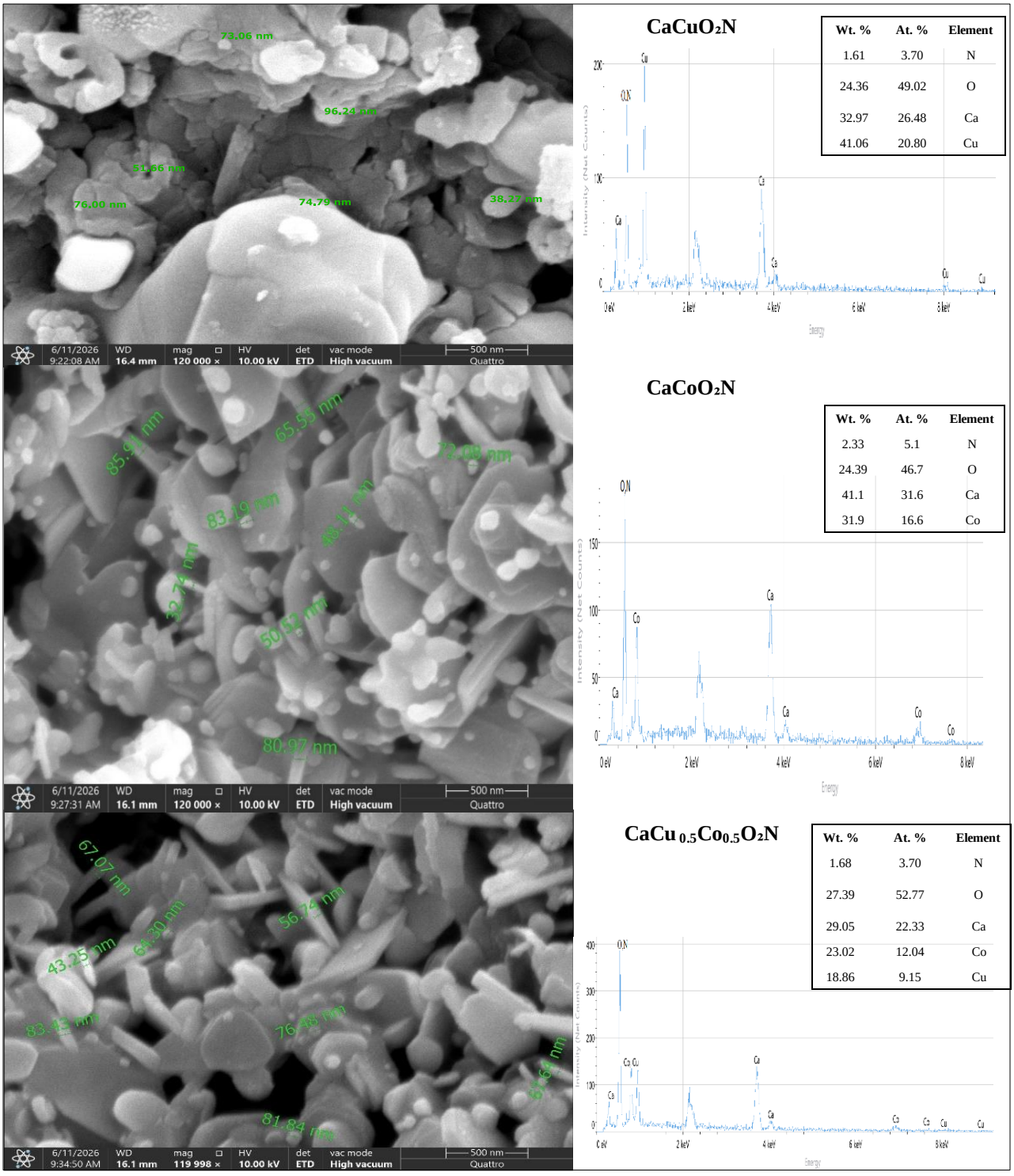


Fig. (3-10): FESEM micrographs of $CaCuO_2N$, $CaCoO_2N$, and $CaCu_{0.5}Co_{0.5}O_2N$ oxynitride perovskite synthesized by the sol–gel Auto-Combustion technique.

3.2.3 FESEM-EDS of Mg-Based Oxynitride Perovskites

The FESEM images were used to examine the morphological features, including the shape, distribution, and size of the particles, of $MgCuO_2N$, $MgCoO_2N$, and $MgCu_{0.5}Co_{0.5}O_2N$. Fig. (3-11) shows the morphology of $MgCuO_2N$, where the particles exhibit irregular shapes with an agglomerated morphology. The measured particle sizes are within the nanometer range, approximately 59–78 nm. The observed agglomeration can be attributed to particle growth and aggregation during the thermal treatment of the synthesized nanoparticles[92]. The particles are distributed throughout the observed area with visible interparticle voids. $MgCoO_2N$ exhibits a different particle morphology, with irregular to nearly rounded particles forming relatively dense agglomerated regions. The measured particle sizes are approximately 50–126 nm. The presence of different particle sizes and interparticle spaces indicates variations in particle growth and aggregation compared with $MgCuO_2N$.

The $MgCu_{0.5}Co_{0.5}O_2N$ sample shows irregular particles with a strongly agglomerated morphology. The measured particle sizes are approximately 75–149 nm, which are generally larger than those observed for $MgCuO_2N$ and within a higher size range than $MgCoO_2N$. The observed differences in particle size and morphology among the three oxynitrides indicate variations in the microstructural features of the Mg-based oxynitrides. The EDS spectra confirm the presence of the constituent elements in the Mg-based oxynitride samples. The nitrogen contents were 0.8 at.% for $MgCuO_2N$, 1.0 at.% for $MgCoO_2N$, and 2.3 at.% for $MgCu_{0.5}Co_{0.5}O_2N$. For the mixed composition, the Cu and Co contents were 13.3 and 12.8 at.%, respectively, indicating the simultaneous presence of both transition metals. These EDS results support the elemental composition of the synthesized Mg-based oxynitride samples.

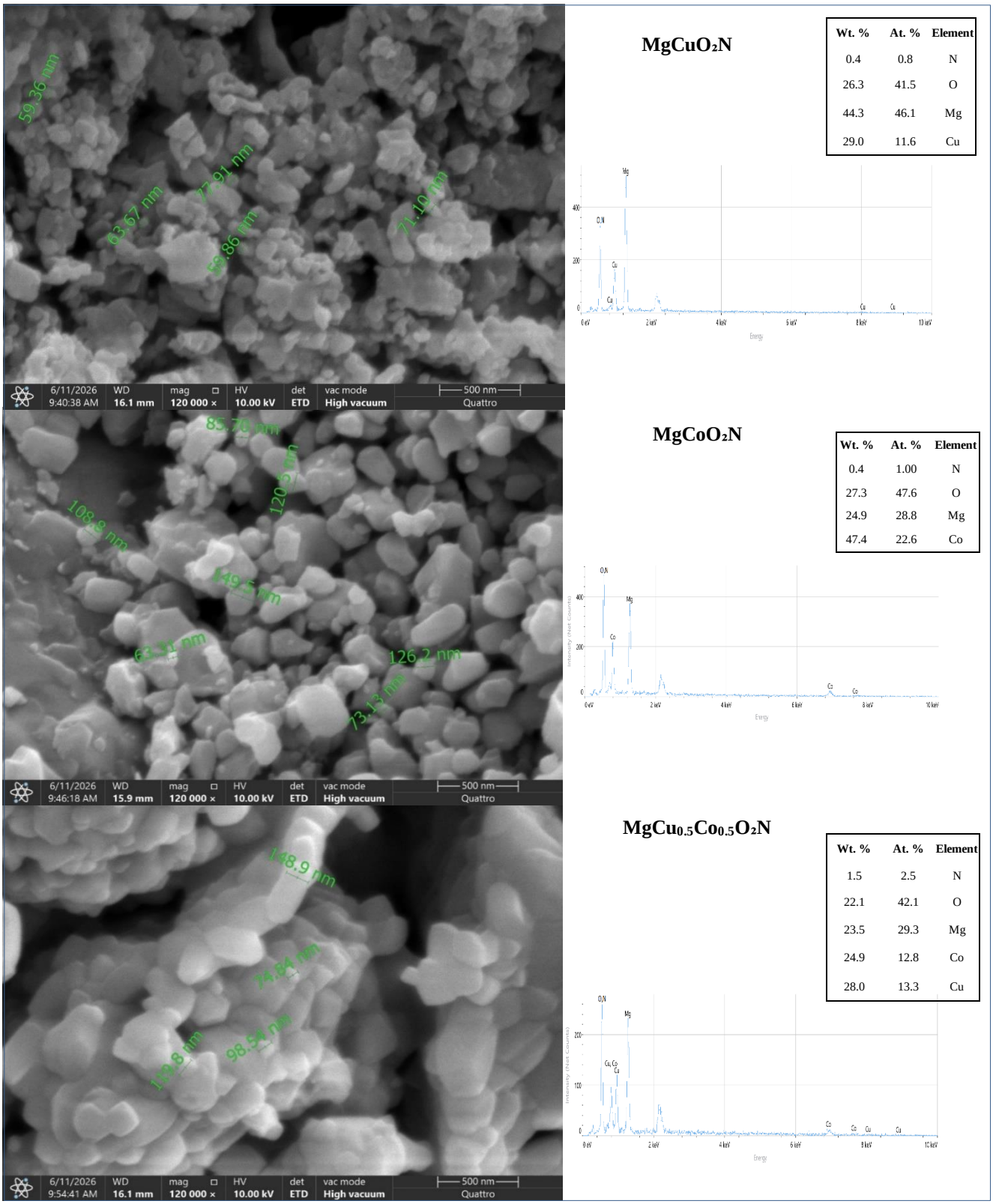


Fig. (3-11): FESEM micrographs of $MgCuO_2N$, $MgCoO_2N$, and $MgCu_{0.5}Co_{0.5}O_2N$ oxynitride perovskites synthesized by the sol–gel Auto-Combustion technique.

3.2.4 FESEM-EDS of Pb-Based Oxynitride Perovskites

The FESEM images were used to examine the morphological features, including the shape, distribution, and size of the particles, of $PbCuO_2N$, $PbCoO_2N$, and $PbCu_{0.5}Co_{0.5}O_2N$. Fig. (3-12) shows the morphology of $PbCuO_2N$, where the particles exhibit an agglomerated morphology with irregular shapes and visible voids between the aggregated regions. The measured particle sizes are within the nanometer range, approximately 80.72–94.67 nm. The observed agglomeration can be associated with particle growth and aggregation during the thermal treatment of the synthesized nanoparticles[93].

$PbCoO_2N$ exhibits a different surface morphology, characterized by irregular to nearly rounded particles with a relatively compact agglomerated arrangement. The measured particle sizes are approximately 53.30–89.54 nm. The particles show different sizes and shapes within the observed area, indicating variations in particle growth and arrangement compared with $PbCuO_2N$.

The $PbCu_{0.5}Co_{0.5}O_2N$ nanoparticles exhibits irregular particles with a pronounced agglomerated morphology. The measured particle sizes range approximately from 54.42 to 150.9 nm. The particles appear relatively larger in some regions, with visible spaces between the aggregated particles. The wider particle-size range observed for the mixed composition indicates a variation in particle growth and aggregation compared with the single-transition-metal nanomaterials

The EDS spectra confirm the presence of the constituent elements in the Pb-based oxynitride samples. The nitrogen contents were 3.0 at.% for $PbCuO_2N$, 1.5 at.% for $PbCoO_2N$, and 0.8 at.% for $PbCu_{0.5}Co_{0.5}O_2N$. For the mixed composition, the Cu and Co contents were 14.9 and 13.4 at.%, respectively, indicating the simultaneous presence of both transition metals. These EDS results

support the elemental composition of the synthesized Pb-based oxynitride samples.

The FESEM results show that $PbCuO_2N$ consists of irregular agglomerated nanoparticles with particle sizes of approximately 80.72–94.67 nm, $PbCoO_2N$ exhibits irregular to nearly rounded agglomerated particles with sizes of approximately 53.30–89.54 nm, while $PbCu_{0.5}Co_{0.5}O_2N$ shows irregular agglomerated particles with a wider size range of approximately 54.42–150.9 nm. The differences in particle morphology, size, and arrangement demonstrate variations in the microstructure of the Pb-based oxynitrides

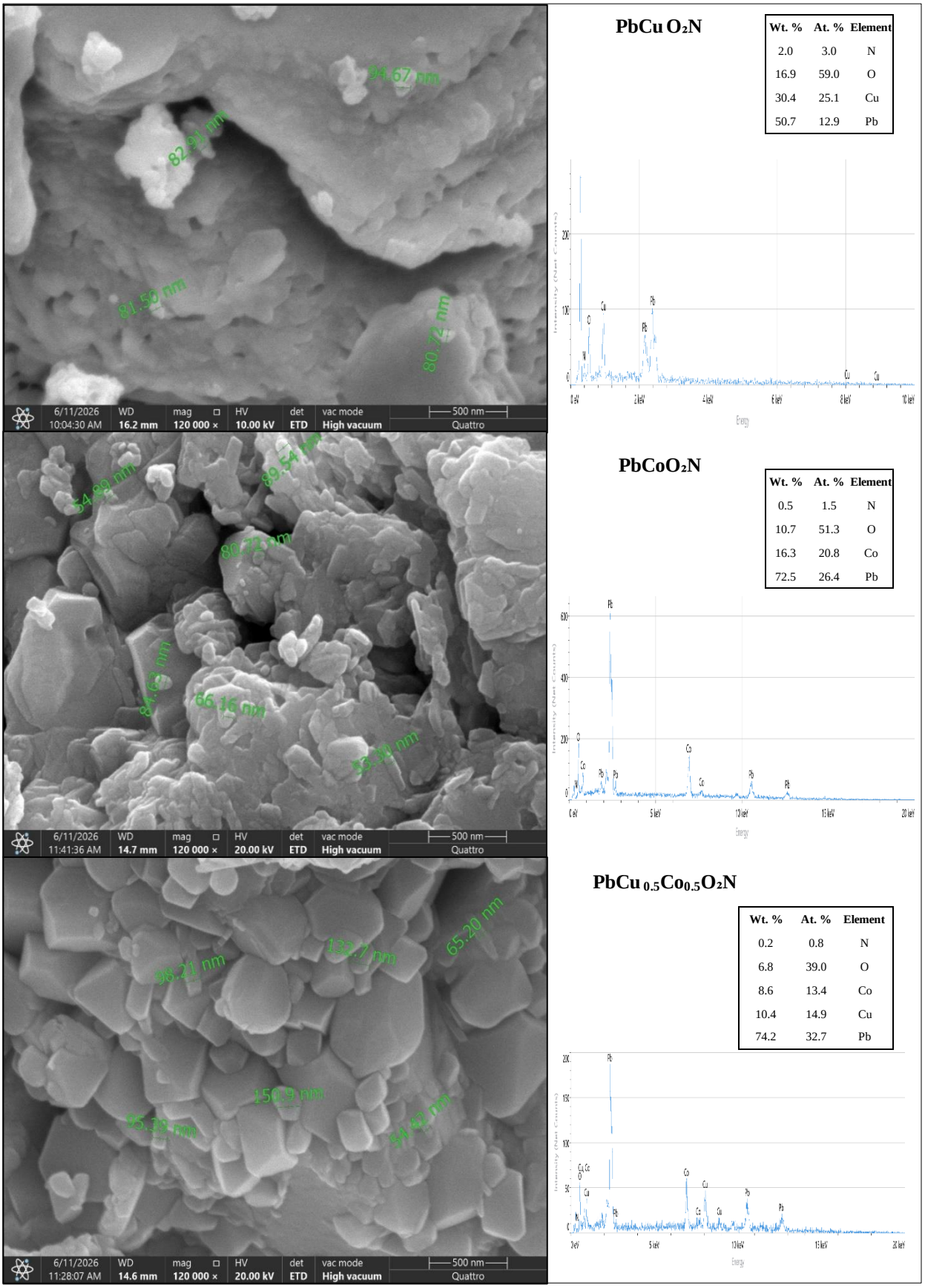


Fig. (3-12): FESEM micrographs of $PbCuO_2N$, $PbCoO_2N$, and $PbCu_{0.5}Co_{0.5}O_2N$ oxynitride perovskite synthesized by the sol–gel Auto-Combustion technique.

3.3 Atomic force Microscope Analysis (AFM)

3.3.1 Ba-Based Oxynitride Perovskites

The two-dimensional (2D) deflection maps and three-dimensional (3D) surface profiles obtained over a scanning area of 2.5 × 2.5 μm² reveal clear differences in the surface topography of the Ba-based oxynitride nanoparticles. The $BaCuO_2N$ sample exhibits an irregular surface with noticeable height variations and sharp nanoscale features. The 3D profile shows pronounced surface peaks and valleys, indicating variations in the surface topography of the nanomaterial. The corresponding roughness parameters were Sa = 0.303 nm, Sq = 0.755 nm, and Sy = 37.073 nm.

$BaCoO_2N$ exhibits a relatively uniform and densely packed surface morphology in the AFM images, with smaller apparent height variations across the scanned area. Its roughness parameters were Sa = 0.405 nm and Sq = 1.042 nm, while Sy was 35.252 nm. Although the 3D profile appears relatively uniform, the slightly higher Sa and Sq values compared with $BaCuO_2N$ indicate that its average surface roughness is somewhat greater. However, its lower Sy value indicates a smaller overall peak-to-valley height range within the scanned area[94].

The $BaCu_{0.5}Co_{0.5}O_2N$ sample shows a markedly different surface topography, characterized by more pronounced nanoscale features and larger height variations. The 3D profile displays pronounced surface features with prominent peaks and valleys. This observation is supported by the substantially higher roughness parameters, with Sa = 1.451 nm, Sq = 4.706 nm, and Sy = 55.102 nm. These values are considerably higher than those of both $BaCuO_2N$ and $BaCoO_2N$, indicating that the mixed Cu–Co oxynitride nanoparticles possess the roughest surface among the investigated Ba-based nanomaterials.

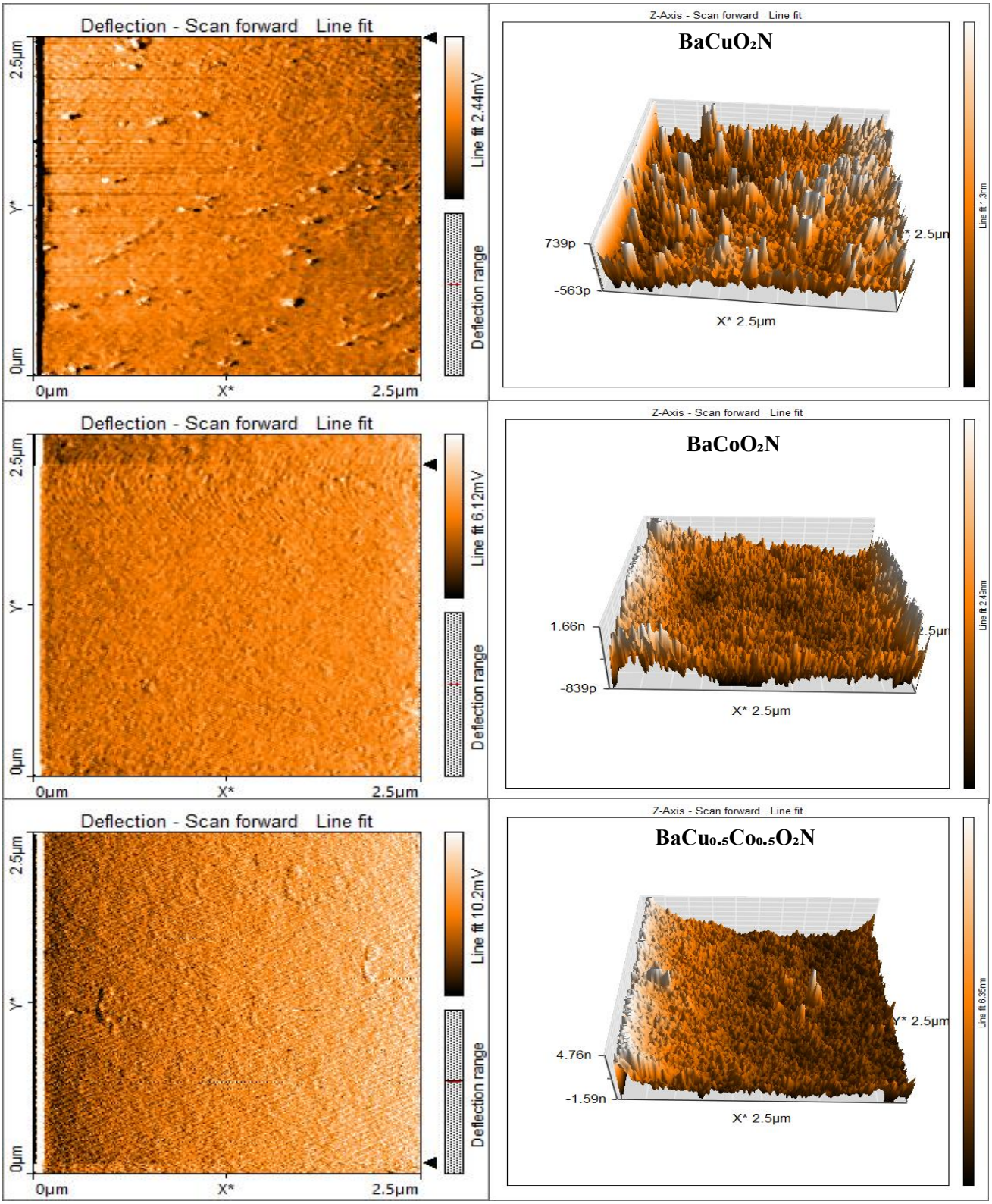


Fig. (3-13): AFM images of $BaCuO_2N$, $BaCoO_2N$ and $BaCu_{0.5}Co_{0.5}O_2N$ oxynitride perovskites synthesized sol–gel Auto-Combustion technique.

The differences in surface roughness demonstrate that changing the transition-metal composition affects the surface topography of the Ba-based oxynitride nanoparticles. Among the three samples, $BaCuO_2N$ exhibits the lowest Sa and Sq values and therefore has the smoothest average surface, whereas $BaCu_{0.5}Co_{0.5}O_2N$ exhibits the highest values of all three roughness parameters and consequently the greatest surface roughness. $BaCoO_2N$ shows an intermediate average roughness based on Sa and Sq, while its Sy value is the lowest among the three samples.

Based on the AFM results, $BaCuO_2N$ exhibited the smoothest surface among the investigated Ba-based oxynitride nanoparticles, as indicated by its lowest Sa and Sq values. In contrast, the higher roughness of $BaCu_{0.5}Co_{0.5}O_2N$ indicates a more heterogeneous surface topography with greater nanoscale height variations. The AFM results therefore demonstrate that the incorporation of both Cu and Co produces a substantial change in the surface morphology and roughness of the Ba-based oxynitride nanomaterials.

Table (3-5): AFM data of $BaCuO_2N$, $BaCoO_2N$ and $BaCu_{0.5}Co_{0.5}O_2N$ oxynitride perovskites synthesized by the sol–gel Auto-Combustion technique.

Perovskites oxynitride	**Sa (nm)**	**Sq (nm)**	**Sy (nm)**
$BaCuO_2N$	0.303	0.755	37.073
$BaCoO_2N$	0.405	1.042	35.252
$BaCu_{0.5}Co_{0.5}O_2N$	1.451	4.706	55.102

3.3.2 Ca-Based Oxynitride Perovskites

The atomic force microscopy (AFM) analysis of the synthesized $CaCuO_2N$, $CaCoO_2N$, and $CaCu_{0.5}Co_{0.5}O_2N$ oxynitride nanoparticles reveals clear differences in their surface topography and roughness. $CaCuO_2N$ exhibits an irregular surface morphology with noticeable height variations and agglomerated surface features. The corresponding roughness parameters were Sa = 36.20 nm, Sq = 46.24 nm, and Sy = 413.7 nm, indicating a relatively rough surface with a large peak-to-valley height range.

$CaCoO_2N$ also shows a rough and irregular surface morphology, with pronounced surface features and height variations across the scanned area. Its roughness parameters were Sa = 36.95 nm, Sq = 49.35 nm, and Sy = 326.3 nm. Compared with $CaCuO_2N$, $CaCoO_2N$ exhibits slightly higher Sa and Sq values, indicating a slightly greater average surface roughness, whereas its Sy value is lower, indicating a smaller overall peak-to-valley height range. The Sa parameter represents the arithmetic mean height deviation over the measured area, while Sq represents the root-mean-square height deviation and is more sensitive to larger height variations[95].

In contrast, $CaCu_{0.5}Co_{0.5}O_2N$ exhibits a different surface topography, characterized by more closely distributed and relatively finer surface features across the scanned area. The roughness parameters were Sa = 25.09 nm, Sq = 32.47 nm, and Sy = 254.2 nm. All three roughness parameters are lower than those of $CaCuO_2N$ and $CaCoO_2N$, indicating a smoother surface with smaller average height variations and a lower peak-to-valley height range.

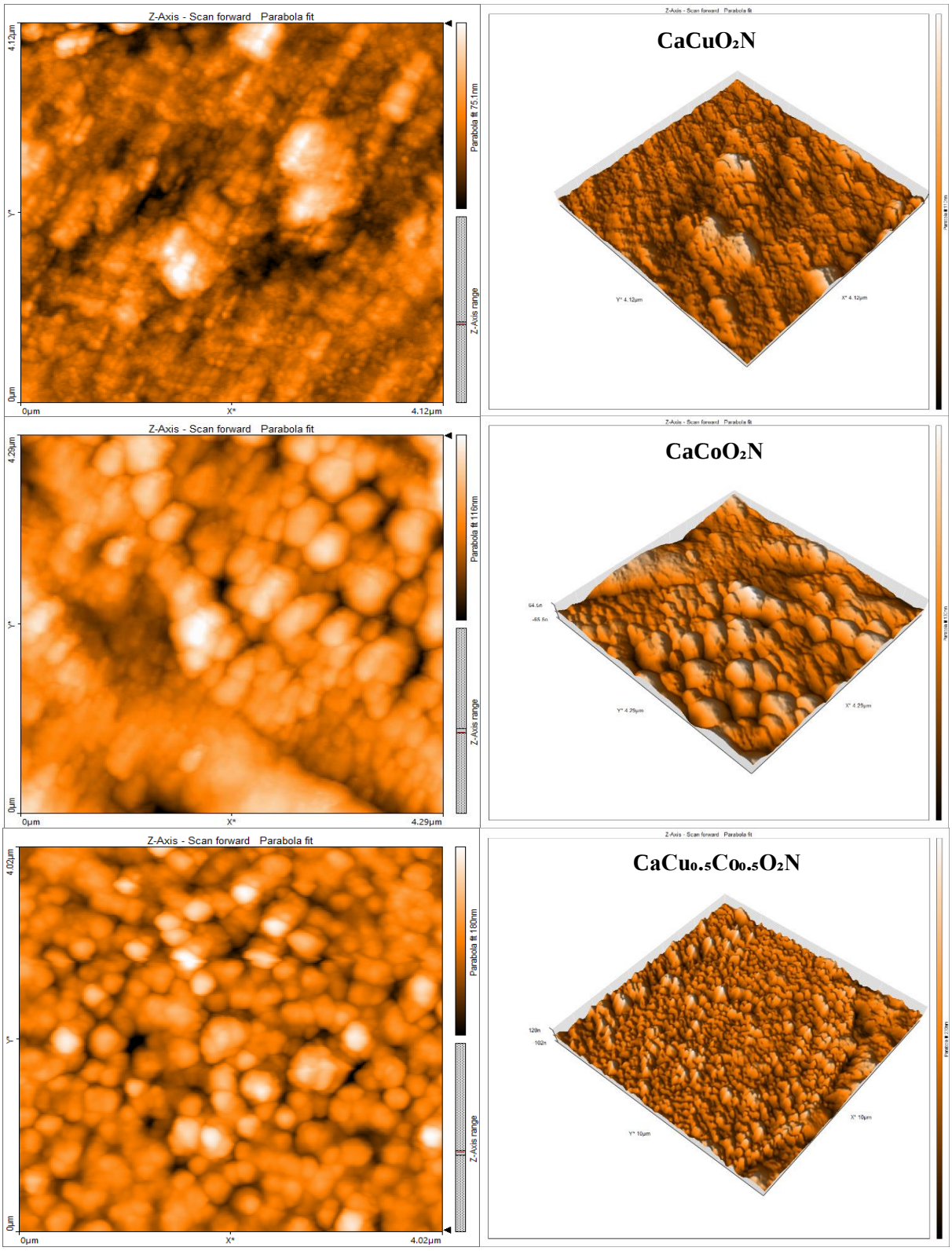


Fig. (3-14): AFM images of $CaCuO_2N$, $CaCoO_2N$ and $CaCu_{0.5}Co_{0.5}O_2N$ oxynitride perovskites synthesized sol–gel technique.

The differences in the AFM results indicate that changing the transition-metal composition at the B-site affects the surface topography of the Ca-based oxynitride nanoparticles. $CaCuO_2N$ and $CaCoO_2N$ exhibit comparatively higher surface roughness, whereas $CaCu_{0.5}Co_{0.5}O_2N$ exhibits the lowest values of Sa, Sq, and Sy among the investigated samples[96].

Based on the AFM results, $CaCu_{0.5}Co_{0.5}O_2N$ exhibited the smoothest surface among the investigated Ca-based oxynitride nanoparticles, as indicated by its lowest Sa and Sq values, together with the lowest Sy value. This indicates that the mixed Cu–Co sample has the smallest average surface roughness and the lowest overall peak-to-valley height variation within the scanned area.

Table (3-6): AFM data of $CaCuO_2N$, $CaCoO_2N$ and $CaCu_{0.5}Co_{0.5}O_2N$ oxynitride perovskites synthesized by the sol–gel Auto-Combustion technique.

Perovskites oxynitride	Sa (nm)	Sq (nm)	Sy (nm)
$CaCuO_2N$	36.20	46.24	413.7
$CaCoO_2N$	36.95	49.35	326.3
$CaCu_{0.5}Co_{0.5}O_2N$	25.09	32.47	254.2

3.3.3 Mg-Based Oxynitride Perovskites

AFM analysis of the synthesized $MgCuO_2N$, $MgCoO_2N$, and $MgCu_{0.5}Co_{0.5}O_2N$ oxynitride nanoparticles reveals clear differences in their surface topography and roughness with changes in the transition-metal composition. $MgCuO_2N$ exhibits an irregular surface morphology with relatively small height variations and comparatively fine surface features across the scanned area. The corresponding roughness parameters were Sa = 17.79 nm, Sq = 23.17 nm, and Sy = 199.7 nm, indicating the lowest surface roughness among the investigated Mg-based samples.

$MgCoO_2N$ exhibits a more pronounced surface topography, with larger surface features and greater height variations across the scanned area. Its roughness parameters were Sa = 28.60 nm, Sq = 36.09 nm, and Sy = 287.2 nm. Compared with $MgCuO_2N$, the higher Sa and Sq values indicate greater average surface roughness, while the higher Sy value indicates a larger overall peak-to-valley height range. AFM measurements provide quantitative information on surface height variations and are therefore suitable for comparing the surface roughness of different nanomaterials.

The $MgCu_{0.5}Co_{0.5}O_2N$ sample shows the most pronounced surface topography among the three samples, with more prominent surface features and greater height variations in the AFM images. The corresponding roughness parameters were Sa = 41.63 nm, Sq = 54.15 nm, and Sy = 543.7 nm. These values are higher than those of both $MgCuO_2N$ and $MgCoO_2N$, indicating that the mixed Cu–Co oxynitride nanoparticles possess the highest surface roughness and the largest peak-to-valley height range among the investigated Mg-based samples.

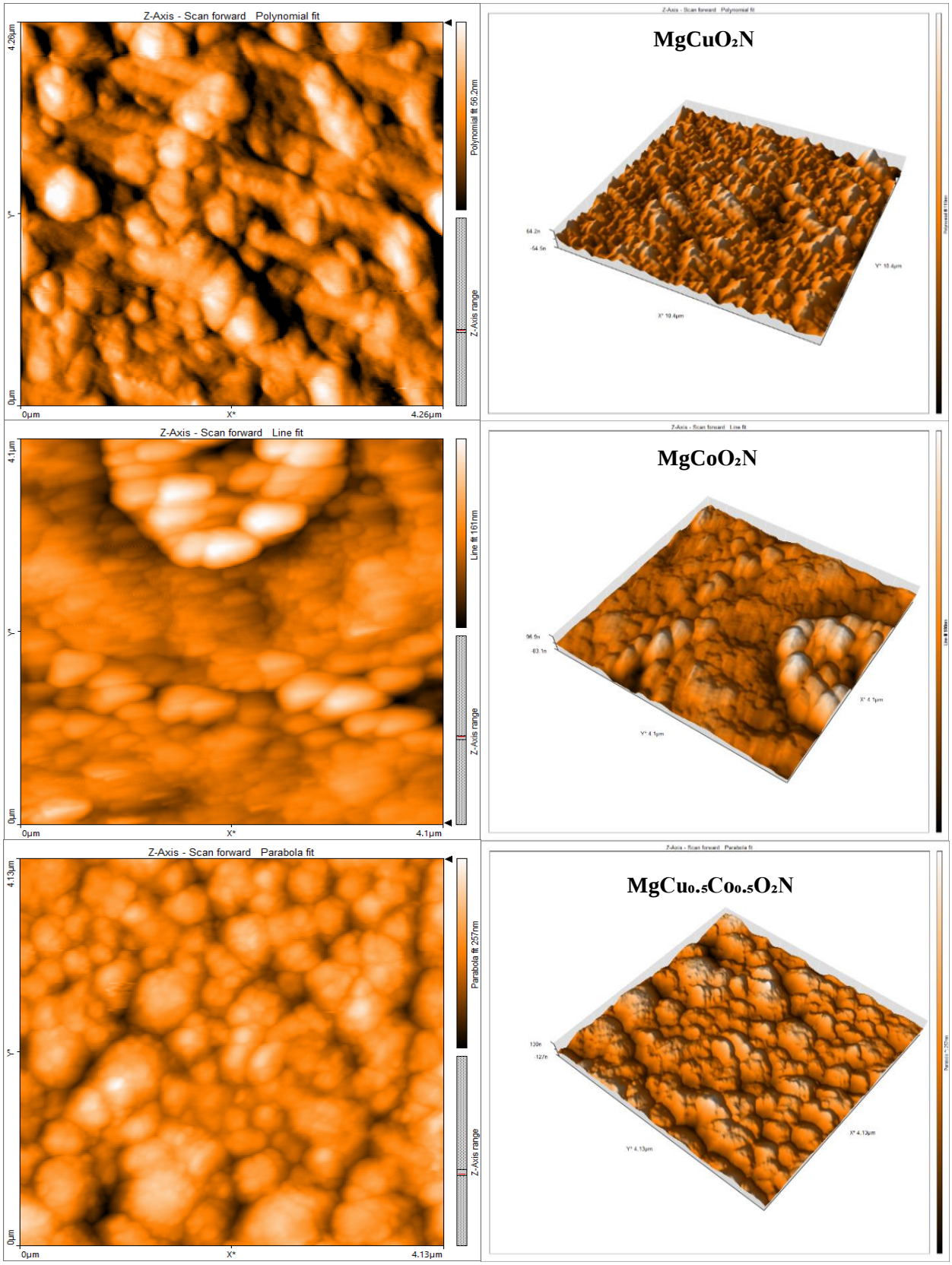


Fig. (3-15): AFM images of $MgCuO_2N$, $MgCoO_2N$ and $MgCu_{0.5}Co_{0.5}O_2N$ oxynitride perovskites synthesized by the sol–gel Auto-Combustion technique.

The differences in surface roughness indicate that changing the transition-metal composition affects the surface topography of the Mg-based oxynitride nanoparticles. The progressive increase in Sa, Sq, and Sy from $MgCuO_2N$ to $MgCoO_2N$ and $MgCu_{0.5}Co_{0.5}O_2N$ demonstrates an increase in the magnitude of surface height variations across the measured areas. Such differences in morphology can be associated with changes occurring during the preparation and thermal treatment of sol–gel-derived nanoparticles, since drying and calcination can influence particle growth, coarsening, and aggregation[97].

Among the investigated samples, $MgCuO_2N$ exhibited the smoothest surface, as indicated by its lowest Sa, Sq, and Sy values. In contrast, $MgCu_{0.5}Co_{0.5}O_2N$ exhibited the roughest surface, with the highest values of all three roughness parameters. $MgCoO_2N$ showed an intermediate surface roughness between the two samples based on Sa, Sq, and Sy.

The AFM results demonstrate that the transition-metal composition has a clear effect on the nanoscale surface morphology of the Mg-based oxynitride nanoparticles. $MgCuO_2N$ exhibited the most uniform surface in terms of the measured roughness parameters, whereas $MgCu_{0.5}Co_{0.5}O_2N$ showed the greatest surface height variations and roughness. These observations are consistent with the quantitative AFM data obtained from the scanned surfaces.

Table (3-7): AFM data of $MgCuO_2N$, $MgCoO_2N$ and $MgCu_{0.5}Co_{0.5}O_2N$ oxynitride perovskites synthesized by the sol–gel Auto-Combustion technique.

Perovskites oxynitride	**Sa (nm)**	**Sq (nm)**	**Sy (nm)**
$MgCuO_2N$	17.79	23..17	199.7
$MgCoO_2N$	28.60	36.09	287.2
$MgCu_{0.5}Co_{0.5}O_2N$	41.63	54.15	543.7

3.3.4 Pb-Based Oxynitride Perovskites

AFM analysis of the synthesized $PbCuO_2N$, $PbCoO_2N$, and $PbCu_{0.5}Co_{0.5}O_2N$ oxynitride nanoparticles reveals clear differences in surface topography and roughness with changes in the transition-metal composition. $PbCuO_2N$ exhibits an irregular surface topography with noticeable height variations and several pronounced surface features, as observed in both the two-dimensional and three-dimensional AFM images. The corresponding roughness parameters were Sa = 40.40 nm, Sq = 51.20 nm, and Sy = 384.6 nm, indicating a relatively rough surface with a considerable peak-to-valley height range.

$PbCoO_2N$ exhibits a comparatively different surface topography, with more clearly defined rounded surface features distributed across the scanned area. The corresponding roughness parameters were Sa = 29.35 nm, Sq = 37.33 nm, and Sy = 310.4 nm. The lower Sa and Sq values compared with $PbCuO_2N$ indicate lower average surface roughness, while the lower Sy value indicates a smaller overall peak-to-valley height range.

In contrast, $PbCu_{0.5}Co_{0.5}O_2N$ exhibits the most pronounced surface height variations among the investigated Pb-based samples. The two-dimensional AFM image shows irregular surface features, while the three-dimensional profile displays a more strongly undulated surface with pronounced peaks and valleys. The measured roughness parameters were Sa = 50.91 nm, Sq = 64.34 nm, and Sy = 541.4 nm. These values are higher than those obtained for both $PbCuO_2N$ and $PbCoO_2N$, indicating that the mixed Cu–Co oxynitride nanoparticles possess the highest surface roughness and the largest peak-to-valley height range among the investigated Pb-based samples.

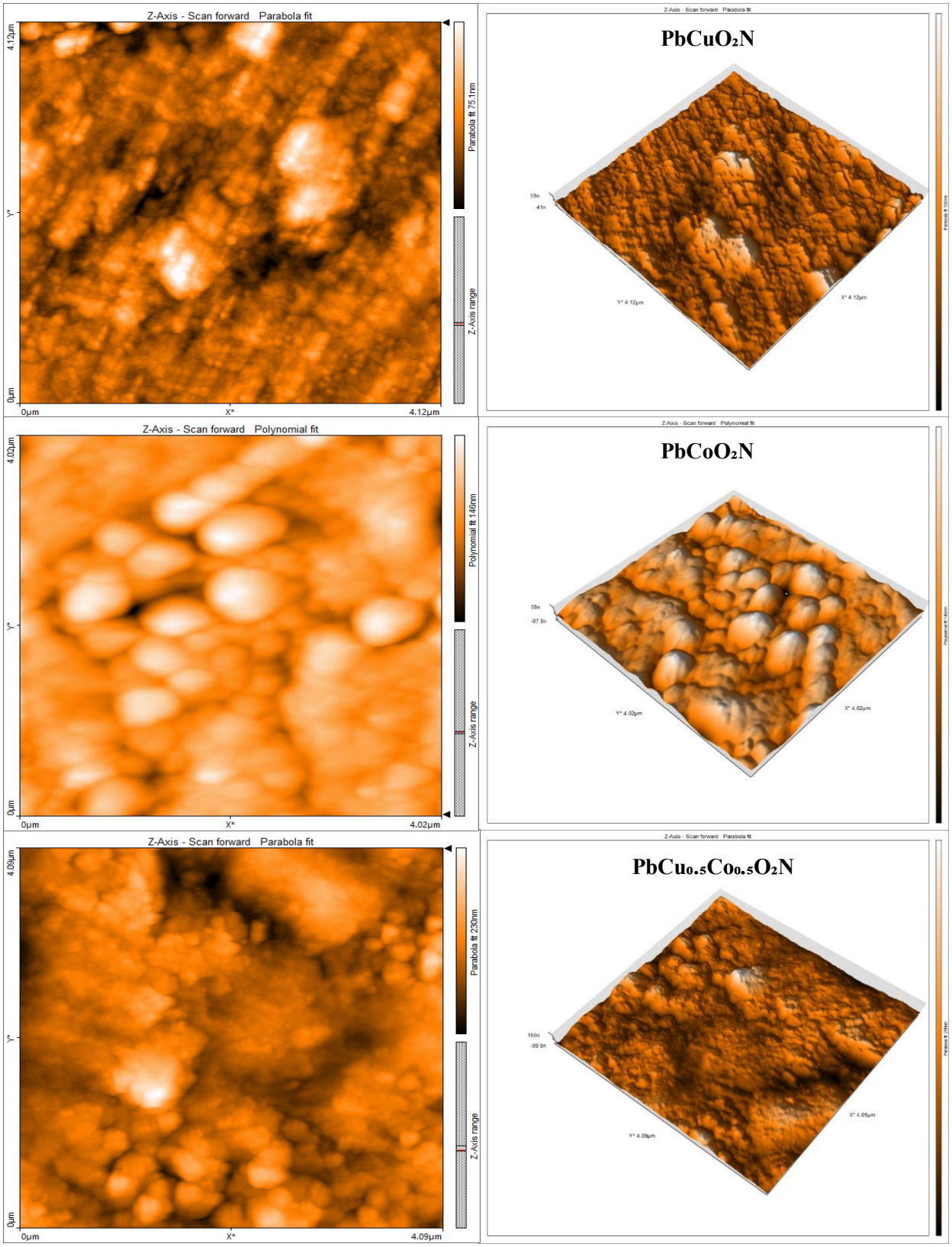


Fig. (3-16): AFM images of $PbCuO_2N$, $PbCoO_2N$ and $PbCu_{0.5}Co_{0.5}O_2N$ oxynitride perovskites synthesized by the sol–gel Auto-Combustion technique.

The differences in the AFM results demonstrate that changing the transition-metal composition affects the surface topography of the Pb-based oxynitride nanoparticles. The Sa and Sq values provide quantitative measures of the average and root-mean-square surface height variations, respectively, while the peak-to-valley parameter represents the overall height difference between the highest and lowest points within the analyzed surface area.

However, the specific mechanism responsible for the differences observed among the present Pb-based oxynitride samples cannot be established from the AFM measurements alone. Among the investigated Pb-based oxynitride nanoparticles, $PbCoO_2N$ exhibited the smoothest surface, as indicated by its lowest Sa, Sq, and Sy values.

$PbCuO_2N$ showed higher surface roughness, whereas $PbCu_{0.5}Co_{0.5}O_2N$ exhibited the highest values of all three roughness parameters and therefore the roughest surface. Thus, the AFM results demonstrate that the transition-metal composition has a measurable effect on the nanoscale surface morphology of the Pb-based oxynitride nanoparticles.

$PbCoO_2N$ exhibited the lowest average roughness and the smallest peak-to-valley height range, whereas $PbCu_{0.5}Co_{0.5}O_2N$ showed the greatest surface height variations and roughness. These conclusions are directly supported by the AFM images and the corresponding quantitative roughness parameters.

Table (3-8): AFM data of $PbCuO_2N$, $PbCoO_2N$ and $PbCu_{0.5}Co_{0.5}O_2N$ oxynitride perovskites synthesized by the sol–gel Auto-Combustion technique.

Perovskites oxynitride	**Sa (nm)**	**Sq (nm)**	**Sy (nm)**
$PbCuO_2N$	40.40	51.20	384.6
$PbCoO_2N$	29.35	37.33	310.4
$PbCu_{0.5}Co_{0.5}O_2N$	50.91	64.34	541.4

3.4 FTIR Spectroscopy Analysis

3.4.1 Ba-Based Oxynitride Perovskites

The FTIR spectra of $BaCuO_2N$, $BaCoO_2N$, and $BaCu_{0.5}Co_{0.5}O_2N$ synthesized by the sol–gel method are presented in Fig. (3-17). The spectra show several absorption bands at different wavenumbers, indicating the vibrational characteristics of the synthesized materials and changes in their local chemical environments. For $BaCuO_2N$, a broad absorption band is observed at 3443.19 cm^{-1}, which is attributed to the O–H stretching vibration associated with surface-adsorbed moisture. The corresponding band is also observed at 3443.46 cm^{-1} for $BaCu_{0.5}Co_{0.5}O_2N$. The presence of this band is related to the interaction of the sample surface with moisture from the surrounding atmosphere.

In the intermediate-wavenumber region, $BaCuO_2N$ exhibits absorption bands at 1443.86, 1187.89, 1059.02, and 858.61 cm^{-1}. $BaCoO_2N$ shows bands at 1715.10, 1432.67, 1059.31, and 887.93 cm^{-1}, while $BaCu_{0.5}Co_{0.5}O_2N$ exhibits bands at 1715.19, 1429.06, 1059.34, and 858.11 cm^{-1}. The similarity of several bands among the three samples indicates that they possess related chemical environments. The slight shifts in the band positions can be attributed to changes in the local bonding environment resulting from the different B-site cations. In perovskite oxynitrides, changes in the cationic and anionic environments can affect the vibrational frequencies of the structure[99].

The low-wavenumber region provides important information about the inorganic framework of the synthesized materials. For $BaCuO_2N$, the main absorption bands in this region are located at approximately 653.63 and 516.98 cm^{-1}. For $BaCoO_2N$, prominent bands are observed at approximately 688.42, 579.88, and 541.15 cm^{-1}. In $BaCu_{0.5}Co_{0.5}O_2N$, the main bands occur at approximately 660.70 and 581.99 cm^{-1}. These absorption bands can be assigned to vibrational modes of the metal–anion framework. Similar low-wavenumber

vibrational features have been reported for perovskite oxynitrides and are related to the vibrations of the metal–anion structural units[99].

A comparison of the three spectra shows that the position of the main framework-related bands changes with the B-site composition. The main band shifts from 653.63 cm^{-1} in $BaCuO_2N$ to 688.42 cm^{-1} in $BaCoO_2N$ and to 660.70 cm^{-1} in $BaCu_{0.5}Co_{0.5}O_2N$. Similarly, the band at 516.98 cm^{-1} in $BaCuO_2N$ occurs at higher wavenumbers in the Co-containing samples, reaching 581.99 cm^{-1} in $BaCu_{0.5}Co_{0.5}O_2N$. These changes indicate that the substitution of Cu by Co and the simultaneous presence of Cu and Co modify the local vibrational environment of the B-site.

The $BaCu_{0.5}Co_{0.5}O_2N$ sample therefore exhibits a distinct FTIR response compared with the single-metal compositions. The changes in the positions of the low-wavenumber bands indicate a modified local bonding environment resulting from the coexistence of Cu and Co at the B-site. This result is consistent with the effect of cation substitution on the local structural environment of perovskite-type oxynitrides. The FTIR spectra confirm the presence of characteristic vibrations of the inorganic framework in the three synthesized compounds.

The differences in the positions of the main absorption bands demonstrate that the nature of the B-site cation influences the local vibrational environment. Among the investigated samples, $BaCu_{0.5}Co_{0.5}O_2N$ shows the clearest change in the framework-related vibrational bands, indicating that the simultaneous incorporation of Cu and Co produces a different local chemical environment compared with the single-metal compositions. These FTIR results are consistent with the structural changes observed by the other characterization techniques.

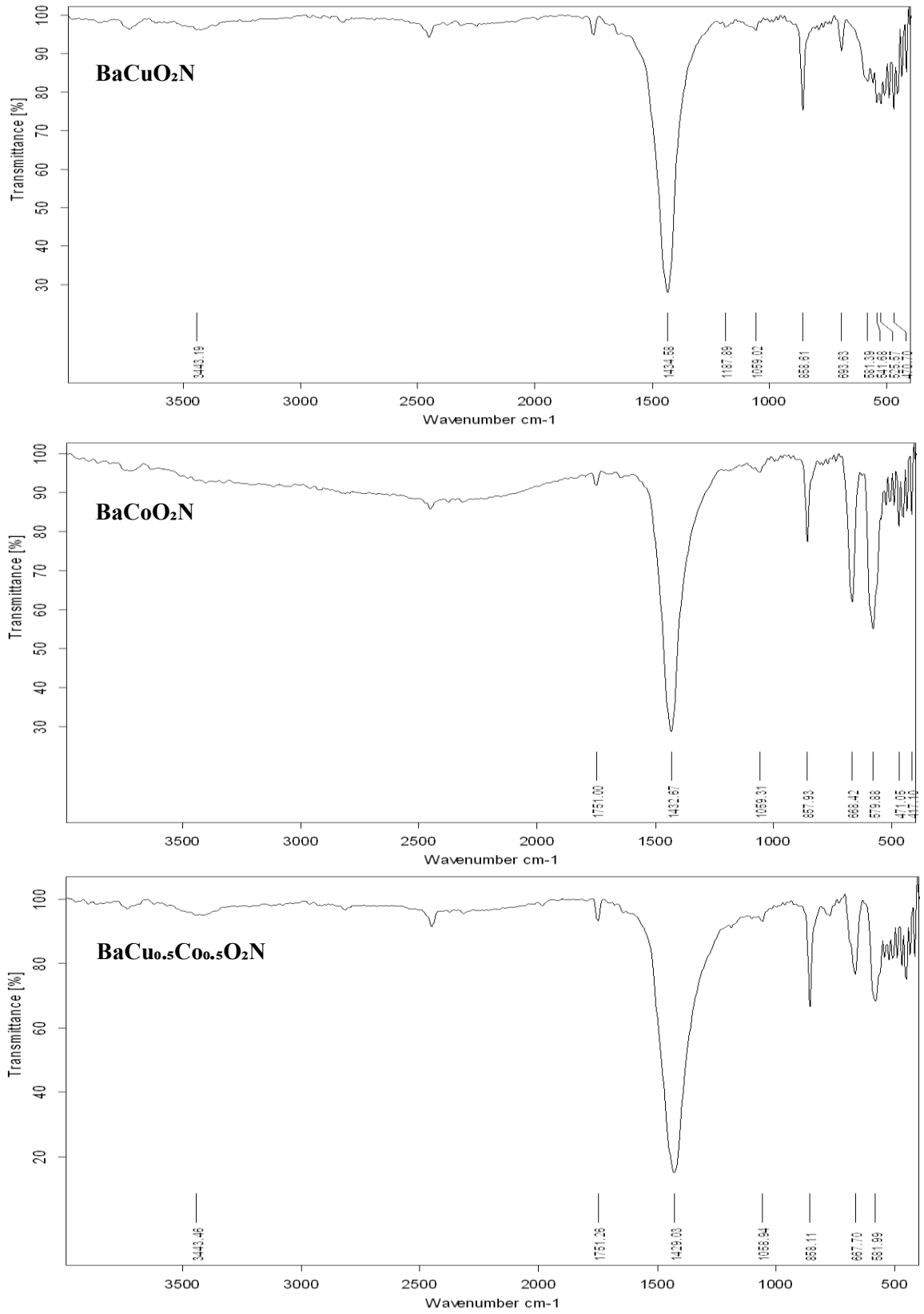


Fig. (3-17): FTIR Spectra of $BaCuO_2N$, $BaCoO_2N$ and $BaCu_{0.5}Co_{0.5}O_2N$ oxynitride perovskites synthesized by the sol–gel Auto-Combustion technique.

3.4.2 Ca-Based Oxynitride Perovskites

FTIR spectra of $CaCuO_2N$, $CaCoO_2N$, and $CaCu_{0.5}Co_{0.5}O_2N$ synthesized by the sol–gel method are shown in Fig. (3-18). The spectra exhibit different absorption features over the investigated wavenumber range, reflecting changes in the vibrational behavior of the prepared calcium-based oxynitride perovskites. The low-wavenumber region below 700 cm^{-1} is particularly important for identifying the vibrational characteristics of the inorganic framework.

$CaCuO_2N$ exhibits several absorption bands in this region, with distinct features extending from approximately 670 to 450 cm^{-1}. $CaCoO_2N$ also shows several absorption features within the same region, while $CaCu_{0.5}Co_{0.5}O_2N$ exhibits a series of overlapping absorption bands extending over approximately the same range. These low-wavenumber bands are associated with vibrational modes of the metal–anion framework of the perovskite structure. Similar low-wavenumber vibrational features have been reported for perovskite-related oxynitrides and have been associated with vibrations of the metal–anion structural units[100].

A comparison of the spectra reveals clear differences in the vibrational response of the three compositions. $CaCuO_2N$ shows relatively well-resolved absorption features in the low-wavenumber region, whereas $CaCoO_2N$ exhibits broader and less distinctly separated features. In $CaCu_{0.5}Co_{0.5}O_2N$, the low-wavenumber region contains several overlapping bands, producing a more complex vibrational profile. These differences are related to the change in the B-site composition from Cu to Co and to the simultaneous presence of Cu and Co in the mixed oxynitrides.

The changes observed in the positions and shapes of the low-wavenumber bands indicate that the substitution of Cu by Co modifies the local vibrational

environment of the inorganic framework. In the mixed $CaCu_{0.5}Co_{0.5}O_2N$ composition, the coexistence of Cu and Co at the B-site produces a vibrational response different from those of the individual $CaCuO_2N$ and $CaCoO_2N$ compositions. This behavior is consistent with the sensitivity of perovskite-related oxynitrides to changes in the local cationic and anionic environment

The FTIR results show that the three calcium-based oxynitride perovskites possess distinct vibrational characteristics that vary according to the B-site composition. The differences in the low-wavenumber absorption features demonstrate that the incorporation of Co and the simultaneous presence of Cu and Co modify the local vibrational environment of the perovskite framework. The FTIR results therefore support the formation of different local chemical environments in $CaCuO_2N$, $CaCoO_2N$, and $CaCu_{0.5}Co_{0.5}O_2N$.

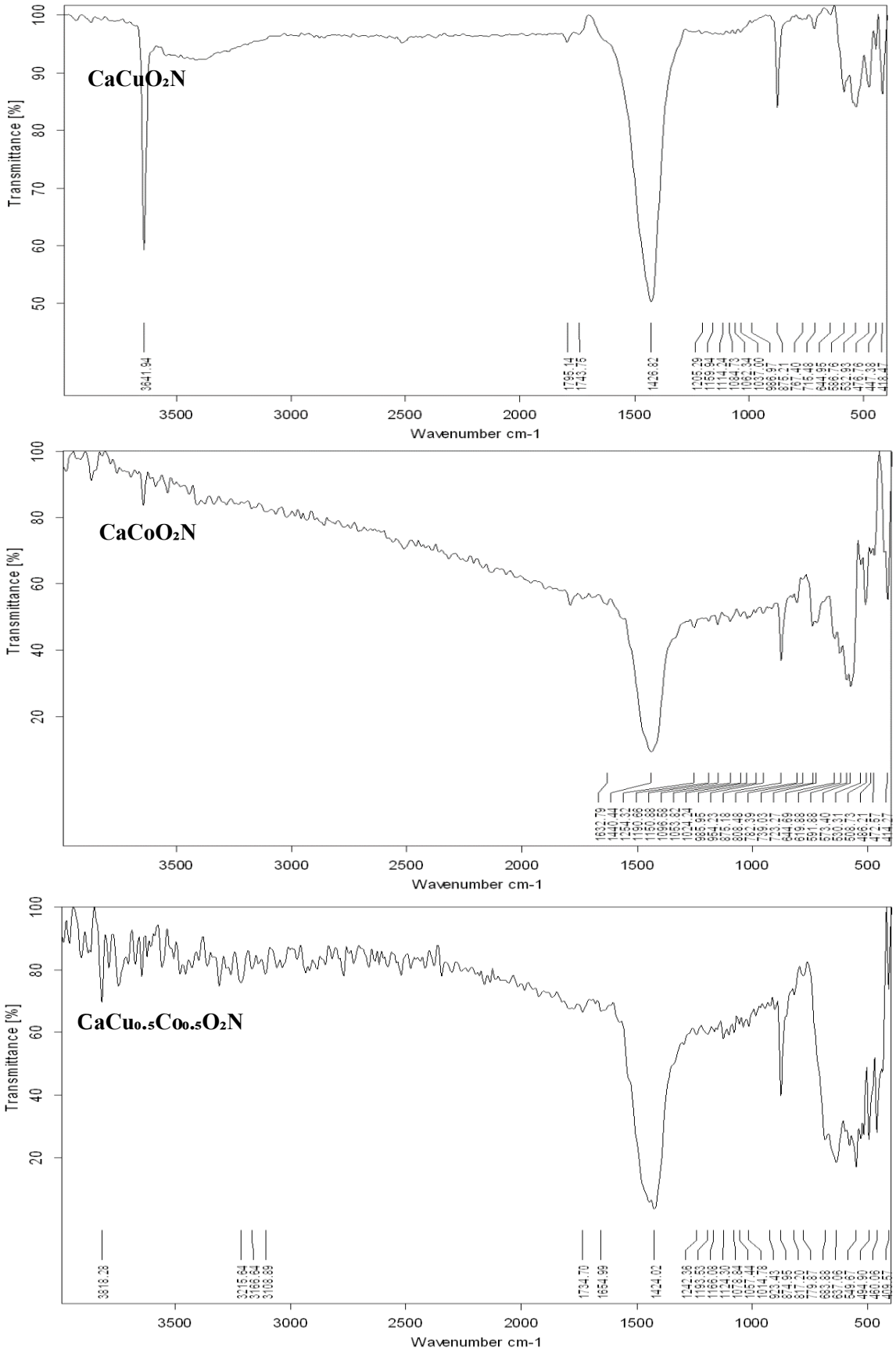


Fig. (3-18): FTIR images of $CaCuO_2N$, $CaCoO_2N$ and $CaCu_{0.5}Co_{0.5}O_2N$ oxynitride perovskites synthesized by the sol–gel Auto-Combustion technique.

3.4.3 Mg-Based Oxynitride Perovskites

The FTIR spectra of $MgCuO_2N$, $MgCoO_2N$, and $MgCu_{0.5}Co_{0.5}O_2N$ nanoparticles synthesized by the sol–gel method are presented in Fig. (3-19). The spectra exhibit composition-dependent absorption features, particularly in the mid- and low-wavenumber regions, reflecting differences in the vibrational response of the magnesium-based oxynitride nanomaterials.

$MgCuO_2N$ exhibits a broad absorption profile in the mid-wavenumber region, with distinguishable features at approximately 1465 and 1435 cm^{-1}. In contrast, $MgCoO_2N$ and $MgCu_{0.5}Co_{0.5}O_2N$ show a comparatively narrower absorption feature around 1405–1407 cm^{-1}. The change in the position and profile of these absorption features with the introduction of Co indicates a modification of the local vibrational environment associated with the B-site composition. Such changes are consistent with the structural sensitivity of oxynitride perovskites to variations in their cationic and anionic environments[101].

The most pronounced differences among the Mg-based oxynitride nanoparticles are observed in the low-wavenumber region below 700 cm^{-1}. $MgCoO_2N$ exhibits a distinct absorption band at approximately 631 cm^{-1}, together with additional absorption features extending through the 590–510 cm^{-1} region. $MgCu_{0.5}Co_{0.5}O_2N$ also exhibits pronounced absorption features within this region, whereas $MgCuO_2N$ shows comparatively weaker and broader features. These low-wavenumber absorptions are associated with vibrational modes of the metal–anion framework of the oxynitride perovskite structure[102].

The difference between $MgCuO_2N$ and the Co-containing compositions indicates that the substitution of Cu by Co modifies the vibrational response of the Mg-based oxynitride framework. In $MgCu_{0.5}Co_{0.5}O_2N$, the simultaneous presence of Cu and Co at the B-site produces an absorption profile that differs from those of the individual $MgCuO_2N$ and $MgCoO_2N$ compositions. This

behavior reflects the influence of B-site composition on the local vibrational environment of the oxynitride nanoparticle

Overall, the FTIR spectra demonstrate distinct vibrational characteristics for $MgCuO_2N$, $MgCoO_2N$, and $MgCu_{0.5}Co_{0.5}O_2N$. The differences in the absorption features, particularly in the low-wavenumber region, are consistent with changes in the local metal–anion environment resulting from the variation of the B-site cations. The FTIR results therefore provide spectroscopic evidence for differences in the local vibrational environments of the synthesized Mg-based oxynitride nanomaterials[103].

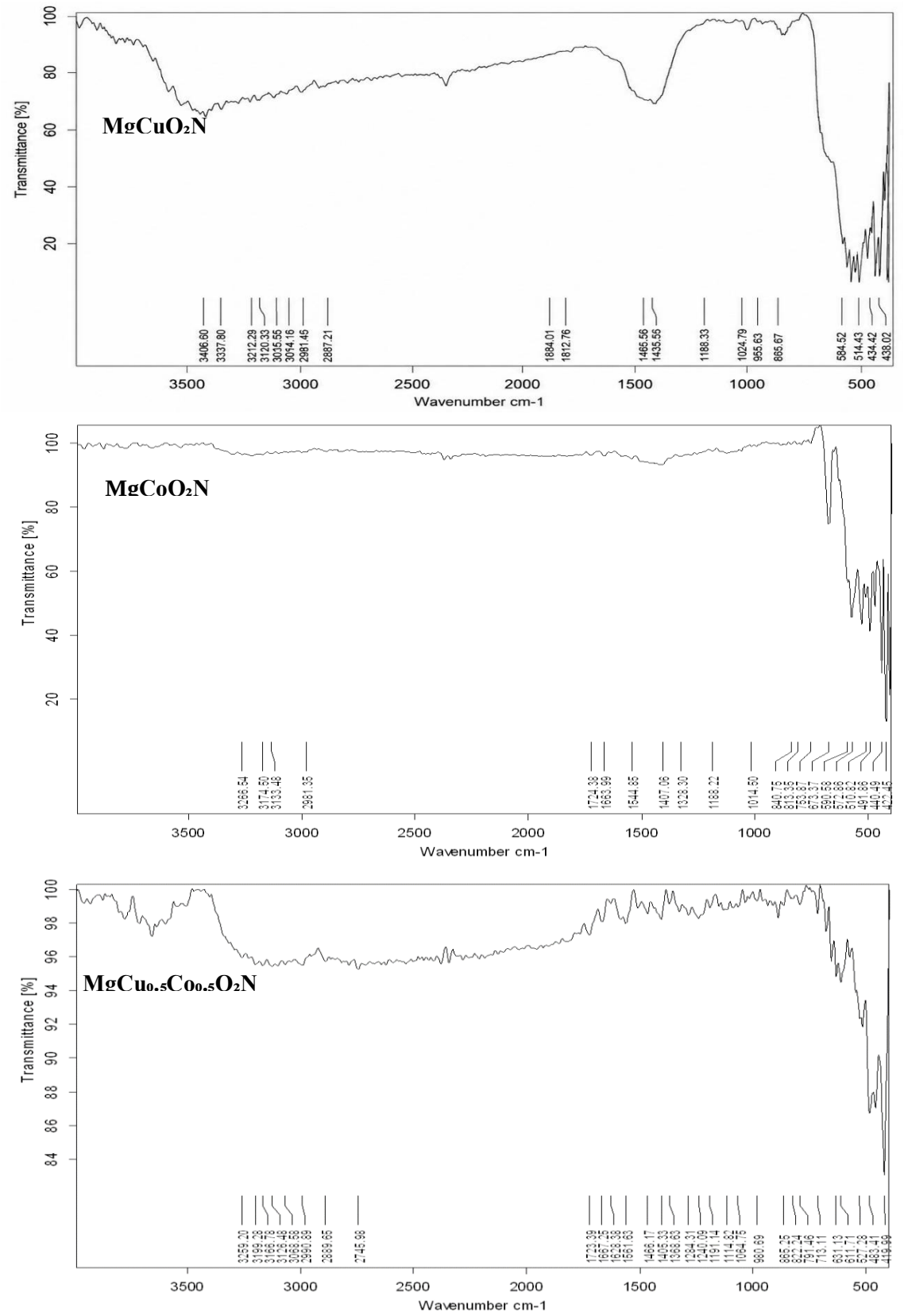


Fig. (3-19): FTIR images of $MgCuO_2N$, $MgCoO_2N$ and $MgCu_{0.5}Co_{0.5}O_2N$ oxynitride perovskites synthesized by the sol–gel Auto-Combustion technique.

3.4.4 Pb-Based Oxynitride Perovskites

The FTIR spectra of $PbCuO_2N$, $PbCoO_2N$, and $PbCu_{0.5}Co_{0.5}O_2N$ oxynitride nanoparticles synthesized by the sol–gel method display clear differences in their vibrational profiles, particularly in the mid- and low-wavenumber regions. These differences reflect the effect of B-site composition on the vibrational response of the Pb-based oxynitride nanomaterials.

For $PbCuO_2N$, the mid-wavenumber region is characterized by a broad and asymmetric absorption profile, with two distinguishable features located at approximately 1407 and 1321 cm^{-1}. The presence of two separated features gives the $PbCuO_2N$ spectrum a broader and more complex profile than those of the Co-containing compositions. In $PbCoO_2N$ and $PbCu_{0.5}Co_{0.5}O_2N$, this region is dominated by a more concentrated absorption feature near 1407 cm^{-1}. The change from the split profile of $PbCuO_2N$ to the more concentrated response of the Co-containing samples indicates that modification of the B-site composition alters the local vibrational environment within the Pb-based oxynitride framework[104].

A more distinctive feature of the Pb-based series is observed below 700 cm^{-1}. $PbCoO_2N$ exhibits two pronounced absorption bands at approximately 665 and 575 cm^{-1}, giving this spectrum a clearly resolved low-wavenumber response. $PbCu_{0.5}Co_{0.5}O_2N$ also retains pronounced absorption features in this region, although their spectral profile differs from that of the single-Co composition. In contrast, the corresponding features in $PbCuO_2N$ are considerably broader and less pronounced. Vibrational modes in this low-wavenumber range are characteristic of the metal–anion framework in inorganic perovskite-type materials and are sensitive to changes in the local coordination environment[101].

The contrast between the three compositions is particularly relevant to the B-site substitution. $PbCuO_2N$ contains Cu as the B-site cation, whereas replacement of Cu by Co in $PbCoO_2N$ produces a markedly different low-wavenumber spectral profile. The mixed $PbCu_{0.5}Co_{0.5}O_2N$ composition does not simply reproduce the spectrum of either parent compound; instead, it exhibits its own combination of absorption features. This indicates that the simultaneous presence of Cu and Co modifies the vibrational response of the Pb-based oxynitride framework.

The absorption features extending toward the lower limit of the spectrum, below approximately 500 cm^{-1}, further contribute to the differentiation of the three Pb-based oxynitride nanoparticles. These low-energy modes are associated with vibrational motions within the metal–anion framework and provide additional evidence that changes in B-site composition are reflected in the infrared response of the synthesized nanomaterials [103].

The Pb-based oxynitride series demonstrates a clear composition-dependent evolution of the FTIR spectra. $PbCuO_2N$ is distinguished by its broad and split mid-wavenumber absorption profile and comparatively less pronounced low-wavenumber features, whereas $PbCoO_2N$ is characterized by clearly resolved bands near 665 and 575 cm^{-1}. The mixed $PbCu_{0.5}Co_{0.5}O_2N$ composition exhibits an intermediate but composition-specific vibrational profile. These spectral variations demonstrate that Cu/Co substitution at the B-site influences the local vibrational environment of the Pb-based oxynitride nanomaterials.

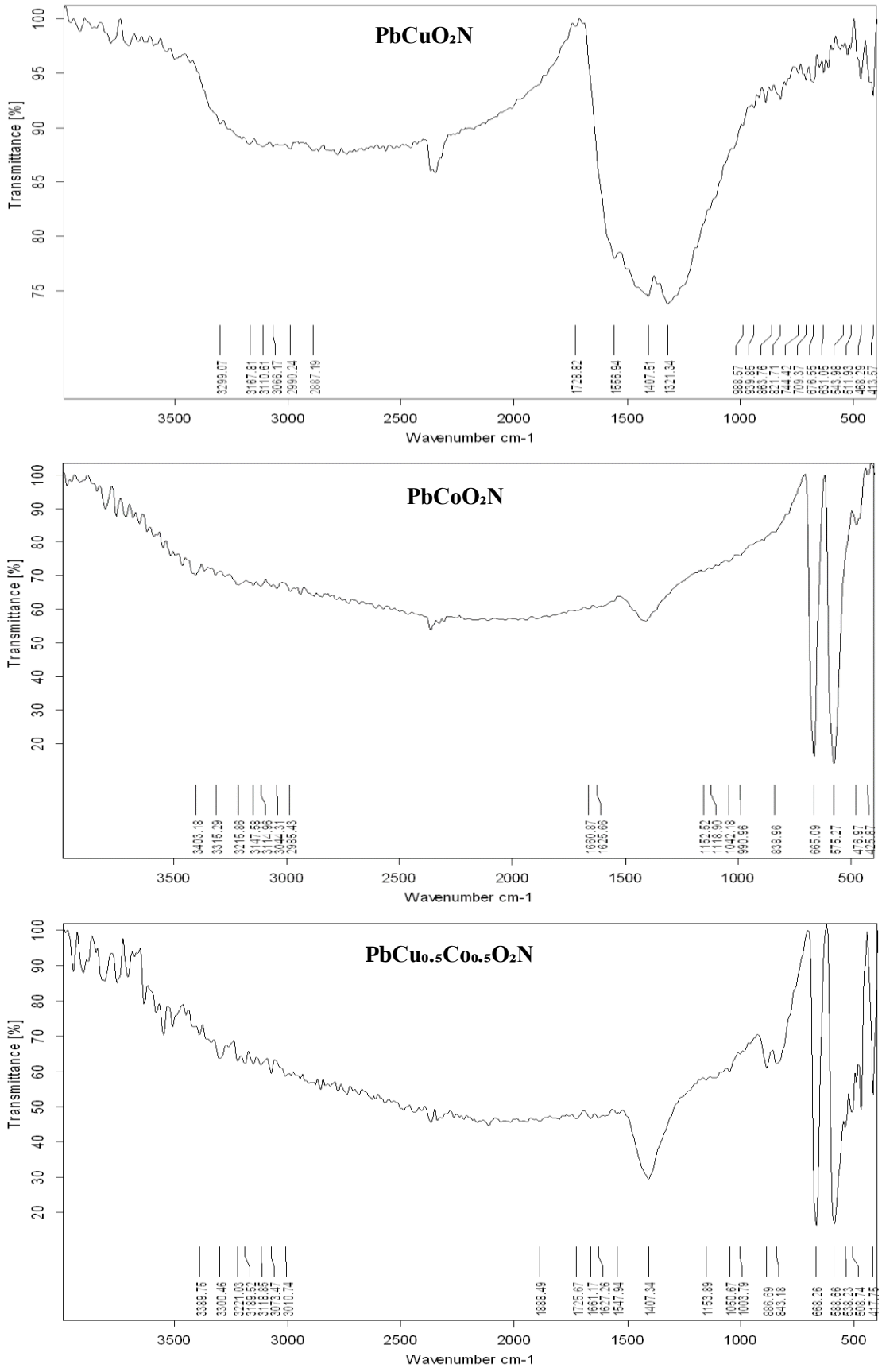


Fig. (3-20): FTIR images of $PbCuO_2N$, $PbCoO_2N$ and $PbCu_{0.5}Co_{0.5}O_2N$ oxynitride perovskites synthesized by the sol–gel Auto-Combustion technique.

3.5 Optical Properties

3.5.1 UV-Vis Spectroscopy

3.5.1.1 Ba-Based Oxynitride Perovskites

The electronic UV–Vis absorption spectra of the Ba-based oxynitride nanoparticles, $BaCuO_2N$, $BaCoO_2N$ and $BaCu_{0.5}Co_{0.5}O_2N$, synthesized by the sol–gel method, are presented in Fig. (3-19). The three oxynitride nanomaterials exhibit different absorption responses over the investigated wavelength range, indicating a clear dependence of their optical behavior on the B-site Cu/Co content. The optical band gaps were calculated using the Tauc relation for direct allowed transitions, $(\alpha h\nu)^2 = B(h\nu - Eg)$, where α is the absorption coefficient, $h\nu$ is the photon energy, B is a proportionality constant, and Eg is the optical band gap. The calculated optical band-gap values were 2.77 eV for $BaCuO_2N$, 2.04 eV for $BaCoO_2N$ and 1.63 eV for $BaCu_{0.5}Co_{0.5}O_2N$.

The results show a clear decrease in the optical band gap with the change in B-site Cu/Co content. $BaCuO_2N$ exhibits the highest Eg value of 2.77 eV, whereas $BaCoO_2N$ shows a lower value of 2.04 eV. A further decrease to 1.63 eV is observed for $BaCu_{0.5}Co_{0.5}O_2N$. This progressive reduction in Eg is accompanied by an extension of the optical absorption response toward the longer-wavelength region, particularly for $BaCu_{0.5}Co_{0.5}O_2N$. Thus, the UV–Vis results indicate that the presence of Cu and Co at the B-site in different proportions is associated with a measurable variation in the optical response of the prepared oxynitride nanoparticles.

The obtained band-gap values demonstrate that the optical properties of the Ba-based oxynitride nanomaterials vary with the B-site Cu/Co content. The decrease in Eg from 2.77 to 1.63 eV reflects a shift toward lower-energy optical absorption as the B-site changes from Cu to Co and then to the mixed Cu–Co oxynitride.

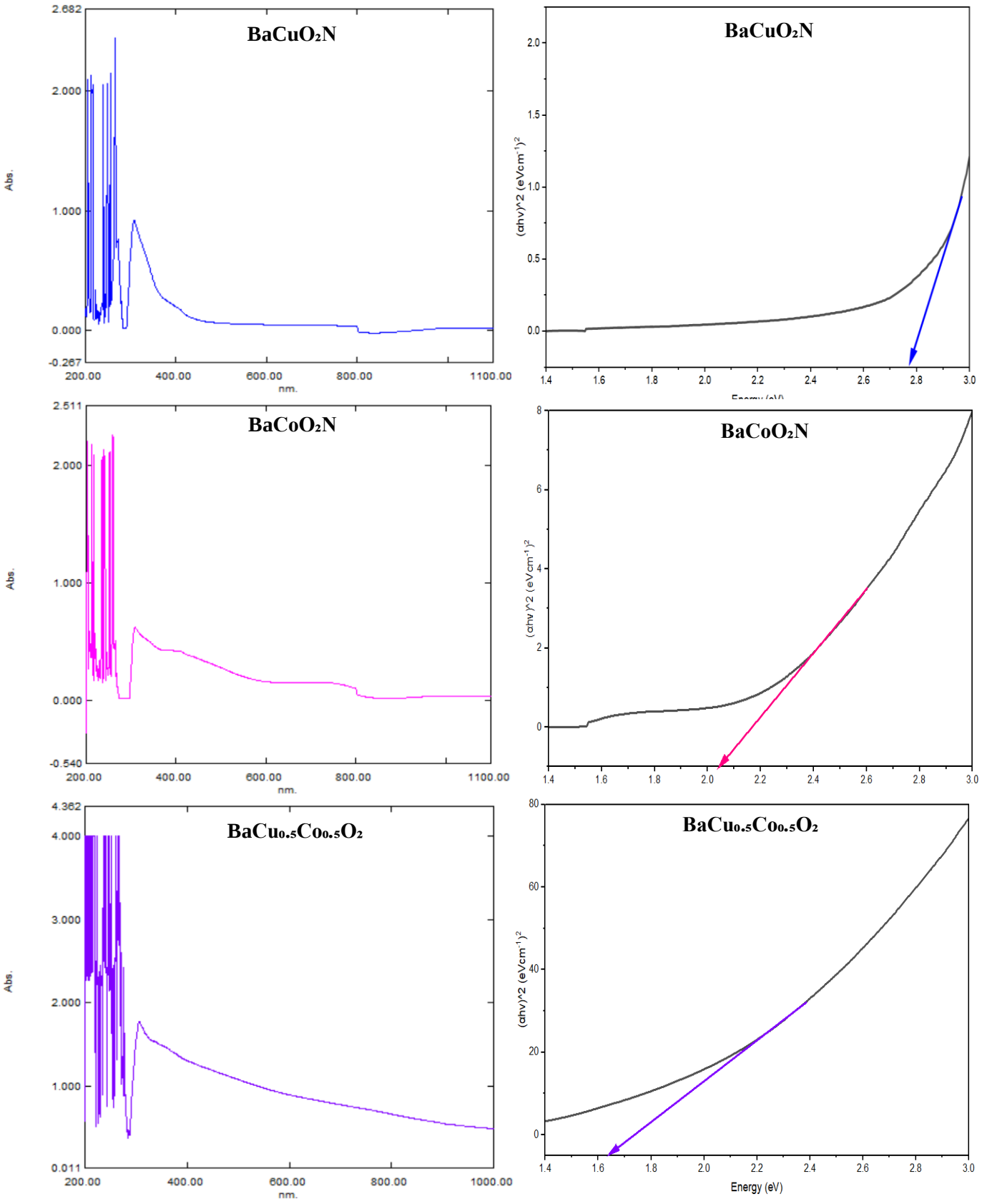


Fig. (3-21): UV–Vis spectra and Tauc plots of $BaCuO_2N$, $BaCoO_2N$ and $BaCu_{0.5}Co_{0.5}O_2N$ oxynitride perovskites synthesized by the sol–gel Auto-Combustion technique.

3.5.1.2 Ca-Based Oxynitride Perovskites

The electronic UV–Vis absorption spectra of the Ca-based oxynitride nanoparticles, $CaCuO_2N$, $CaCoO_2N$ and $CaCu_{0.5}Co_{0.5}O_2N$, synthesized by the sol–gel method, are presented in Fig. (3-22). The three oxynitride nanomaterials exhibit different absorption responses over the investigated wavelength range, indicating a variation in their optical behavior with the Cu/Co content at the B-site. The optical band gaps were calculated using the Tauc relation for direct allowed transitions, $(\alpha h\nu)^2 = B(h\nu - Eg)$, where α is the absorption coefficient, $h\nu$ is the photon energy, B is a proportionality constant, and Eg is the optical band gap. The calculated optical band-gap values were 3.25 eV for $CaCuO_2N$, 2.25 eV for $CaCoO_2N$ and 2.50 eV for $CaCu_{0.5}Co_{0.5}O_2N$.

$CaCuO_2N$ exhibited the highest optical band gap of 3.25 eV, whereas $CaCoO_2N$ showed a lower value of 2.25 eV. The decrease in Eg from $CaCuO_2N$ to $CaCoO_2N$ corresponds to a shift toward lower-energy optical absorption. For $CaCu_{0.5}Co_{0.5}O_2N$, the optical band gap increased to 2.50 eV, indicating that the incorporation of both Cu and Co at the B-site produces an intermediate band-gap value between those obtained for $CaCuO_2N$ and $CaCoO_2N$.

The UV–Vis spectra also show differences in the absorption response among the three oxynitride nanoparticles. $CaCuO_2N$ exhibits its main absorption response at the shorter-wavelength region, consistent with its relatively high band gap. $CaCoO_2N$ shows an extended absorption response toward longer wavelengths, consistent with its lower Eg of 2.25 eV. $CaCu_{0.5}Co_{0.5}O_2N$ exhibits an absorption response between those of $CaCuO_2N$ and $CaCoO_2N$, in agreement with its intermediate Eg value of 2.50 eV.

The obtained band-gap values demonstrate that the optical properties of the Ca-based oxynitride nanomaterials vary with the Cu/Co content at the B-site. The change in Eg from 3.25 eV for $CaCuO_2N$ to 2.25 eV for $CaCoO_2N$, followed by an increase to 2.50 eV for $CaCu_{0.5}Co_{0.5}O_2N$, indicates that the optical response is sensitive to the B-site Cu/Co arrangement.

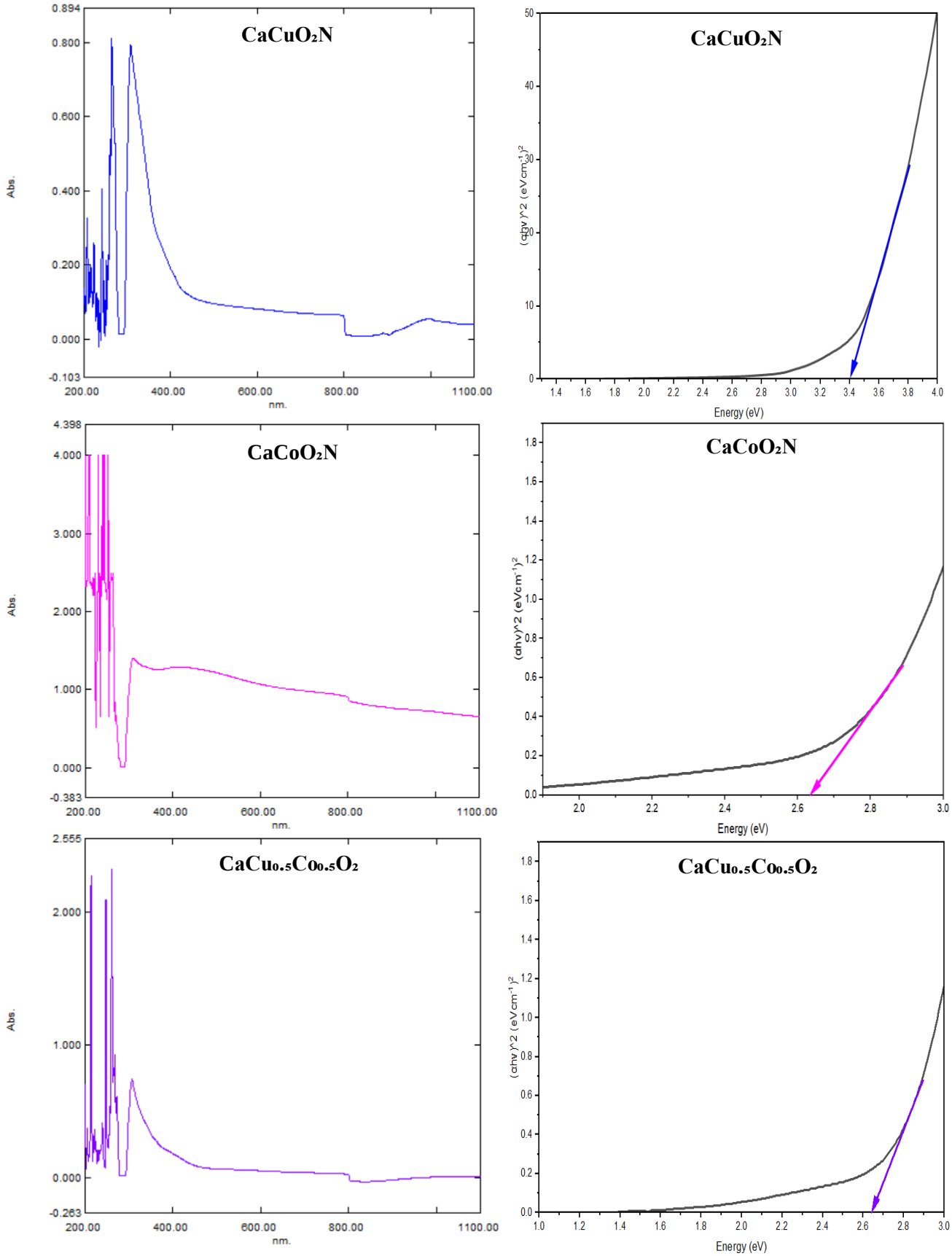


Fig. (3-22): UV–Vis spectra and Tauc plots of $CaCuO_2N$, $CaCoO_2N$ and $CaCu_{0.5}Co_{0.5}O_2N$ oxynitride perovskites synthesized by the sol–gel Auto-Combustion technique.

3.5.1.3 Mg-Based Oxynitride Perovskites

The electronic UV–Vis absorption spectra of the Mg-based oxynitride nanoparticles, $MgCuO_2N$, $MgCoO_2N$ and $MgCu_{0.5}Co_{0.5}O_2N$, synthesized by the sol–gel method, are presented in Fig. (3-23). The three oxynitride nanomaterials exhibit different absorption responses over the investigated wavelength range, indicating a variation in their optical behavior with the Cu/Co content at the B-site. The optical band gaps were calculated using the Tauc relation for direct allowed transitions, $(\alpha h\nu)^2 = B(h\nu - Eg)$, where α is the absorption coefficient, $h\nu$ is the photon energy, B is a proportionality constant, and Eg is the optical band gap. The calculated optical band-gap values were 2.58 eV for $MgCuO_2N$, 2.13 eV for $MgCoO_2N$ and 2.48 eV for $MgCu_{0.5}Co_{0.5}O_2N$.

$MgCuO_2N$ exhibited an optical band gap of 2.58 eV, whereas $MgCoO_2N$ showed a lower value of 2.13 eV. The decrease in Eg from $MgCuO_2N$ to $MgCoO_2N$ corresponds to a shift toward lower-energy optical absorption. For $MgCu_{0.5}Co_{0.5}O_2N$, the optical band gap increased to 2.48 eV, giving a value between those obtained for $MgCuO_2N$ and $MgCoO_2N$.

The UV–Vis spectra show that $MgCuO_2N$ exhibits its main absorption response in the shorter-wavelength region, consistent with its relatively higher band gap. $MgCoO_2N$ shows an extended absorption response toward longer wavelengths, in agreement with its lower Eg of 2.13 eV. $MgCu_{0.5}Co_{0.5}O_2N$ exhibits an absorption response between those observed for $MgCuO_2N$ and $MgCoO_2N$, consistent with its intermediate Eg value of 2.48 eV.

The obtained band-gap values demonstrate that the optical properties of the Mg-based oxynitride nanomaterials vary with the Cu/Co content at the B-site. The change in Eg from 2.58 eV for $MgCuO_2N$ to 2.13 eV for $MgCoO_2N$, followed by an increase to 2.48 eV for $MgCu_{0.5}Co_{0.5}O_2N$, indicates that the optical response is sensitive to the Cu/Co arrangement at the B-site.

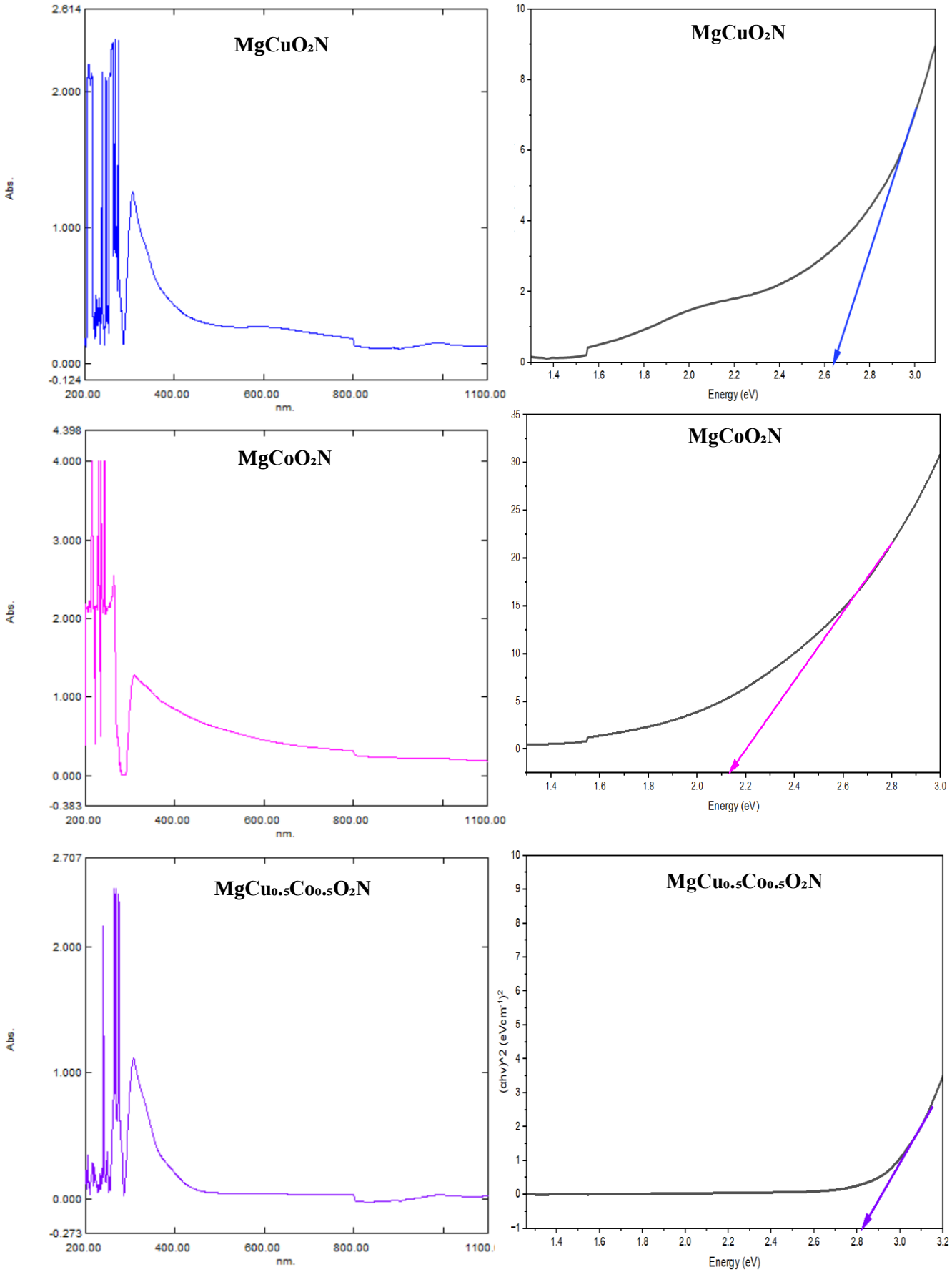


Fig. (3-23): UV–Vis spectra and Tauc plots of $MgCuO_2N$, $MgCoO_2N$ and $MgCu_{0.5}Co_{0.5}O_2N$ oxynitride perovskites synthesized by the sol–gel Auto-Combustion technique.

3.5.1.4 Pb-Based Oxynitride Perovskites

The electronic UV–Vis absorption spectra of the Pb-based oxynitride nanoparticles, $PbCuO_2N$, $PbCoO_2N$ and $PbCu_{0.5}Co_{0.5}O_2N$, synthesized by the sol–gel method, are presented in Fig. (3-24). The three oxynitride nanomaterials exhibit different absorption responses over the investigated wavelength range, indicating a variation in their optical behavior with the Cu/Co content at the B-site.

The optical band gaps were calculated using the Tauc relation for direct allowed transitions, $(\alpha h\nu)^2 = B(h\nu - Eg)$, where α is the absorption coefficient, $h\nu$ is the photon energy, B is a proportionality constant, and Eg is the optical band gap. The calculated optical band-gap values were 2.68 eV for $PbCuO_2N$, 2.26 eV for $PbCoO_2N$ and 2.37 eV for $PbCu_{0.5}Co_{0.5}O_2N$.

$PbCuO_2N$ exhibited the highest optical band gap of 2.68 eV, whereas $PbCoO_2N$ showed a lower value of 2.26 eV. The decrease in Eg from $PbCuO_2N$ to $PbCoO_2N$ corresponds to a shift toward lower-energy optical absorption. For $PbCu_{0.5}Co_{0.5}O_2N$, the optical band gap increased to 2.37 eV, giving an intermediate value between those obtained for $PbCuO_2N$ and $PbCoO_2N$. The UV–Vis spectra show differences in the absorption response of the three oxynitride nanoparticles.

$PbCuO_2N$ exhibits its main absorption response in the shorter-wavelength region, consistent with its relatively higher band gap. $PbCoO_2N$ shows a more extended absorption response toward longer wavelengths, in agreement with its lower Eg of 2.26 eV. $PbCu_{0.5}Co_{0.5}O_2N$ exhibits an absorption response between those observed for $PbCuO_2N$ and $PbCoO_2N$, consistent with its intermediate Eg value of 2.37 eV.

The obtained band-gap values demonstrate that the optical properties of the Pb-based oxynitride nanomaterials vary with the Cu/Co content at the B-site. The change in Eg from 2.68 eV for $PbCuO_2N$ to 2.26 eV for $PbCoO_2N$, followed by an increase to 2.37 eV for $PbCu_{0.5}Co_{0.5}O_2N$, indicates that the optical response varies with the Cu/Co arrangement at the B-site.

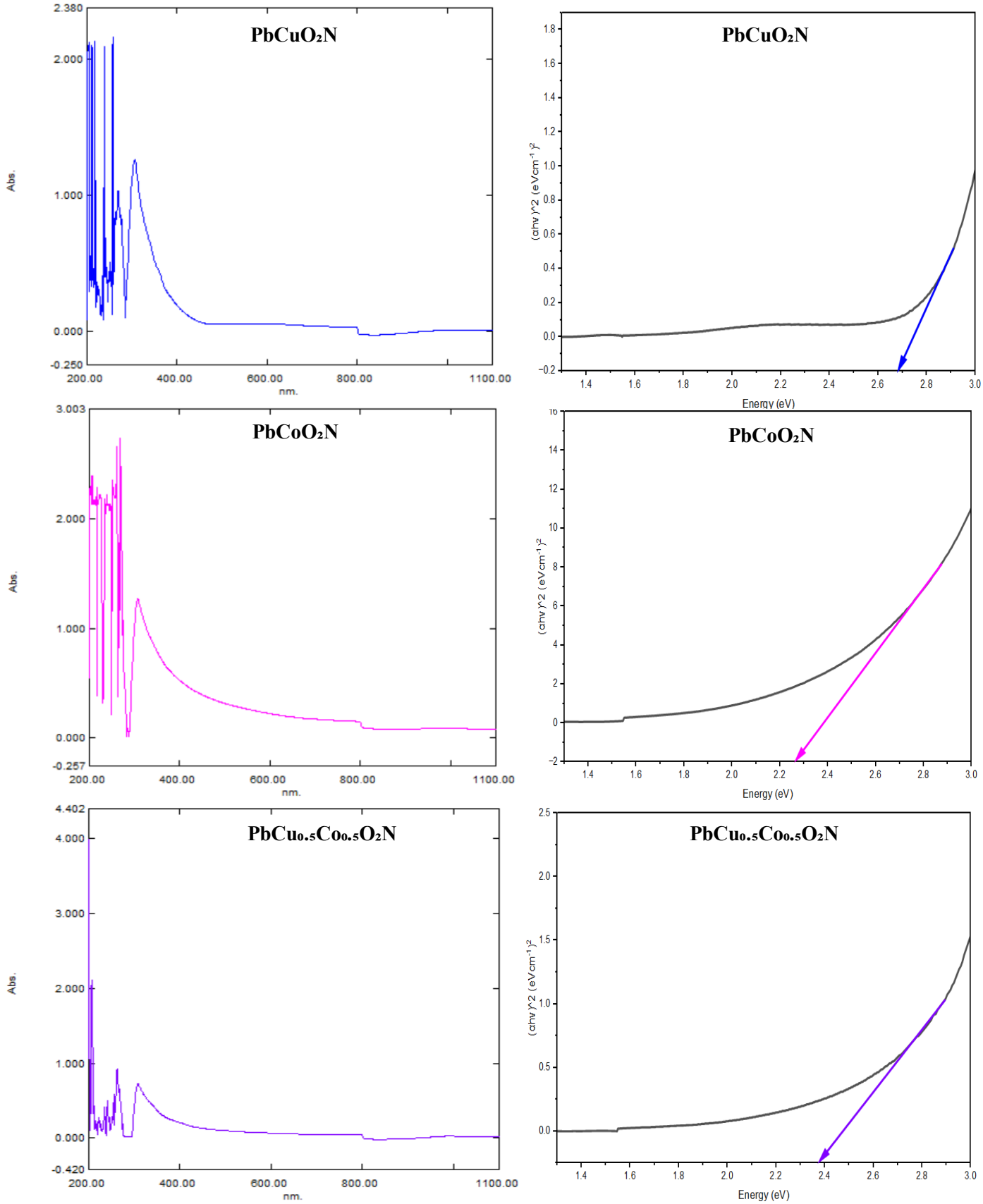


Fig. (3-24): UV–Vis spectra and Tauc plots of $PbCuO_2N$, $PbCoO_2N$ and $PbCu_{0.5}Co_{0.5}O_2N$ oxynitride perovskites synthesized by the sol–gel Auto-Combustion technique.

3.6 Thermogravimetric Analysis (TGA)

3.6.1 Ba-Based Oxynitride Perovskites

Thermal stability and decomposition behavior of the Ba-based oxynitride perovskites, $BaCuO_2N$, $BaCoO_2N$ and $BaCu_{0.5}Co_{0.5}O_2N$, were investigated up to 550 °C using TGA and DTG, as shown in Fig. (3-25). All three oxynitride materials exhibited limited mass loss throughout the investigated temperature range, with total mass losses of approximately 0.20 wt% for $BaCuO_2N$, 0.11 wt% for $BaCoO_2N$ and 0.24 wt% for $BaCu_{0.5}Co_{0.5}O_2N$.

The TGA curves and their corresponding DTG profiles revealed three main regions of mass change below approximately 350 °C, followed by an approximately stable region. For $BaCuO_2N$, the mass losses in the ranges of 25–100, 100–200 and 200–350 °C were approximately 0.088, 0.063 and 0.053 wt%, respectively. $BaCoO_2N$ exhibited corresponding mass losses of approximately 0.026, 0.049 and 0.037 wt%, whereas $BaCu_{0.5}Co_{0.5}O_2N$ showed mass losses of approximately 0.092, 0.071 and 0.079 wt%, respectively.

The initial mass decrease below approximately 100 °C, accompanied by the low-temperature DTG peaks, can be attributed mainly to the desorption of weakly retained surface species and physically adsorbed moisture. The subsequent mass changes between approximately 100 and 200 °C are associated with the removal of thermally weakly retained species, while the broader mass-loss region between approximately 200 and 350 °C indicates further thermally induced processes. The relatively small magnitude of the mass changes in these regions accounts for the low total weight loss observed for all three compositions.

The DTG profiles show clear differences among the three compositions. $BaCuO_2N$ and $BaCoO_2N$ exhibit prominent low-temperature DTG peaks followed by broader features in the intermediate-temperature region. In contrast, $BaCu_{0.5}Co_{0.5}O_2N$ exhibits several distinguishable DTG peaks between approximately 50 and 150 °C, followed by a broader peak around 240–260 °C. These differences indicate that the B-site composition affects the distribution and intensity of the thermal events.

Above approximately 350 °C, the TGA curves become nearly constant, and only negligible mass changes are observed up to 550 °C. The mass changes above this region are approximately 0.002, 0.001 and 0.001 wt% for $BaCuO_2N$, $BaCoO_2N$ and $BaCu_{0.5}Co_{0.5}O_2N$, respectively. Thus, no significant additional mass loss occurs above approximately 350 °C within the investigated temperature range.

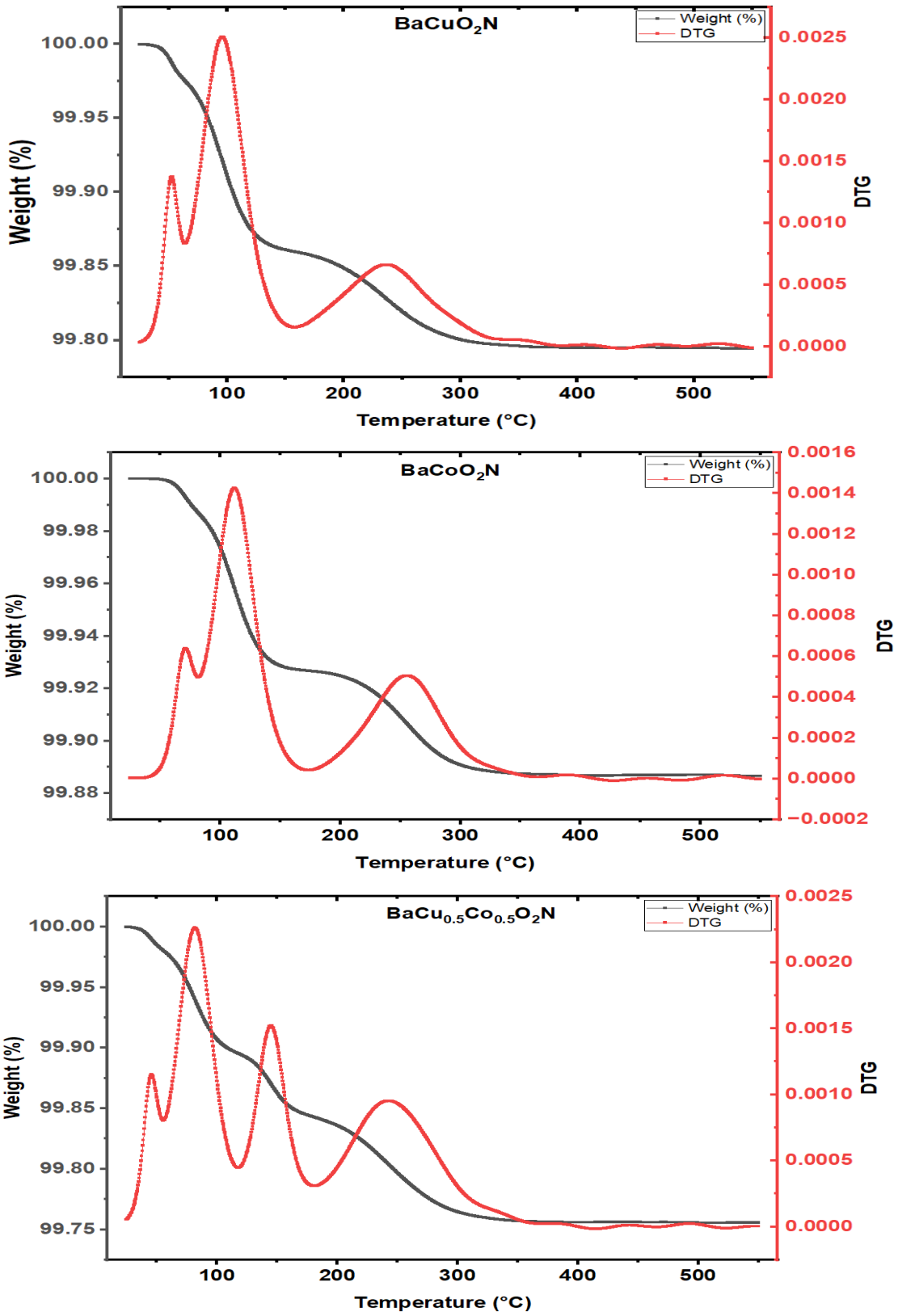


Fig. (3-25): TGA thermograms of $BaCuO_2N$, $BaCoO_2N$ and $BaCu_{0.5}Co_{0.5}O_2N$ oxynitride perovskites synthesized by the sol–gel Auto-Combustion technique.

The kinetic and thermodynamic parameters calculated from the TGA data using the Coats–Redfern method are summarized in Table (3-9). The activation energy (Ea) values are 115,965.6 J mol^{-1} for $BaCuO_2N$, 117,699.6 J mol^{-1} for $BaCoO_2N$ and 112,582.9 J mol^{-1} for $BaCu_{0.5}Co_{0.5}O_2N$. The corresponding enthalpy changes (ΔH) are 113,486.7, 115,220.8 and 110,104.1 J mol^{-1}, respectively. The calculated values demonstrate variations in the kinetic parameters with B-site composition, with $BaCu_{0.5}Co_{0.5}O_2N$ exhibiting the lowest Ea and ΔH values among the investigated compositions.

Table (3-9): Thermodynamic data of $BaCuO_2N$, $BaCoO_2N$ and $BaCu_{0.5}Co_{0.5}O_2N$ oxynitride perovskites synthesized by the sol–gel Auto-Combustion technique.

Perovskites oxynitride	**(ΔE_a) (J/mol)**	**(ΔH) (J/mol)**	**(ΔS) (J $k^{-1}mol^{-1}$)**	**(ΔG) (J/mol)**
$BaCuO_2N$	115965.6	113486.7	87.4518	87413.03
$BaCoO_2N$	117699.6	115220.8	63.39724	96617.09
$BaCu_{0.5}Co_{0.5}O_2N$	112582.9	110104.1	81.33369	85854.46

3.6.2 Ca-Based Oxynitride Perovskites

The thermal behavior of the Ca-based oxynitride perovskites, $CaCuO_2N$, $CaCoO_2N$ and $CaCu_{0.5}Co_{0.5}O_2N$, was investigated up to 550 °C using TGA and DTG, as shown in Fig. (3-26). All three compositions exhibit limited mass loss throughout the investigated temperature range, with the total weight loss remaining below 0.3%. The TGA curves show that the major mass changes occur below approximately 300 °C, followed by an approximately stable region at higher temperatures.

For $CaCuO_2N$, the TGA curve shows an initial gradual decrease in mass at low temperature, followed by a more pronounced decrease extending to approximately 250–300 °C. The corresponding DTG profile exhibits two main thermal features, with a distinct low-temperature peak at approximately 50–80 °C and a broader peak centered around 200–230 °C. $CaCoO_2N$ shows a similar two-step thermal response, with a low-temperature DTG peak followed by a broader peak at approximately 240–270 °C. These features indicate that the observed mass loss occurs mainly through two successive thermal processes below approximately 300 °C.

In contrast, $CaCu_{0.5}Co_{0.5}O_2N$ exhibits a more differentiated DTG profile, with three distinguishable peaks in the low- and intermediate-temperature regions. The first two peaks occur below approximately 150 °C, while a broader thermal feature appears around 220–250 °C. The corresponding TGA curve shows a gradual decrease in mass across these regions. The additional DTG feature indicates that the thermal mass-change behavior of the mixed Cu–Co composition is distributed over a greater number of thermal events than those observed for the single-metal compositions.

The initial mass decrease at low temperature can be associated with the removal of weakly retained surface species and physically adsorbed moisture. The subsequent mass changes at intermediate temperatures represent further thermally induced processes responsible for the observed decrease in mass. The relatively small overall mass loss, together with the stabilization of the TGA curves at higher temperatures, indicates that no substantial additional mass change occurs above approximately 300–350 °C under the investigated conditions.

The kinetic and thermodynamic parameters calculated from the TGA data using the Coats–Redfern method are presented in Table (3-10). The activation energy (Ea) values are 230,528.2 J mol^{-1} for $CaCuO_2N$, 282,465.3 J mol^{-1} for $CaCoO_2N$ and 307,949.2 J mol^{-1} for $CaCu_{0.5}Co_{0.5}O_2N$. The corresponding enthalpy changes (ΔH) are 228,049.4, 279,979.5 and 305,470.4 J mol^{-1}, respectively. Thus, the calculated kinetic parameters increase progressively from $CaCuO_2N$ to $CaCoO_2N$ and $CaCu_{0.5}Co_{0.5}O_2N$, indicating a composition-dependent variation in the energy required for the thermally analyzed process.

The entropy changes (ΔS) are positive for all three compositions, with values of 85.73434 J K^{-1} mol^{-1} for $CaCuO_2N$, 108.26807 J K^{-1} mol^{-1} for $CaCoO_2N$ and 106.32611 J K^{-1} mol^{-1} for $CaCu_{0.5}Co_{0.5}O_2N$. The positive ΔS values indicate an increase in the degree of disorder associated with the activated state during the investigated thermal process. The Gibbs free energy changes (ΔG) are also positive, with values of 202,487.76, 247,608.37 and 273,769.31 J mol^{-1}, respectively. Under the conditions of the thermodynamic calculation, the positive ΔG values indicate that the corresponding thermal processes are non-spontaneous.

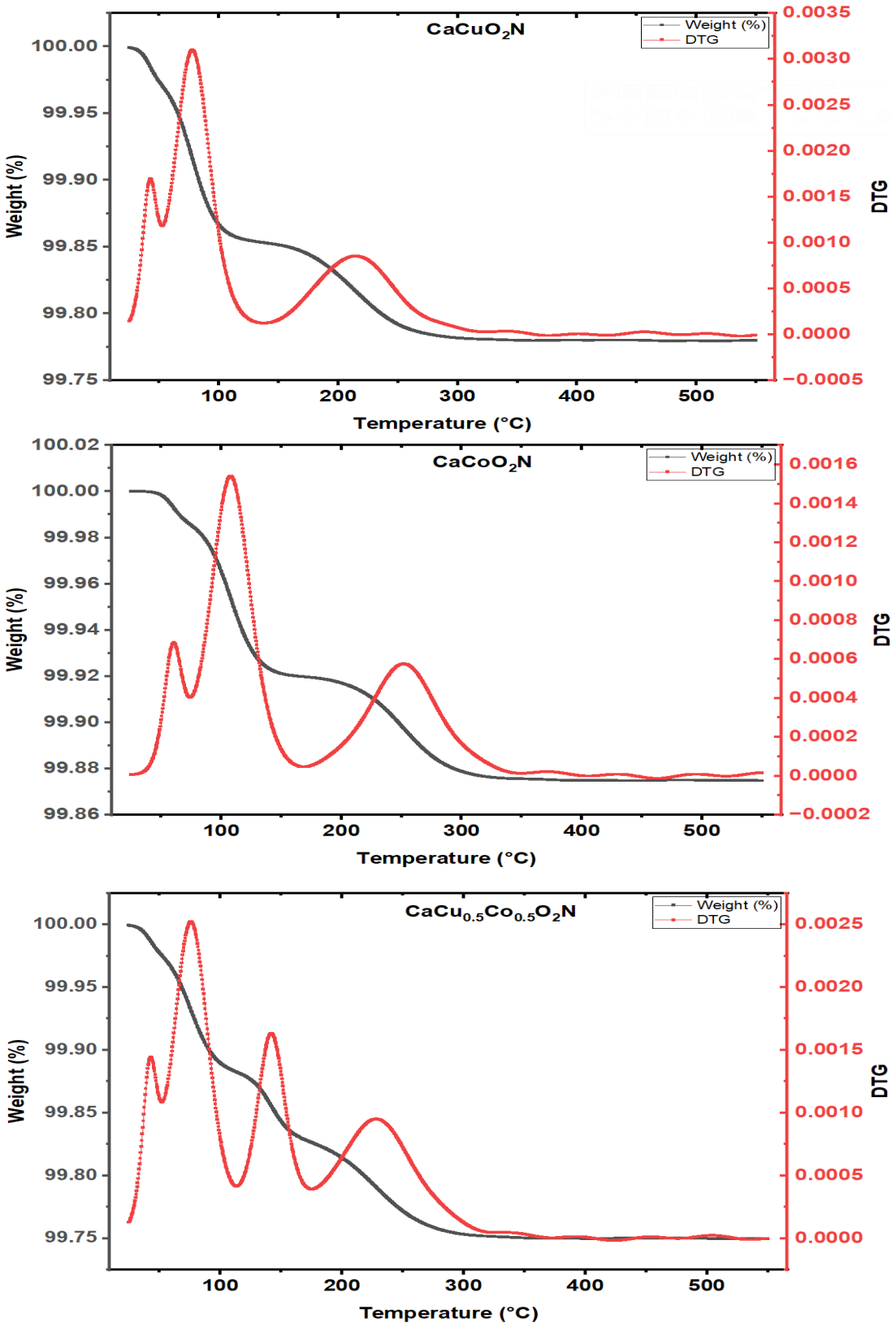


Fig. (3-26): TGA thermograms of $CaCuO_2N$, $CaCoO_2N$ and $CaCu_{0.5}Co_{0.5}O_2N$ oxynitride perovskites synthesized by the sol–gel Auto-Combustion technique.

The TGA/DTG results demonstrate limited mass loss in the Ca-based oxynitride compositions up to 550 °C. The differences in the DTG profiles, particularly the transition from two main thermal features in $CaCuO_2N$ and $CaCoO_2N$ to three distinguishable features in $CaCu_{0.5}Co_{0.5}O_2N$, demonstrate that the B-site composition affects the distribution of thermal events. The kinetic and thermodynamic parameters further show that the thermal behavior of the Ca-based oxynitride compositions varies systematically with the Cu/Co configuration at the B-site.

Table (3-10): Thermodynamic data of $CaCuO_2N$, $CaCoO_2N$ and $CaCu_{0.5}Co_{0.5}O_2N$ oxynitride perovskites synthesized by the sol–gel Auto-Combustion technique.

Perovskites oxynitride	**(ΔE_a) (J/mol)**	**(ΔH) (J/mol)**	**(ΔS) (J $k^{-1}mol^{-1}$)**	**(ΔG) (J/mol)**
$CaCuO_2N$	230528.2	228049.4	85.73434	202487.76
$CaCoO_2N$	282465.3	279979.5	108.26807	247608.37
$CaCu_{0.5}Co_{0.5}O_2N$	307949.2	305470.4	106.32611	273769.31

3.6.3 Mg-Based Oxynitride Perovskites

The thermal behavior of the Mg-based oxynitride perovskites, $MgCuO_2N$, $MgCoO_2N$ and $MgCu_{0.5}Co_{0.5}O_2N$, was investigated up to 550 °C using TGA and DTG, as shown in Fig. (3-27). All three compositions exhibit limited mass loss throughout the investigated temperature range, with the total weight loss remaining below 0.2%. The TGA curves show that the major changes in mass occur below approximately 350 °C, followed by an almost constant mass at higher temperatures.

The $MgCuO_2N$ sample exhibits a gradual initial decrease in weight followed by a more pronounced decrease extending to approximately 300 °C. Its DTG profile is characterized by a low-temperature thermal feature followed by a broad peak centered at approximately 240–260 °C. This indicates that the mass change in $MgCuO_2N$ occurs mainly through two distinguishable thermal events.

$MgCoO_2N$ exhibits a different DTG profile, with a distinct low-temperature peak at approximately 60–80 °C, followed by a more intense peak around 120–140 °C and a broader feature centered at approximately 260–280 °C. The corresponding TGA curve shows a gradual decrease in mass over the same temperature range. Thus, the thermal response of $MgCoO_2N$ is distributed over several distinguishable events rather than the two main features observed for $MgCuO_2N$.

The $MgCu_{0.5}Co_{0.5}O_2N$ composition also exhibits three distinguishable DTG peaks. A low-temperature feature appears around 50–70 °C, followed by a prominent peak near 90–110 °C and another peak around 140–160 °C, with a broader thermal feature centered at approximately 240–260 °C. The corresponding TGA curve shows a continuous decrease in mass until approximately 350 °C, after which the curve becomes nearly constant. The multiple DTG features indicate that the thermal mass-change behavior of the mixed Cu–Co composition occurs through several overlapping or successive thermal events.

The initial mass decrease at low temperature can be associated with the desorption of weakly retained surface species and physically adsorbed moisture. The subsequent changes in mass at intermediate temperatures represent further thermally induced processes. Because TGA/DTG records changes in mass and their temperature distribution, the exact chemical identity of the species

responsible for each individual thermal event cannot be established solely from these curves.

Above approximately 350 °C, the TGA curves of all three compositions approach a nearly constant mass, with only negligible fluctuations observed up to 550 °C. This indicates that no substantial additional mass loss occurs at higher temperatures within the investigated range., The Mg-based oxynitride compositions show limited mass variation, while the differences in the DTG profiles demonstrate that the Cu/Co composition at the B-site affects the distribution of the observed thermal events.

The kinetic and thermodynamic parameters calculated from the TGA data using the Coats–Redfern method are presented in Table (3-11). The activation energy (Ea) values are 362,188.4 J mol^{-1} for $MgCuO_2N$, 162,138.7 J mol^{-1} for $MgCoO_2N$ and 135,761.1 J mol^{-1} for $MgCu_{0.5}Co_{0.5}O_2N$. The corresponding enthalpy changes (ΔH) are 359,709.6, 159,659.9 and 133,282.3 J mol^{-1}, respectively. Thus, the calculated Ea and ΔH values vary substantially with B-site composition, with $MgCuO_2N$ exhibiting the highest values and the mixed Cu–Co composition the lowest values.

The entropy changes (ΔS) are positive for all three compositions, with values of 158.96115 J K^{-1} mol^{-1} for $MgCuO_2N$, 142.66486 J K^{-1} mol^{-1} for $MgCoO_2N$ and 85.4975 J K^{-1} mol^{-1} for $MgCu_{0.5}Co_{0.5}O_2N$. The positive ΔS values indicate an increase in the degree of disorder associated with the activated state during the investigated thermal process. The calculated Gibbs free energy changes (ΔG) are 312,315.3, 117,124.3 and 107,791.2 J mol^{-1} for $MgCuO_2N$, $MgCoO_2N$ and $MgCu_{0.5}Co_{0.5}O_2N$, respectively.

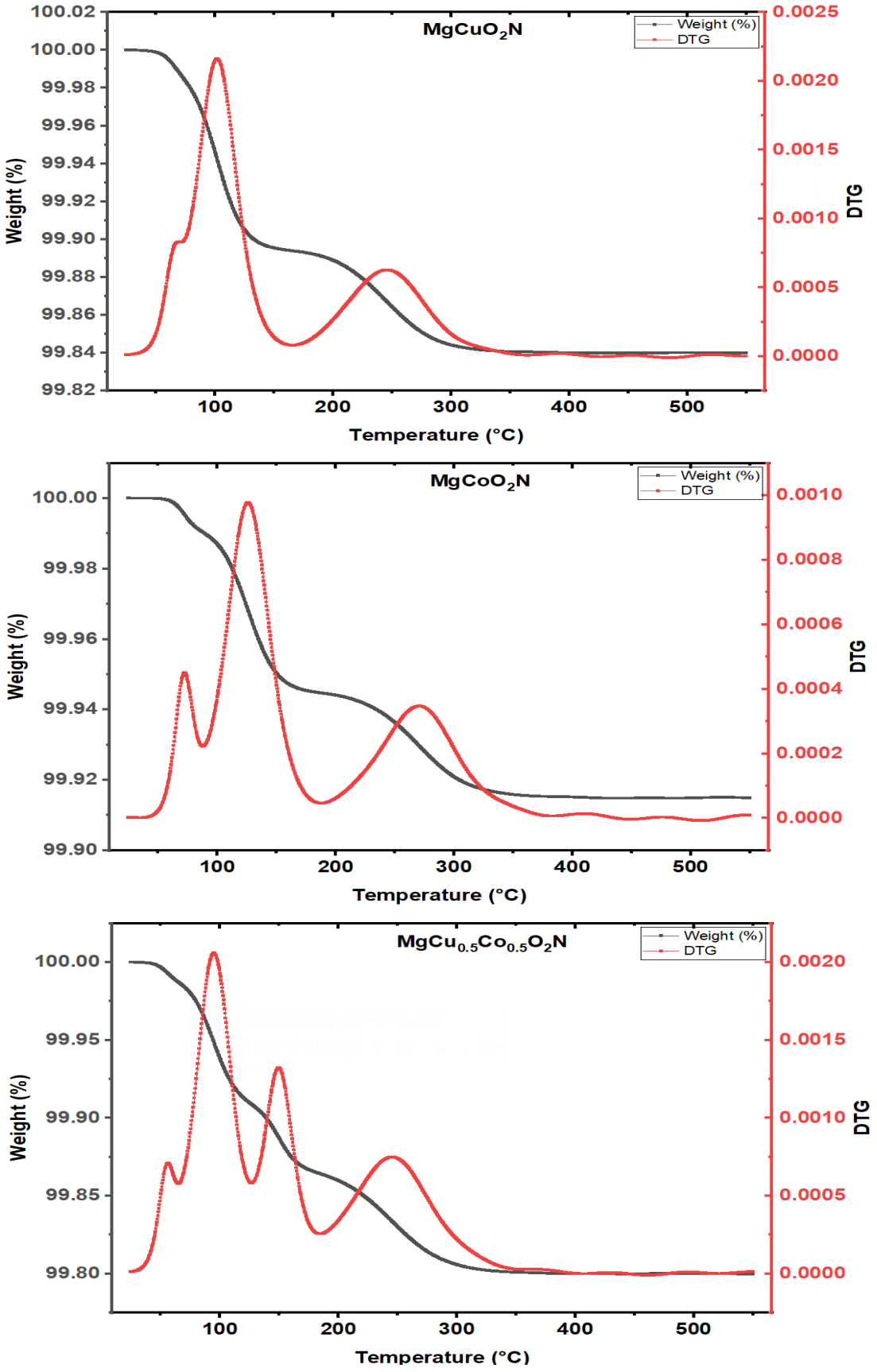


Fig. (3-27): TGA thermograms of $MgCuO_2N$, $MgCoO_2N$ and $MgCu_{0.5}Co_{0.5}O_2N$ oxynitride perovskites synthesized by the sol–gel Auto-Combustion technique.

The TGA/DTG results indicate that the Mg-based oxynitride compositions undergo only limited mass loss up to 550 °C. The distinct differences in the DTG profiles, together with the substantial variation in the calculated kinetic and thermodynamic parameters, demonstrate that changing the Cu/Co composition at the B-site is accompanied by a significant change in the thermal response of the Mg-based oxynitride materials.

Table (3-11): Thermodynamic data of $MgCuO_2N$, $MgCoO_2N$ and $MgCu_{0.5}Co_{0.5}O_2N$ oxynitride perovskites synthesized by the sol–gel Auto-Combustion technique.

Perovskites oxynitride	(ΔE_a) (J/mol)	(ΔH) (J/mol)	(ΔS) (J $k^{-1}mol^{-1}$)	(ΔG) (J/mol)
$MgCuO_2N$	362188.4	359709.6	158.96115	312315.3
$MgCoO_2N$	162138.7	159659.9	142.66486	117124.3
$MgCu_{0.5}Co_{0.5}O_2N$	135761.1	133282.3	85.4975	107791.2

3.6.4 Pb-Based Oxynitride Perovskites

The thermal behavior of the Pb-based oxynitride perovskites, $PbCuO_2N$, $PbCoO_2N$ and $PbCu_{0.5}Co_{0.5}O_2N$, was investigated up to 550 ℃ using TGA and DTG, as shown in Fig. (3-28). All three compositions exhibit limited mass loss throughout the investigated temperature range, with the total weight loss remaining below 0.3%. The TGA curves show that the major changes in mass occur below approximately 300 °C, followed by an almost constant mass at higher temperatures.

The $PbCuO_2N$ sample exhibits an initial decrease in weight at low temperature, followed by a further gradual decrease extending to approximately 250–300 °C. Its DTG profile shows a low-temperature feature followed by a pronounced peak at approximately 65–80 °C and a broader thermal feature centered around 200–220 °C. These features indicate that the observed mass change occurs through more than one thermally distinguishable event, with the main changes concentrated below approximately 300 °C.

$PbCoO_2N$ exhibits a similar overall decrease in mass, but its DTG profile shows a distinct low-temperature peak followed by a more pronounced peak around 80–100 °C and a broader feature centered at approximately 220–250 °C. Compared with $PbCuO_2N$, the position and relative intensity of the DTG features are different, indicating a variation in the thermal response associated with the B-site composition.

The $PbCu_{0.5}Co_{0.5}O_2N$ composition exhibits the most differentiated DTG profile among the three samples. Several distinct thermal features are observed, including low-temperature peaks below approximately 100 °C, an additional peak around 130–150 °C, and a broader feature centered at approximately 210–230 °C. The corresponding TGA curve shows a continuous decrease in mass over these

temperature regions before approaching a nearly constant value above approximately 300–350 °C. The greater number of distinguishable DTG features indicates that the thermal mass-change behavior of the mixed Cu–Co composition is distributed over several thermal events.

The initial mass decrease at low temperature can be associated with the desorption of weakly retained surface species and physically adsorbed moisture. The subsequent mass changes at intermediate temperatures represent additional thermally induced processes. However, the exact chemical identity of the species responsible for the individual DTG peaks cannot be determined solely from TGA/DTG measurements. Therefore, the DTG peaks are interpreted here in terms of the temperature distribution and relative separation of the thermal events rather than assigning them to specific chemical decomposition products.

Above approximately 300–350 °C, the TGA curves approach a nearly constant mass, and only negligible fluctuations are observed up to 550 °C. This indicates that no substantial additional mass loss occurs at higher temperatures within the investigated range., The Pb-based oxynitride compositions exhibit limited mass variation, while the differences in the DTG profiles demonstrate that the Cu/Co configuration at the B-site influences the distribution and complexity of the observed thermal events.

The kinetic and thermodynamic parameters calculated from the TGA data using the Coats–Redfern method are presented in Table (3-12). The activation energy (Ea) values are 116,710.7 J mol^{-1} for $PbCuO_2N$, 134,135.4 J mol^{-1} for $PbCoO_2N$ and 114,359.2 J mol^{-1} for $PbCu_{0.5}Co_{0.5}O_2N$. The corresponding enthalpy changes (ΔH) are 114,231.9, 131,656.5 and 111,880.8 J mol^{-1}, respectively. These values demonstrate a clear variation in the calculated kinetic parameters with B-site composition, with $PbCoO_2N$ exhibiting the highest Ea and ΔH values, whereas $PbCu_{0.5}Co_{0.5}O_2N$ exhibits the lowest values.

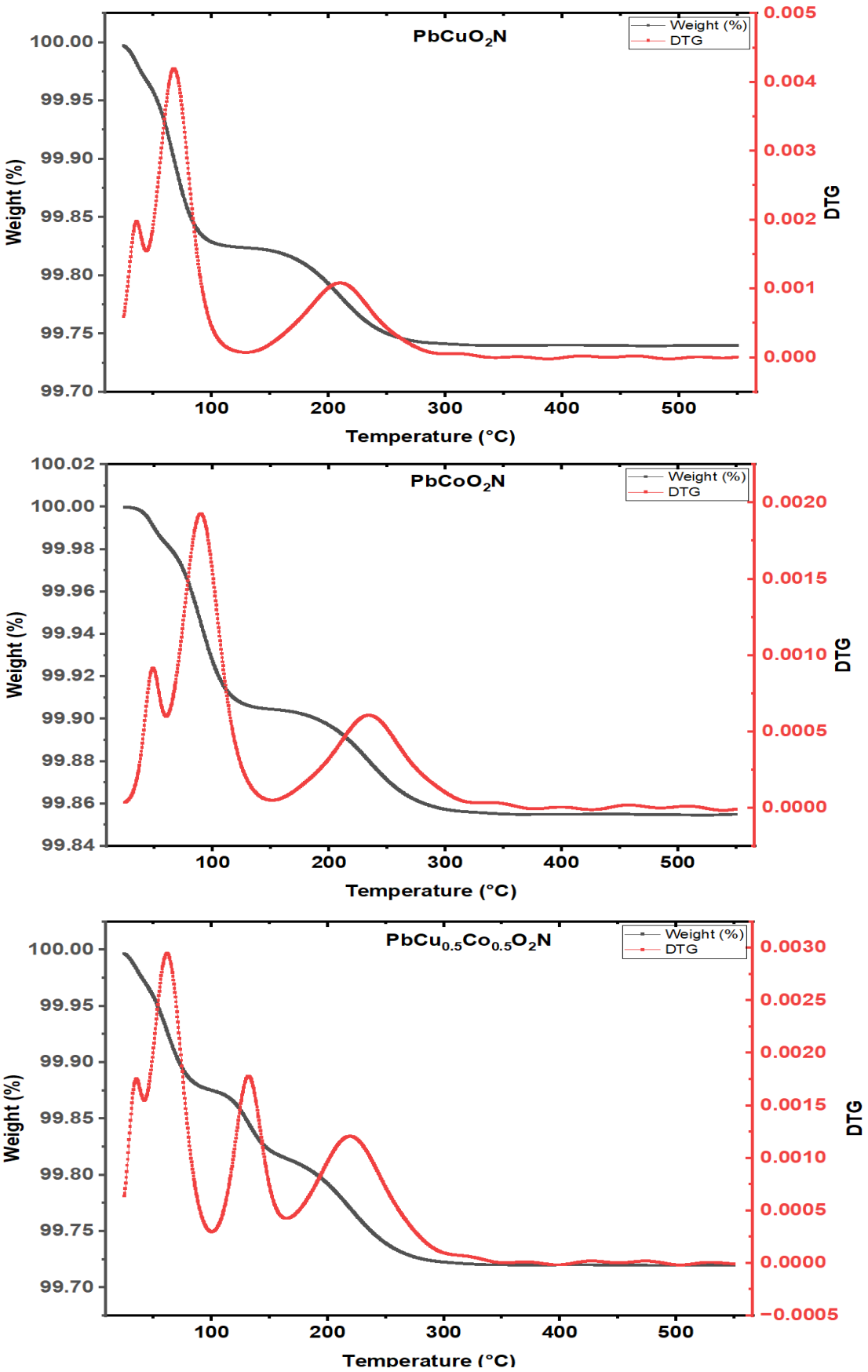


Fig. (3-28): TGA thermograms of $PbCuO_2N$, $PbCoO_2N$ and $PbCu_{0.5}Co_{0.5}O_2N$ oxynitride perovskites synthesized by the sol–gel Auto-Combustion technique

The entropy changes (ΔS) are positive for all three compositions, with values of 55.05688 J K^{-1} mol^{-1} for $PbCuO_2N$, 94.94946 J K^{-1} mol^{-1} for $PbCoO_2N$ and 47.22922 J K^{-1} mol^{-1} for $PbCu_{0.5}Co_{0.5}O_2N$. The positive ΔS values indicate an increase in the degree of disorder associated with the activated state during the investigated thermal process. The calculated Gibbs free energy changes (ΔG) are 97,816.7, 103,347.4 and 97,799.1 J mol^{-1} for $PbCuO_2N$, $PbCoO_2N$ and $PbCu_{0.5}Co_{0.5}O_2N$, respectively.

The TGA/DTG results indicate that the Pb-based oxynitride compositions undergo only limited mass loss up to 550 °C. The differences in the number, position and distribution of the DTG features, particularly the more differentiated profile of $PbCu_{0.5}Co_{0.5}O_2N$, demonstrate that the B-site Cu/Co composition affects the thermal response of the Pb-based oxynitride materials. The calculated kinetic and thermodynamic parameters further confirm that the thermal characteristics vary with the B-site composition.

Table (3-12): Thermodynamic data of $PbCuO_2N$, $PbCoO_2N$ and $PbCu_{0.5}Co_{0.5}O_2N$ oxynitride perovskites synthesized by the sol–gel Auto-Combustion technique.

Perovskites oxynitride	**(ΔE_a) (J/mol)**	**(ΔH) (J/mol)**	**(ΔS) (J $k^{-1}mol^{-1}$)**	**(ΔG) (J/mol)**
$PbCuO_2N$	116710.7	114231.9	55.05688	97816.7
$PbCoO_2N$	134135.4	131656.5	94.94946	103347.4
$PbCu_{0.5}Co_{0.5}O_2N$	114359.2	111880.8	47.22922	97799.1

3.7 Hall Effect

3.7.1 Ba-Based Oxynitride Perovskites

Table (3-13) summarizes the electrical transport parameters obtained from Hall effect measurements for $BaCuO_2N$, $BaCoO_2N$ and $BaCu_{0.5}Co_{0.5}O_2N$ oxynitride nanoparticles. The electrical conductivity values were 6.90, 8.05 and 7.33 S cm^{-1} for $BaCuO_2N$, $BaCoO_2N$ and $BaCu_{0.5}Co_{0.5}O_2N$, respectively. $BaCoO_2N$ exhibited the highest electrical conductivity, whereas $BaCu_{0.5}Co_{0.5}O_2N$ showed an intermediate value.

The carrier concentration was 2.15×10^{17} cm^{-3} for $BaCuO_2N$, 1.62×10^{17} cm^{-3} for $BaCoO_2N$ and 2.05×10^{17} cm^{-3} for $BaCu_{0.5}Co_{0.5}O_2N$. The corresponding carrier mobilities were 201, 311 and 223 cm^2 V^{-1} s^{-1}, respectively. Although $BaCoO_2N$ exhibited the lowest carrier concentration, it showed the highest carrier mobility, which is consistent with its highest measured electrical conductivity. $BaCu_{0.5}Co_{0.5}O_2N$ exhibited a carrier concentration close to that of $BaCuO_2N$, while its carrier mobility was higher than that of $BaCuO_2N$ and lower than that of $BaCoO_2N$.

The Hall coefficient was positive for all three oxynitride nanoparticles, with values of 29.1, 38.6 and 30.4 cm^3 C^{-1} for $BaCuO_2N$, $BaCoO_2N$ and $BaCu_{0.5}Co_{0.5}O_2N$, respectively. The positive Hall coefficient confirms that holes are the predominant charge carriers in all three oxynitrides, indicating p-type semiconducting behavior. The differences in electrical conductivity, carrier concentration and mobility demonstrate that the Cu/Co content at the B-site influences the electrical transport properties of the Ba-based oxynitride nanomaterials.

Table (3-13): Hall effect data of $BaCuO_2N$, $BaCoO_2N$ and $BaCu_{0.5}Co_{0.5}O_2N$ oxynitride perovskites synthesized by the sol–gel Auto-Combustion technique.

Nano Perovskite oxynitride	Conductivity $(S.cm^{-1})$	Bulk concentration cm^{-3}	Mobility $cm^2.V^{-1}.s^{-1}$	Hall Coefficient $cm^3.C^{-1}$
$BaCuO_2N$	6.90E+00	2.15E+17	2.01E+02	2.91E+01
$BaCoO_2N$	8.05E+00	1.62E+17	3.11E+02	3.86E+01
$BaCu_{0.5}Co_{0.5}O_2N$	7.33E+00	2.05E+17	2.23E+02	3.04E+01

The Hall effect measurements confirm p-type electrical conduction in the Ba-based oxynitride nanoparticles, with measurable differences in conductivity, carrier concentration and mobility among $BaCuO_2N$, $BaCoO_2N$ and $BaCu_{0.5}Co_{0.5}O_2N$.

3.7.2 Ca-Based Oxynitride Perovskites

Table (3-14) summarizes the electrical transport parameters obtained from Hall effect measurements for $CaCuO_2N$, $CaCoO_2N$ and $CaCu_{0.5}Co_{0.5}O_2N$ oxynitride nanoparticles. The electrical conductivity values were 8.27×10^{-4}, 1.70×10^{-3} and 1.38×10^{-3} S cm^{-1} for $CaCuO_2N$, $CaCoO_2N$ and $CaCu_{0.5}Co_{0.5}O_2N$, respectively. Thus, $CaCoO_2N$ exhibited the highest electrical conductivity, followed by $CaCu_{0.5}Co_{0.5}O_2N$ and $CaCuO_2N$.

The carrier concentration was 6.50×10^{13} cm^{-3} for $CaCuO_2N$, 7.75×10^{12} cm^{-3} for $CaCoO_2N$ and 1.26×10^{13} cm^{-3} for $CaCu_{0.5}Co_{0.5}O_2N$. The corresponding carrier mobilities were 7.94×10^{1}, 1.37×10^{2} and 6.85×10^{2} cm^2 V^{-1} s^{-1}, respectively. $CaCuO_2N$ exhibited the highest carrier concentration, whereas $CaCoO_2N$ showed a lower carrier concentration accompanied by a higher mobility. The mixed Cu–Co oxynitride exhibited the highest carrier

mobility among the investigated nanoparticles, despite having a carrier concentration lower than that of $CaCuO_2N$.

The Hall coefficient was positive for all three oxynitride nanoparticles, with values of 9.60×10^4, 8.05×10^5 and 4.96×10^5 $cm^3\ C^{-1}$ for $CaCuO_2N$, $CaCoO_2N$ and $CaCu_{0.5}Co_{0.5}O_2N$, respectively. The positive Hall coefficient confirms that holes are the predominant charge carriers, indicating p-type semiconducting behavior for all three oxynitride nanoparticles.

The variation in electrical conductivity among the investigated nanomaterials is associated with differences in both carrier concentration and mobility. In particular, the relatively high conductivity of $CaCoO_2N$ is accompanied by the highest carrier mobility among the single-metal oxynitrides, whereas $CaCu_{0.5}Co_{0.5}O_2N$ exhibits a markedly higher mobility despite its relatively low carrier concentration. These results demonstrate that the Cu/Co content at the B-site affects the electrical transport parameters of the Ca-based oxynitride nanomaterials.

Table (3-14): Hall effect data of $CaCuO_2N$, $CaCoO_2N$ and $CaCu_{0.5}Co_{0.5}O_2N$ oxynitride perovskites synthesized by the sol–gel Auto-Combustion technique.

Perovskites oxynitride	**Conductivity** $S.cm^{-1}$	**Bulk concentration** cm^{-3}	**Mobility** $cm^2.V^{-1}.s^{-1}$	**Hall Coefficient** $cm^3.C^{-1}$
$CaCuO_2N$	8.27E-04	6.50E+13	7.94E+01	9.60E+04
$CaCoO_2N$	1.70E-03	7.75E+12	1.37E+03	8.05E+05
$CaCu_{0.5}Co_{0.5}O_2N$	1.38E-03	1.26E+13	6.85E+02	4.96E+05

The Hall effect measurements confirm p-type electrical conduction in $CaCuO_2N$, $CaCoO_2N$ and $CaCu_{0.5}Co_{0.5}O_2N$, with clear differences in conductivity, carrier concentration and carrier mobility among the investigated oxynitride nanoparticles.

3.7.3 Mg-Based Oxynitride Perovskites

Table (3-15), summarizes the electrical transport parameters obtained from Hall effect measurements for $MgCuO_2N$, $MgCoO_2N$ and $MgCu_{0.5}Co_{0.5}O_2N$ oxynitride nanoparticles. The electrical conductivity values were 4.86×10^{-4}, 4.36×10^{-4} and 1.19×10^{-3} S cm^{-1} for $MgCuO_2N$, $MgCoO_2N$ and $MgCu_{0.5}Co_{0.5}O_2N$, respectively. $MgCu_{0.5}Co_{0.5}O_2N$ exhibited the highest electrical conductivity among the investigated oxynitride nanoparticles.

The carrier concentration was 2.21×10^{12} cm^{-3} for $MgCuO_2N$, 1.32×10^{12} cm^{-3} for $MgCoO_2N$ and 1.54×10^{13} cm^{-3} for $MgCu_{0.5}Co_{0.5}O_2N$. The corresponding carrier mobilities were 1.37×10^3, 2.06×10^3 and 4.85×10^3 $cm^2 V^{-1} s^{-1}$, respectively. Thus, $MgCu_{0.5}Co_{0.5}O_2N$ exhibited both the highest carrier concentration and the highest carrier mobility, which is consistent with its higher electrical conductivity. In comparison, $MgCuO_2N$ showed a higher carrier concentration than $MgCoO_2N$, whereas $MgCoO_2N$ exhibited higher carrier mobility.

The Hall coefficient was positive for all three oxynitride nanoparticles, with values of 2.82×10^6, 4.72×10^6 and 4.06×10^6 $cm^3 C^{-1}$ for $MgCuO_2N$, $MgCoO_2N$ and $MgCu_{0.5}Co_{0.5}O_2N$, respectively. The positive Hall coefficient confirms that holes are the predominant charge carriers, indicating p-type semiconducting behavior in all three oxynitride nanoparticles.

The electrical transport parameters show a clear variation with the Cu/Co content at the B-site. In particular, the higher conductivity of $MgCu_{0.5}Co_{0.5}O_2N$ is accompanied by substantially higher carrier concentration and mobility compared with $MgCuO_2N$ and $MgCoO_2N$. These results indicate that the Cu/Co configuration at the B-site has a measurable effect on the electrical transport properties of the Mg-based oxynitride nanomaterials.

Table (3-15): Hall effect data of $MgCuO_2N$, $MgCoO_2N$ and $MgCu_{0.5}Co_{0.5}O_2N$ oxynitride perovskites synthesized by the sol–gel Auto-Combustion technique.

Perovskites oxynitride	**Conductivity** $S.cm^{-1}$	**Bulk concentration** cm^{-3}	**Mobility** $cm^2.V^{-1}.s^{-1}$	**Hall Coefficient** $cm^3.C^{-1}$
$MgCuO_2N$	4.86E-04	2.21E+12	1.37E+03	2.82E+06
$MgCoO_2N$	4.36E-04	1.32E+12	2.06E+03	4.72E+06
$MgCu_{0.5}Co_{0.5}O_2N$	1.19E-03	1.54E+13	4.85E+03	4.06E+06

The Hall effect measurements confirm p-type electrical conduction in $MgCuO_2N$, $MgCoO_2N$ and $MgCu_{0.5}Co_{0.5}O_2N$, with distinct differences in electrical conductivity, carrier concentration and carrier mobility among the investigated oxynitride nanoparticles.

3.7.4 Pb-Based Oxynitride Perovskites

Table (3-16) presents the electrical transport parameters obtained from Hall effect measurements for $PbCuO_2N$, $PbCoO_2N$ and $PbCu_{0.5}Co_{0.5}O_2N$ oxynitride nanoparticles. The electrical conductivity values were 3.75×10^{-4}, 6.67×10^{-4} and 6.11×10^{-4} S cm^{-1} for $PbCuO_2N$, $PbCoO_2N$ and $PbCu_{0.5}Co_{0.5}O_2N$, respectively. $PbCoO_2N$ exhibited the highest electrical conductivity, while $PbCu_{0.5}Co_{0.5}O_2N$ showed an intermediate value.

The carrier concentration was 8.10×10^{12} cm^{-3} for $PbCuO_2N$, 1.04×10^{13} cm^{-3} for $PbCoO_2N$ and 8.30×10^{12} cm^{-3} for $PbCu_{0.5}Co_{0.5}O_2N$. Thus, $PbCoO_2N$ exhibited the highest carrier concentration, whereas $PbCuO_2N$ and $PbCu_{0.5}Co_{0.5}O_2N$ showed relatively similar values. The corresponding carrier mobilities were 2.89×10^2, 4.01×10^2 and 4.60×10^2 cm^2 V^{-1} s^{-1}, respectively. $PbCu_{0.5}Co_{0.5}O_2N$ exhibited the highest carrier mobility among the investigated oxynitride nanoparticles, followed by $PbCoO_2N$ and $PbCuO_2N$.

The Hall coefficient was positive for all three oxynitride nanoparticles, with values of 7.70×10^5, 6.02×10^5 and 7.52×10^5 cm^3 C^{-1} for $PbCuO_2N$, $PbCoO_2N$ and $PbCu_{0.5}Co_{0.5}O_2N$, respectively. The positive Hall coefficient confirms that holes are the predominant charge carriers, indicating p-type semiconducting behavior in all three oxynitride nanoparticles.

The variation in electrical conductivity is accompanied by changes in both carrier concentration and mobility. $PbCoO_2N$ combines the highest carrier concentration with a relatively high carrier mobility, resulting in the highest measured electrical conductivity. In contrast, $PbCu_{0.5}Co_{0.5}O_2N$ exhibits the highest carrier mobility despite its carrier concentration being close to that of $PbCuO_2N$. These results demonstrate that the Cu/Co content at the B-site affects the electrical transport parameters of the Pb-based oxynitride nanomaterials.

Table (3-16): Hall effect data of $PbCuO_2N$, $PbCoO_2N$ and $PbCu_{0.5}Co_{0.5}O_2N$ oxynitride perovskites synthesized by the sol–gel Auto-Combustion technique.

Perovskites oxynitride	**Conductivity** $S.cm^{-1}$	**Bulk concentration** cm^{-3}	**Mobility** $cm^2.V^{-1}.s^{-1}$	**Hall Coefficient** $cm^3.C^{-1}$
$PbCuO_2N$	3.75E-04	8.10E+12	2.89E+02	7.70E+05
$PbCoO_2N$	6.67E-04	1.04E+13	4.01E+02	6.02E+05
$PbCu_{0.5}Co_{0.5}O_2N$	6.11E-04	8.30E+12	4.60E+02	7.52E+05

The Hall effect measurements confirm p-type electrical conduction in $PbCuO_2N$, $PbCoO_2N$ and $PbCu_{0.5}Co_{0.5}O_2N$, with measurable differences in electrical conductivity, carrier concentration and mobility among the investigated oxynitride nanoparticles.

3.8 Solar Cell Applications

3.8.1 Ba-Based Oxynitride Perovskites

The photovoltaic characteristics of the synthesized oxynitride nanoparticles were evaluated from current density–voltage (J–V) measurements, as shown in Fig. (3-29), and the corresponding photovoltaic parameters are summarized in Table (3-17). The J–V curves show clear photovoltaic responses for $BaCuO_2N$, $BaCoO_2N$ and $BaCu_{0.5}Co_{0.5}O_2N$, with distinct values of short-circuit current density (Jsc), open-circuit voltage (Voc), maximum current density (Jmax), maximum voltage (Vmax), fill factor (FF) and power conversion efficiency (PCE).

The short-circuit current densities were 15.30, 25.15 and 24.45 mA cm^{-2} for $BaCuO_2N$, $BaCoO_2N$ and $BaCu_{0.5}Co_{0.5}O_2N$, respectively. $BaCoO_2N$ exhibited

the highest Jsc, followed by $BaCu_{0.5}Co_{0.5}O_2N$, whereas $BaCuO_2N$ showed the lowest value. The relatively high Jsc values obtained for $BaCoO_2N$ and $BaCu_{0.5}Co_{0.5}O_2N$ indicate higher photocurrent generation under the applied measurement conditions.

The open-circuit voltage values were 0.93, 0.85 and 0.63 V for $BaCuO_2N$, $BaCoO_2N$ and $BaCu_{0.5}Co_{0.5}O_2N$, respectively. $BaCuO_2N$ exhibited the highest Voc, while $BaCu_{0.5}Co_{0.5}O_2N$ showed the lowest value. The maximum current densities (Jmax) were 14.07, 23.42 and 22.18 mA cm^{-2}, while the corresponding maximum voltages (Vmax) were 0.75, 0.67 and 0.49 V, respectively.

The fill factor values were 0.738 for $BaCuO_2N$, 0.734 for $BaCoO_2N$ and 0.705 for $BaCu_{0.5}Co_{0.5}O_2N$. The relatively close FF values of $BaCuO_2N$ and $BaCoO_2N$ indicate similar squareness of their J–V characteristics, whereas the lower FF obtained for $BaCu_{0.5}Co_{0.5}O_2N$ reflects a greater difference between its maximum-power point and the product of Jsc and Voc.

The calculated power conversion efficiencies were 10.60%, 15.77% and 10.86% for $BaCuO_2N$, $BaCoO_2N$ and $BaCu_{0.5}Co_{0.5}O_2N$, respectively. $BaCoO_2N$ exhibited the highest PCE of 15.77%, which is consistent with its high Jsc together with a relatively high Voc and FF. Although $BaCu_{0.5}Co_{0.5}O_2N$ exhibited a Jsc of 24.45 mA cm^{-2}, its lower Voc of 0.63 V and FF of 0.705 resulted in a PCE of 10.86%. $BaCuO_2N$ showed the highest Voc of 0.93 V and a comparable FF of 0.738, but its lower Jsc of 15.30 mA cm^{-2} resulted in a PCE of 10.60%.

The J–V measurements demonstrate that the photovoltaic response of the Ba-based oxynitride nanomaterials varies according to the Cu/Co content at the B-site. The measured PCE values confirm photovoltaic activity for all three oxynitride nanoparticles under the applied measurement conditions, with the obtained efficiency determined by the combined contribution of Jsc, Voc and FF.

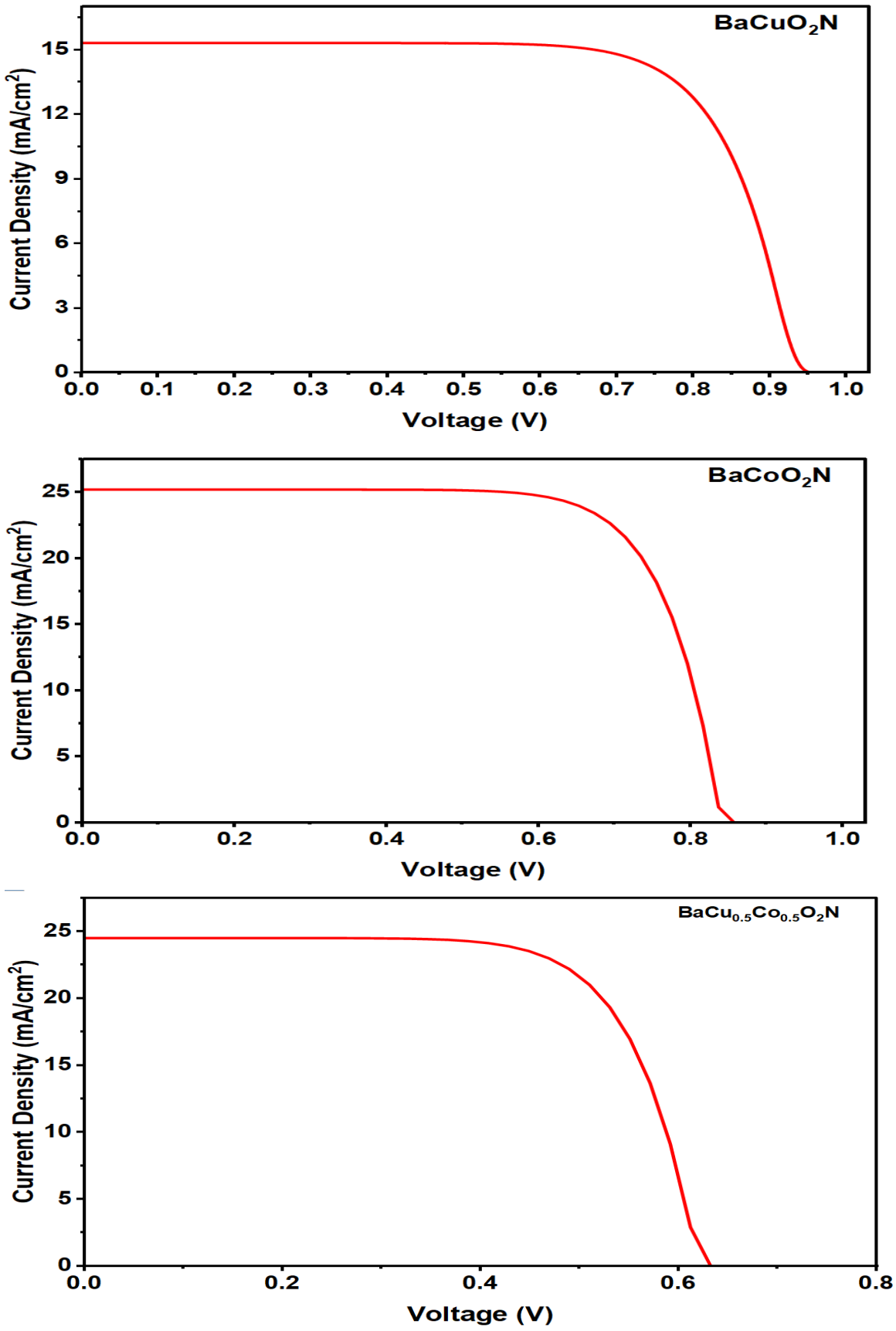


Fig. (3-29): J-V curves of $BaCuO_2N$, $BaCoO_2N$ and $BaCu_{0.5}Co_{0.5}O_2N$ oxynitride perovskites synthesized by the sol–gel Auto-Combustion technique.

Table (3-17) solar cells Parameters of $BaCuO_2N$, $BaCoO_2N$ and $BaCu_{0.5}Co_{0.5}O_2N$.

Parameter	**$BaCuO_2N$**	**$BaCoO_2N$**	**$BaCu_{0.5}Co_{0.5}O_2N$**
Jsc (mA/cm²)	15.30	25.15	24.45
Voc (V)	0.93	0.85	0.63
Jmax (mA/cm²)	14.07	23.42	22.18
Vmax (V)	0.75	0.67	0.49
FF	0.738	0.734	0.705
PCE/ Efficiency (%)	10.60%	15.77%	10.86%

3.8.2 Ca-Based Oxynitride Perovskites

The photovoltaic characteristics of the Ca-based oxynitride nanoparticles were evaluated from current density–voltage (J–V) measurements, as shown in Fig. (3-30), and the corresponding photovoltaic parameters are summarized in Table (3-18). The J–V curves exhibit clear photovoltaic responses for $CaCuO_2N$, $CaCoO_2N$ and $CaCu_{0.5}Co_{0.5}O_2N$, with different values of short-circuit current density (Jsc), open-circuit voltage (Voc), maximum current density (Jmax), maximum voltage (Vmax), fill factor (FF) and power conversion efficiency (PCE).

The short-circuit current densities were 12.99, 30.48 and 17.48 mA cm^{-2} for $CaCuO_2N$, $CaCoO_2N$ and $CaCu_{0.5}Co_{0.5}O_2N$, respectively. $CaCoO_2N$ exhibited the highest Jsc, indicating the highest photocurrent density among the investigated oxynitride nanoparticles under the applied measurement conditions. $CaCu_{0.5}Co_{0.5}O_2N$ showed an intermediate Jsc of 17.48 mA cm^{-2}, whereas $CaCuO_2N$ exhibited the lowest value of 12.99 mA cm^{-2}.

The open-circuit voltage values were 0.95, 0.67 and 0.87 V for $CaCuO_2N$, $CaCoO_2N$ and $CaCu_{0.5}Co_{0.5}O_2N$, respectively. $CaCuO_2N$ exhibited the highest Voc, followed by $CaCu_{0.5}Co_{0.5}O_2N$, while $CaCoO_2N$ showed the lowest value. The maximum current densities (Jmax) were 11.44, 25.26 and 15.12 mA cm^{-2},

and the corresponding maximum voltages (Vmax) were 0.80, 0.56 and 0.73 V, respectively.

The fill factor values were 0.739, 0.700 and 0.732 for $CaCuO_2N$, $CaCoO_2N$ and $CaCu_{0.5}Co_{0.5}O_2N$, respectively. $CaCuO_2N$ exhibited the highest FF, while $CaCoO_2N$ showed the lowest value. The relatively close FF values of $CaCuO_2N$ and $CaCu_{0.5}Co_{0.5}O_2N$ indicate similar characteristics of the J–V curves around their maximum-power points, whereas the lower FF of $CaCoO_2N$ indicates a comparatively lower degree of curve fill under the applied measurement conditions.

The power conversion efficiencies were reported as 9.19%, 14.37% and 11.154% for $CaCuO_2N$, $CaCoO_2N$ and $CaCu_{0.5}Co_{0.5}O_2N$, respectively. $CaCoO_2N$ exhibited the highest measured PCE of 14.37%, which is consistent with its substantially higher Jsc despite its lower Voc and FF. $CaCuO_2N$ exhibited the highest Voc and FF but a considerably lower Jsc, resulting in a PCE of 9.19%. $CaCu_{0.5}Co_{0.5}O_2N$ showed a higher Jsc than $CaCuO_2N$ and a relatively high Voc and FF, resulting in a PCE of 11.154%.

The J–V measurements demonstrate clear differences in the photovoltaic response of the Ca-based oxynitride nanomaterials. The variation in PCE is determined by the combined contribution of Jsc, Voc and FF. Under the applied measurement conditions, $CaCoO_2N$ exhibited the highest measured photovoltaic efficiency, while $CaCuO_2N$ exhibited the highest Voc and FF, and $CaCu_{0.5}Co_{0.5}O_2N$ showed an intermediate photovoltaic response.

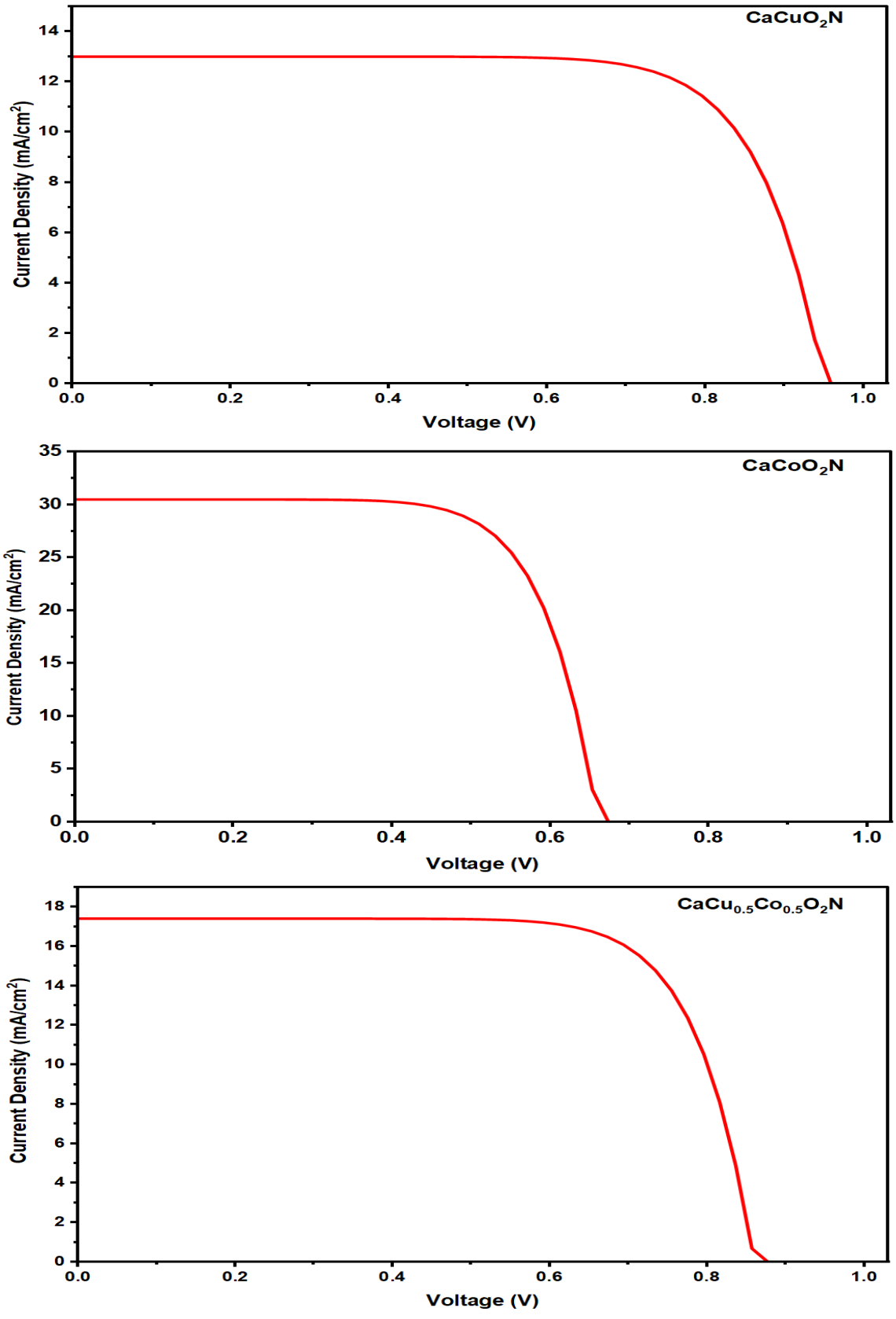


Fig. (3-30): J-V curves of $CaCuO_2N$, $CaCoO_2N$ and $CaCu_{0.5}Co_{0.5}O_2N$ oxynitride perovskites synthesized by the sol–gel Auto-Combustion technique.

Table (3-18): Parameters of $CaCuO_2N$, $CaCoO_2N$ and $CaCu_{0.5}Co_{0.5}O_2N$ solar cells.

Parameter	**$CaCuO_2N$**	**$CaCoO_2N$**	**$CaCu_{0.5}Co_{0.5}O_2N$**
Jsc (mA/cm²)	12.99	30.48	17.48
Voc (V)	0.95	0.67	0.87
Jmax (mA/cm²)	11.44	25.26	15.12
Vmax (V)	0.80	0.56	0.73
FF	0.739	0.700	0.732
PCE / Efficiency (%)	9.19%	14.37%	11.154

3.8.3 Mg-Based Oxynitride Perovskites

The photovoltaic characteristics of the Mg-based oxynitride nanoparticles were evaluated from current density–voltage (J–V) measurements, as shown in Fig. (3-31), and the corresponding photovoltaic parameters are summarized in Table (3-19). The J–V curves exhibit clear photovoltaic responses for $MgCuO_2N$, $MgCoO_2N$ and $MgCu_{0.5}Co_{0.5}O_2N$, with distinct values of short-circuit current density (Jsc), open-circuit voltage (Voc), maximum current density (Jmax), maximum voltage (Vmax), fill factor (FF) and power conversion efficiency (PCE).

The short-circuit current densities were 17.27, 27.27 and 11.83 mA cm^{-2} for $MgCuO_2N$, $MgCoO_2N$ and $MgCu_{0.5}Co_{0.5}O_2N$, respectively. $MgCoO_2N$ exhibited the highest Jsc, indicating the highest measured photocurrent density among the investigated Mg-based oxynitride nanoparticles. $MgCuO_2N$ showed an intermediate Jsc of 17.27 mA cm^{-2}, whereas $MgCu_{0.5}Co_{0.5}O_2N$ exhibited the lowest value of 11.83 mA cm^{-2}.

The open-circuit voltage values were 0.91, 0.73 and 0.96 V for $MgCuO_2N$, $MgCoO_2N$ and $MgCu_{0.5}Co_{0.5}O_2N$, respectively. $MgCu_{0.5}Co_{0.5}O_2N$ exhibited the highest Voc, followed by $MgCuO_2N$, while $MgCoO_2N$ showed the lowest value. The maximum current densities (Jmax) were 14.84, 23.29 and 10.10 mA cm^{-2},

while the corresponding maximum voltages (Vmax) were 0.78, 0.62 and 0.82 V, respectively.

The fill factor values were 0.732, 0.713 and 0.736 for $MgCuO_2N$, $MgCoO_2N$ and $MgCu_{0.5}Co_{0.5}O_2N$, respectively. $MgCu_{0.5}Co_{0.5}O_2N$ exhibited the highest FF, followed closely by $MgCuO_2N$, whereas $MgCoO_2N$ showed the lowest value. The relatively close FF values indicate comparable J–V curve characteristics around the maximum-power region, with $MgCu_{0.5}Co_{0.5}O_2N$ showing the highest measured FF.

The power conversion efficiencies were 11.59%, 14.51% and 8.44% for $MgCuO_2N$, $MgCoO_2N$ and $MgCu_{0.5}Co_{0.5}O_2N$, respectively. $MgCoO_2N$ exhibited the highest measured PCE of 14.51%, which is consistent with its substantially higher Jsc despite its lower Voc and FF. $MgCuO_2N$ showed a PCE of 11.59%, supported by its relatively high Jsc, Voc and FF. Although $MgCu_{0.5}Co_{0.5}O_2N$ exhibited the highest Voc and FF, its considerably lower Jsc resulted in the lowest PCE of 8.44%.

The J–V measurements demonstrate clear differences in the photovoltaic response of the Mg-based oxynitride nanomaterials. The measured photovoltaic efficiency is determined by the combined contribution of Jsc, Voc and FF. Under the applied measurement conditions, $MgCoO_2N$ exhibited the highest measured PCE, whereas $MgCu_{0.5}Co_{0.5}O_2N$ showed the highest Voc and FF but a lower Jsc.

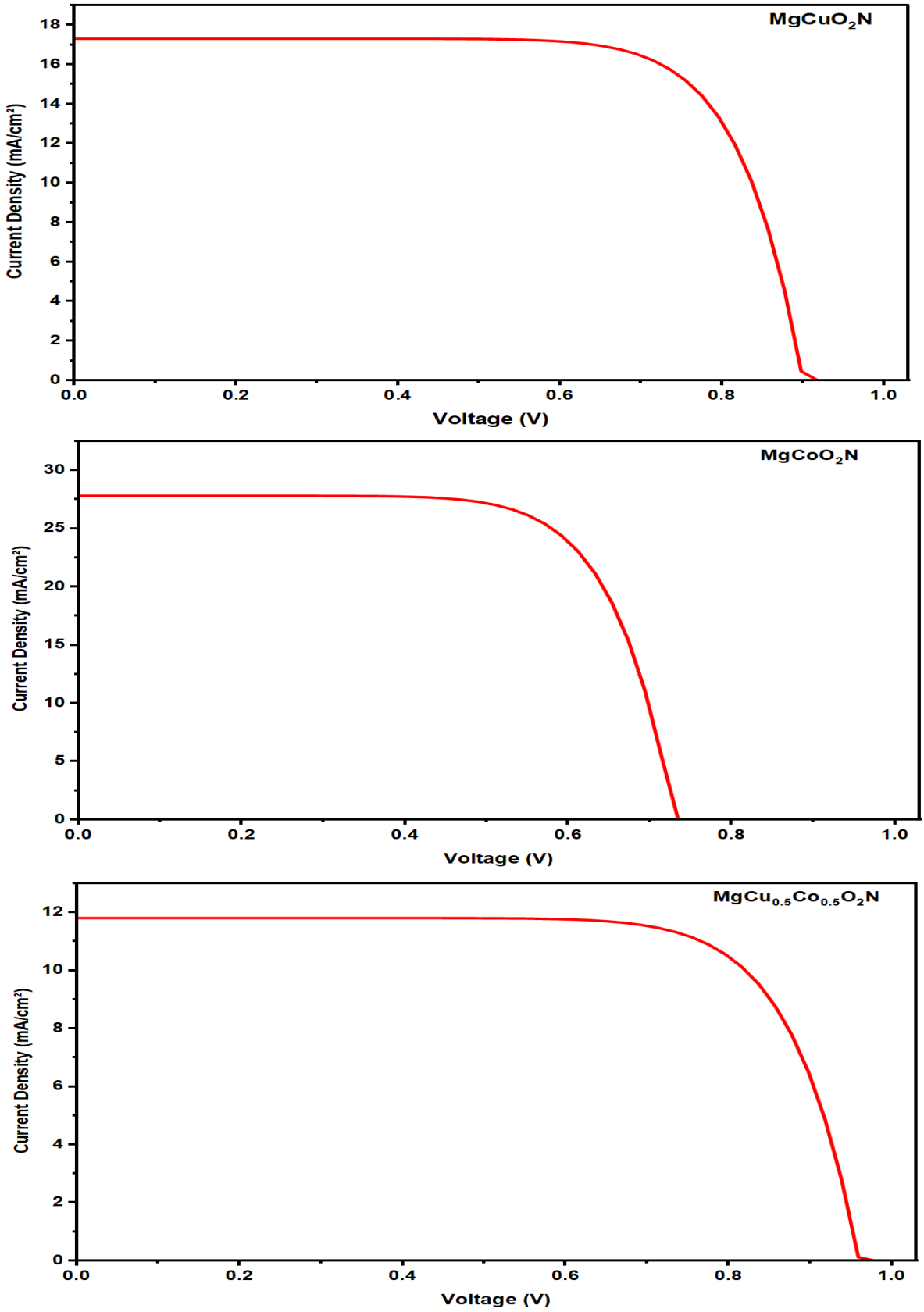


Fig. (3-31): J-V curves of $MgCuO_2N$, $MgCoO_2N$ and $MgCu_{0.5}Co_{0.5}O_2N$ oxynitride perovskites synthesized by the sol–gel Auto-Combustion technique.

Table (3-19): Parameters of $MgCuO_2N$, $MgCoO_2N$ and $MgCu_{0.5}Co_{0.5}O_2N$ solar cells.

Parameter	**$MgCuO_2N$**	**$MgCoO_2N$**	**$MgCu_{0.5}Co_{0.5}O_2N$**
Jsc (mA/cm^2)	17.27	27.27	11.83
Voc (V)	0.91	0.73	0.96
Jmax (mA/cm^2)	14.84	23.29	10.10
Vmax (V)	0.78	0.62	0.82
FF	0.732	0.713	0.736
PCE / Efficiency (%)	11.59%	14.51%	8.44%

3.8.4 Pb-Based Oxynitride Perovskites

The photovoltaic characteristics of the Pb-based oxynitride nanoparticles were evaluated from current density–voltage (J–V) measurements, as shown in Fig. (3-32), and the corresponding photovoltaic parameters are summarized in Table (3-20). The J–V curves show clear photovoltaic responses for $PbCuO_2N$, $PbCoO_2N$ and $PbCu_{0.5}Co_{0.5}O_2N$, with distinct values of short-circuit current density (Jsc), open-circuit voltage (Voc), maximum current density (Jmax), maximum voltage (Vmax), fill factor (FF) and power conversion efficiency (PCE).

The short-circuit current densities were 12.91, 23.90 and 24.70 mA cm^{-2} for $PbCuO_2N$, $PbCoO_2N$ and $PbCu_{0.5}Co_{0.5}O_2N$, respectively. $PbCu_{0.5}Co_{0.5}O_2N$ exhibited the highest Jsc, followed closely by $PbCoO_2N$, whereas $PbCuO_2N$ showed a substantially lower value. The higher Jsc values observed for $PbCoO_2N$ and $PbCu_{0.5}Co_{0.5}O_2N$ indicate higher photocurrent densities under the applied measurement conditions.

The open-circuit voltage values were 0.95, 0.79 and 0.83 V for $PbCuO_2N$, $PbCoO_2N$ and $PbCu_{0.5}Co_{0.5}O_2N$, respectively. $PbCuO_2N$ exhibited the highest Voc, while $PbCoO_2N$ showed the lowest value. The maximum current densities

(Jmax) were 11.08, 20.12 and 21.12 mA cm^{-2}, whereas the corresponding maximum voltages (Vmax) were 0.81, 0.67 and 0.71 V, respectively.

The fill factor values were 0.736, 0.708 and 0.729 for $PbCuO_2N$, $PbCoO_2N$ and $PbCu_{0.5}Co_{0.5}O_2N$, respectively. $PbCuO_2N$ exhibited the highest FF, followed by $PbCu_{0.5}Co_{0.5}O_2N$, while $PbCoO_2N$ showed the lowest value. The relatively close FF values indicate comparable J–V curve characteristics around the maximum-power region among the three oxynitride nanoparticles.

The power conversion efficiencies were 9.03%, 13.48% and 15.08% for $PbCuO_2N$, $PbCoO_2N$ and $PbCu_{0.5}Co_{0.5}O_2N$, respectively. $PbCu_{0.5}Co_{0.5}O_2N$ exhibited the highest measured PCE of 15.08%, which is associated with its highest Jsc together with a relatively high Voc and FF. $PbCoO_2N$ showed a PCE of 13.48%, supported by its high Jsc, although its Voc and FF were lower than those of $PbCuO_2N$. In contrast, $PbCuO_2N$ exhibited the highest Voc and FF but a substantially lower Jsc, resulting in the lowest PCE of 9.03%.

The J–V curves also show that $PbCuO_2N$ maintains a relatively high current density over a broad voltage range before a pronounced decrease near its open-circuit voltage. $PbCoO_2N$ and $PbCu_{0.5}Co_{0.5}O_2N$ show higher current densities and a corresponding decrease in current as the voltage approaches their respective Voc values. These features are consistent with the photovoltaic parameters obtained from the J–V measurements., The J–V measurements demonstrate clear differences in the photovoltaic response of the Pb-based oxynitride nanomaterials. The measured PCE is determined by the combined contribution of Jsc, Voc and FF. Under the applied measurement conditions, $PbCu_{0.5}Co_{0.5}O_2N$ exhibited the highest measured PCE, while $PbCuO_2N$ exhibited the highest Voc and FF.

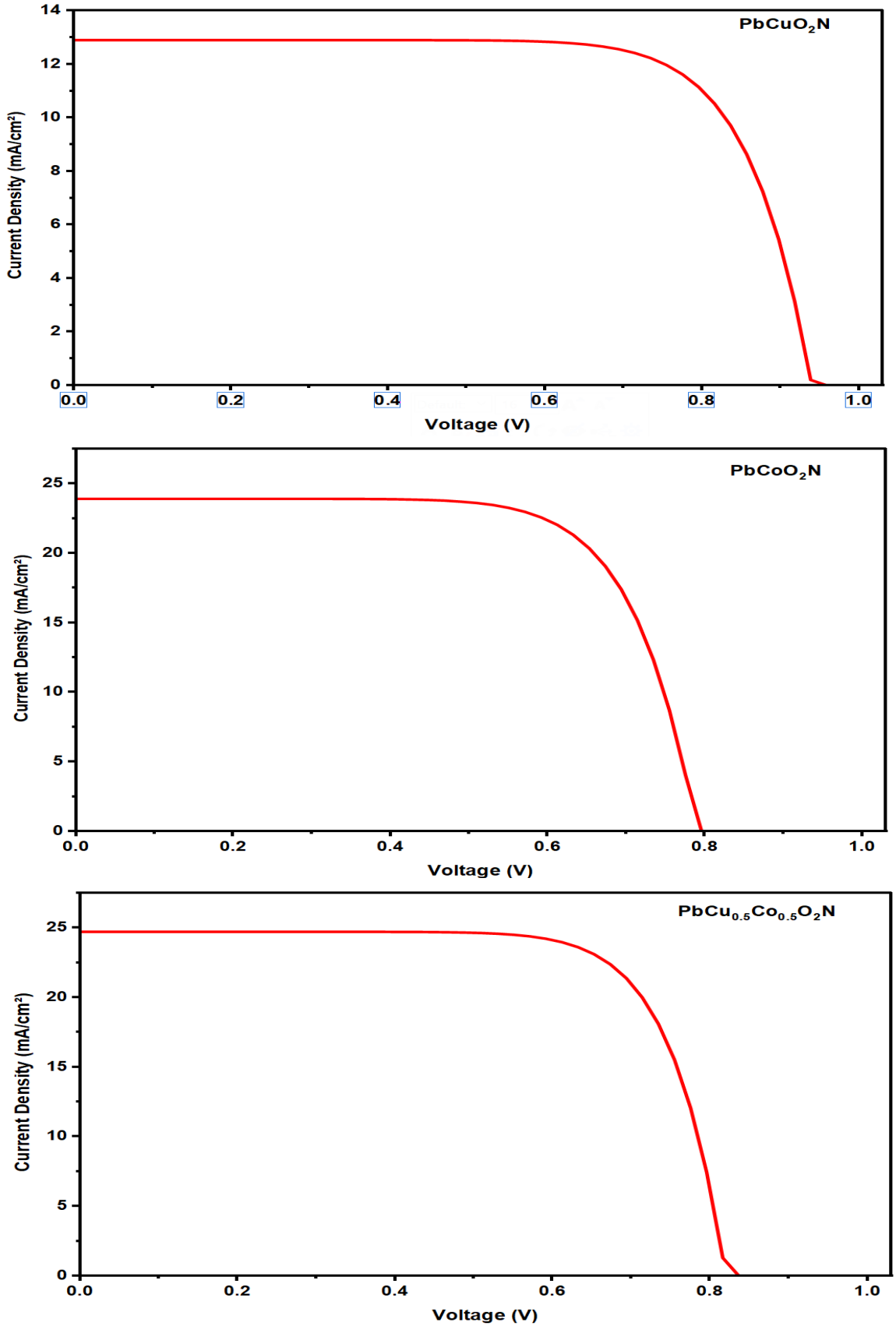


Fig. (3-32): J-V curves of $PbCuO_2N$, $PbCoO_2N$ and $PbCu_{0.5}Co_{0.5}O_2N$ oxynitride perovskites synthesized by the sol–gel technique.

Table (3-20): Parameters of $PbCuO_2N$, $PbCoO_2N$ and $PbCu_{0.5}Co_{0.5}O_2N$ solar cells.

Parameter	**$PbCuO_2N$**	**$PbCoO_2N$**	**$PbCu_{0.5}Co_{0.5}O_2N$**
Jsc (mA/cm^2)	12.91	23.90	24.70
Voc (V)	0.95	0.79	0.83
Jmax (mA/cm^2)	11.08	20.12	21.12
Vmax (V)	0.81	0.67	0.71
FF	0.736	0.708	0.729
PCE / Efficiency (%)	9.03%	13.48%	15.08%

3.9 Conclusions

1. Twelve transition-metal oxynitride nanomaterials based on Ba, Ca, Mg, and Pb at the A-site, with Cu, Co, or equimolar Cu/Co at the B-site, were successfully synthesized by the sol–gel method and characterized using XRD, FESEM–EDS, AFM, FTIR, UV–Vis, TGA/DTG, Hall effect, and solar-cell applications.
2. XRD revealed composition-dependent crystal structures and lattice characteristics, while FESEM–EDS confirmed the nanoscale morphology and the presence of the constituent elements. AFM showed variations in surface topography and roughness with composition.
3. FTIR exhibited characteristic vibrational features of the metal–anion framework, whereas UV–Vis measurements demonstrated composition-dependent optical behavior. For the Ba-based materials, the optical band gaps were 2.77 eV for $BaCuO_2N$, 2.04 eV for $BaCoO_2N$, and 1.63 eV for $BaCu_{0.5}Co_{0.5}O_2N$.
4. TGA/DTG showed limited mass changes and composition-dependent kinetic and thermodynamic parameters. The highest activation energy in the Ca-based series was obtained for $CaCu_{0.5}Co_{0.5}O_2N$ (307.9 kJ/mol).
5. Hall-effect measurements indicated p-type semiconducting behavior, with variations in conductivity, carrier concentration, and mobility. $MgCu_{0.5}Co_{0.5}O_2N$ showed the highest conductivity within the Mg-based series, reaching 1.19×10^{-3} $S \cdot cm^{-1}$.
6. Solar-cell applications demonstrated composition-dependent photovoltaic performance. $BaCoO_2N$ exhibited the highest measured PCE of 15.77%, while $PbCu_{0.5}Co_{0.5}O_2N$ reached 15.08% within the Pb-based series.
7. Overall, the results demonstrate that A-site selection and B-site Cu/Co composition are associated with variations in the structural, morphological,

optical, thermal, electrical, and photovoltaic properties of the prepared oxynitride nanomaterials.

3.10 Recommendations

1. Conduct broader future studies on the relationship between composition and properties of transition-metal perovskite oxynitrides.
2. Continue investigating the functional properties of these materials to further understand their behavior in different applications.
3. Expand the evaluation of the long-term stability and performance of the prepared materials in energy-related applications.

3.11 References

[1] G. K. Singh, “Solar power generation by PV (photovoltaic) technology: A review,” Energy, vol. 53, pp. 1–13, 2013.

[2] A. Mdallal, A. Yasin, M. Mahmoud, M. A. Abdelkareem, A. H. Alami, and A. G. Olabi, “A comprehensive review on solar photovoltaics: Navigating generational shifts, innovations, and sustainability,” Sustain. Horizons, vol. 13, no. February, p. 100137, 2025, doi: 10.1016/j.horiz.2025.100137.

[3] “Cell-Efficiency @ Www.Nrel.Gov.” [Online]. Available: https://www.nrel.gov/pv/cell-efficiency.html

[4] “silicon-perovskite-tandem-solar-cells-new-world-efficiency @ www.longi.com.” [Online]. Available: https://www.longi.com/en/news/silicon-perovskite-tandem-solar-cells-new-world-efficiency/

[5] C. Yang et al., “Achievements, challenges, and future prospects for industrialization of perovskite solar cells,” Light Sci. Appl., vol. 13, no. 1, p. 227, 2024.

[6] A. Rothwarf and K. W. Böer, “Direct conversion of solar energy through photovoltaic cells,” Prog. Solid State Chem., vol. 10, pp. 71–102, 1975.

[7] W. W. Anderson and Y. G. Chai, “Becquerel effect solar cell,” Energy Convers., vol. 15, no. 3–4, pp. 85–94, 1976.

[8] S. Kumar, “Solar photovoltaic cell: History, working principle, and landscape,” in Photovoltaic Modules, CRC Press, 2025, pp. 3–46.

[9] C. Charbonneau et al., “Rapid radiative platinisation for dye-sensitised solar cell counter electrodes,” Prog. Photovoltaics Res. Appl., vol. 22, no. 12, pp. 1267–1272, 2014.

[10] J. M. Choi et al., “Modified laser-fired contact process for efficient PERC solar cells,” Prog. Photovoltaics Res. Appl., vol. 27, no. 12, pp. 1092–1103, 2019.

[11] O. Schmidt, A. Hawkes, A. Gambhir, and I. Staffell, “The future cost of electrical energy storage based on experience rates,” Nat. Energy, vol. 2, no. 8, p. 17110, 2017.

[12] K. A. W. Horowitz, B. Palmintier, B. Mather, and P. Denholm, “Distribution system costs associated with the deployment of photovoltaic systems,” Renew. Sustain. Energy Rev., vol. 90, pp. 420–433, 2018.

[13] D. Yan et al., “Silicon solar cells with passivating contacts: Classification and performance,” Prog. Photovoltaics Res. Appl., vol. 31, no. 4, pp. 310–326, 2023.

[14] C.-R. Lee and L.-J. Chen, “Polyvinylbutyral assisted synthesis and characterization of kesterite quaternary semiconductor Cu2ZnSnSe4 nanofibers by electrospinning route,” Sol. Energy Mater. Sol. Cells, vol. 151, pp. 24–29, 2016.

[15] A. Khatibi, F. Razi Astaraei, and M. H. Ahmadi, “Generation and combination of the solar cells: A current model review,” Energy Sci. Eng., vol. 7, no. 2, pp. 305–322, 2019.

[16] M. M. A. Moon, M. F. Rahman, J. Hossain, and A. B. M. Ismail, “Comparative study of the second generation a-Si: H, CdTe, and CIGS thin-film solar cells,” Adv. Mater. Res., vol. 1154, pp. 102–111, 2019.

[17] O. Vigil-Galán et al., “Route towards low cost-high efficiency second generation solar cells: current status and perspectives,” J. Mater. Sci. Mater. Electron., vol. 26, no. 8, pp. 5562–5573, 2015.

[18] G. F. Brown and J. Wu, “Third generation photovoltaics,” Laser Photon. Rev., vol. 3, no. 4, pp. 394–405, 2009.

[19] M. A. Green, “Third generation photovoltaics: solar cells for 2020 and beyond,” Phys. E Low-dimensional Syst. Nanostructures, vol. 14, no. 1–2, pp. 65–70, 2002.

[20] Y. Rong et al., “Challenges for commercializing perovskite solar cells,” Science (80-.)., vol. 361, no. 6408, p. eaat8235, 2018.

[21] M. K. Hossain et al., “An extensive study on multiple ETL and HTL layers to design and simulation of high-performance lead-free CsSnCl3-based perovskite solar cells,” Sci. Rep., vol. 13, no. 1, p. 2521, 2023.

[22] R. Wang, M. Mujahid, Y. Duan, Z. Wang, J. Xue, and Y. Yang, “A review of perovskites solar cell stability,” Adv. Funct. Mater., vol. 29, no. 47, p. 1808843, 2019.

[23] S. S. Shin, S. J. Lee, and S. Il Seok, “Metal oxide charge transport layers for efficient and stable perovskite solar cells,” Adv. Funct. Mater., vol. 29, no. 47, p. 1900455, 2019.

[24] “Perovskite Solar Cells Explained Simply (Beginner’s Guide).” Accessed: May 07, 2026. [Online]. Available: https://ecoenergytips.com/perovskite-solar-cells-explained/

[25] L. A. Kolahalam, I. V. K. Viswanath, B. S. Diwakar, B. Govindh, V. Reddy, and Y. L. N. Murthy, “Review on nanomaterials: Synthesis and applications,” Mater. Today Proc., vol. 18, pp. 2182–2190, 2019.

[26] N. Baig, I. Kammakakam, and W. Falath, “Nanomaterials: A review of synthesis methods, properties, recent progress, and challenges,” Mater. Adv., vol. 2, no. 6, pp. 1821–1871, 2021.

[27] S. K. Kulkarni and S. K. Kulkarni, Nanotechnology: principles and practices. Springer, 2015.

[28] N. INITIATIVE, “THE NATIONAL NANOTECHNOLOGY INITIATIVE”.

[29] Paras et al., “A review on low-dimensional nanomaterials: nanofabrication, characterization and applications,” Nanomaterials, vol. 13, no. 1, p. 160, 2022.

[30] Z. S. Qian, X. Y. Shan, L. J. Chai, J. J. Ma, J. R. Chen, and H. Feng, “DNA nanosensor based on biocompatible graphene quantum dots and carbon nanotubes,” Biosens. Bioelectron., vol. 60, pp. 64–70, 2014.

[31] S. Pandit, P. Behera, J. Sahoo, and M. De, “In situ synthesis of amino acid functionalized carbon dots with tunable properties and their biological applications,” ACS Appl. Bio Mater., vol. 2, no. 8, pp. 3393–3403, 2019.

[32] A. Barberis et al., “Simultaneous amperometric detection of ascorbic acid and antioxidant capacity in orange, blueberry and kiwi juice, by a telemetric system coupled with a fullerene-or nanotubes-modified ascorbate subtractive biosensor,” Biosens. Bioelectron., vol. 67, pp. 214–223, 2015.

[33] C. J. T. Robidillo et al., “Ratiometric detection of nerve agents by coupling complementary properties of silicon-based quantum dots and green fluorescent protein,” ACS Appl. Mater. Interfaces, vol. 11, no. 36, pp. 33478–33488, 2019.

[34] V. A. Bragina, S. L. Znoyko, A. V Orlov, A. V Pushkarev, M. P. Nikitin, and P. I. Nikitin, “Analytical platform with selectable assay parameters based on three functions of magnetic nanoparticles: demonstration of highly sensitive rapid quantitation of staphylococcal enterotoxin B in Food,” Anal. Chem., vol. 91, no. 15, pp. 9852–9857, 2019.

[35] C.-T. Yang et al., “Exploiting surface-plasmon-enhanced light scattering for the design of ultrasensitive biosensing modality,” Anal. Chem., vol. 88, no. 23, pp. 11924–11930, 2016.

[36] Y. Gu et al., “Electrochemiluminescence sensor based on upconversion

nanoparticles and oligoaniline-crosslinked gold nanoparticles imprinting recognition sites for the determination of dopamine," Biosens. Bioelectron., vol. 128, pp. 129–136, 2019.

[37] J. Ou, H. Tan, Z. Chen, and X. Chen, "FRET-based semiconducting polymer dots for pH sensing," Sensors, vol. 19, no. 6, p. 1455, 2019.

[38] Y.-F. Li, J. Feng, and H.-B. Sun, "Perovskite quantum dots for light-emitting devices," Nanoscale, vol. 11, no. 41, pp. 19119–19139, 2019.

[39] M. Kuno, "Introductory nanoscience: Physical and chemical concepts," MRS Bull., vol. 37, no. 2, pp. 169–170, 2012.

[40] S. Seth and P. Rathinasabapathi, "A short review on detection of antibiotics in milk using nanomaterial-based biosensor," Food Anal. Methods, vol. 15, no. 8, pp. 2181–2192, 2022.

[41] B. Maleki et al., "Synthesis and characterization of nanorod magnetic Co–Fe mixed oxides and its catalytic behavior towards one-pot synthesis of polysubstituted pyridine derivatives," Polycycl. Aromat. Compd., vol. 40, no. 3, pp. 633–643, 2020.

[42] V. V. Mitin, D. I. Sementsov, and N. Z. Vagidov, Quantum mechanics for nanostructures. Cambridge University Press, 2010.

[43] C. Verma, E. Berdimurodov, D. K. Verma, K. Berdimuradov, A. Alfantazi, and C. M. Hussain, "3D Nanomaterials: The future of industrial, biological, and environmental applications," Inorg. Chem. Commun., vol. 156, p. 111163, 2023.

[44] A. M. Díez-Pascual, "Carbon-based nanomaterials," 2021, MDPI.

[45] L. Wang, C. Hu, and L. Shao, "The antimicrobial activity of nanoparticles: present situation and prospects for the future," Int. J. Nanomedicine, pp. 1227–1249, 2017.

[46] P. Kesharwani, K. Jain, and N. K. Jain, "Dendrimer as nanocarrier for drug delivery," Prog. Polym. Sci., vol. 39, no. 2, pp. 268–307, 2014.

[47] T. W. Clyne and D. Hull, An introduction to composite materials. Cambridge university press, 2019.

[48] O. G. Coronado et al., "Functionalized Nanomaterials in Cancer Treatment : A Review," pp. 1–25, 2025.

[49] D. Bokov et al., "Nanomaterial by sol-gel method: synthesis and application," Adv. Mater. Sci. Eng., vol. 2021, no. 1, p. 5102014, 2021.

[50] M. Sabzi et al., “A review on sustainable manufacturing of ceramic-based thin films by chemical vapor deposition (CVD): reactions kinetics and the deposition mechanisms,” Coatings, vol. 13, no. 1, p. 188, 2023.

[51] B. Nahar, S. B. Chaity, M. A. Gafur, and M. Z. Hossain, “Synthesis of spherical copper oxide nanoparticles by chemical precipitation method and investigation of their photocatalytic and antibacterial activities,” J. Nanomater., vol. 2023, no. 1, p. 2892081, 2023.

[52] P. G. Jamkhande, N. W. Ghule, A. H. Bamer, and M. G. Kalaskar, “Metal nanoparticles synthesis: An overview on methods of preparation, advantages and disadvantages, and applications,” J. Drug Deliv. Sci. Technol., vol. 53, p. 101174, 2019.

[53] Y. X. Gan, A. H. Jayatissa, Z. Yu, X. Chen, and M. Li, “Hydrothermal synthesis of nanomaterials,” J. Nanomater., vol. 2020, 2020.

[54] R. D’Amato et al., “Synthesis of ceramic nanoparticles by laser pyrolysis: From research to applications,” J. Anal. Appl. Pyrolysis, vol. 104, pp. 461–469, 2013.

[55] S. A. M. Ealia and M. P. Saravanakumar, “A review on the classification, characterisation, synthesis of nanoparticles and their application,” in IOP conference series: materials science and engineering, IOP Publishing, 2017, p. 32019.

[56] T. Shahwan et al., “Green synthesis of iron nanoparticles and their application as a Fenton-like catalyst for the degradation of aqueous cationic and anionic dyes,” Chem. Eng. J., vol. 172, no. 1, pp. 258–266, 2011.

[57] D. L. Zhang, “Processing of advanced materials using high-energy mechanical milling,” Prog. Mater. Sci., vol. 49, no. 3–4, pp. 537–560, 2004.

[58] R. E. Russo, X. L. Mao, J. Yoo, and J. J. Gonzalez, “Laser ablation,” in Laser-induced breakdown spectroscopy, Elsevier, 2007, pp. 41–70.

[59] A. Gavali, J. Rodrigues, N. Shimpi, and P. Badani, Chapter 2 An Overview of the Synthesis of Nanomaterials, vol. 145. 2023.

[60] H. Ye, “Electrical Characterization of GaN: Si and AlGaN: Si,” 2011.

[61] N. Balkan and A. Erol, “Intrinsic and extrinsic semiconductors,” in Semiconductors for Optoelectronics: Basics and Applications, Springer, 2021, pp. 37–78.

[62] S. M. S. K. K. NG, Physics Of Semiconductor Devices 3rd Edition.

[63] B. G. Streetman and S. K. Banerjee, Solid State Electronic Devices.

[64] X. Zhao, H. Zhang, J. Zhang, J. Liu, M. Lei, and L. Jiang, “Organic Semiconductor Single Crystals for Electronics and Photonics,” Adv. Sci., vol. 10, no. 15, p. 2300483, 2023.

[65] H. J. Möller, H. P. Strunk, and J. H. Werner, Polycrystalline Semiconductors: Grain Boundaries and Interfaces. Springer Science & Business Media, 2012.

[66] J. Wen et al., “Copper-based perovskites and perovskite-like halides: A review from the perspective of molecular level,” Nano Energy, vol. 128, p. 109802, 2024.

[67] B. Raveau and M. Seikh, Cobalt oxides: from crystal chemistry to physics. John Wiley & Sons, 2012.

[68] J. Epp, “X-ray diffraction (XRD) techniques for materials characterization,” in Materials characterization using nondestructive evaluation (NDE) methods, Elsevier, 2016, pp. 81–124.

[69] C. J. Humphreys, “The significance of Bragg’s law in electron diffraction and microscopy, and Bragg’s second law,” Found. Crystallogr., vol. 69, no. 1, pp. 45–50, 2013.

[70] S. Fatimah, R. Ragadhita, D. F. Al Husaeni, and A. B. D. Nandiyanto, “How to calculate crystallite size from x-ray diffraction (XRD) using Scherrer method,” ASEAN J. Sci. Eng., vol. 2, no. 1, pp. 65–76, 2022.

[71] P. Gnanamoorthy, V. Karthikeyan, and V. A. Prabu, “Field Emission Scanning Electron Microscopy (FESEM) characterisation of the porous silica nanoparticulate structure of marine diatoms,” J. Porous Mater., vol. 21, no. 2, pp. 225–233, 2014.

[72] V.-D. Hodoroaba, “Energy-dispersive X-ray spectroscopy (EDS),” in Characterization of nanoparticles, Elsevier, 2020, pp. 397–417.

[73] A. M. Joshua, G. Cheng, and E. V Lau, “Soft matter analysis via atomic force microscopy (AFM): A review,” Appl. Surf. Sci. Adv., vol. 17, p. 100448, 2023.

[74] H. Park et al., “Observation of fractionally quantized anomalous Hall effect,” Nature, vol. 622, no. 7981, pp. 74–79, 2023.

[75] Y. Kobayashi, Y. Tsujimoto, and H. Kageyama, “Property engineering in perovskites via modification of anion chemistry,” Annu. Rev. Mater. Res., vol. 48, no. 1, pp. 303–326, 2018.

[76] M. P. Ravikumar et al., “Mixed-Anion Band Engineered Cobalt Oxynitride

for Efficient Solar Water Splitting and Nitrogen Fixation," Energy & Fuels, vol. 39, no. 42, pp. 20647–20662, 2025.

[77] A. Hosono, Y. Masubuchi, T. Endo, and S. Kikkawa, "Molten BaCN 2 for the sintering and crystal growth of dielectric oxynitride perovskites Sr 1− x Ba x TaO 2 N (x= 0.04–0.23)," Dalt. Trans., vol. 46, no. 48, pp. 16837–16844, 2017.

[78] F. Haydous et al., "Oxynitride thin films versus particle-based photoanodes: a comparative study for photoelectrochemical solar water splitting," ACS Appl. Energy Mater., vol. 2, no. 1, pp. 754–763, 2019.

[79] X. Xu and H. Jiang, "Anion order in perovskite oxynitrides AMO 2 N (A= Ba, Sr, Ca; M= Ta, Nb): a first-principles based investigation," RSC Adv., vol. 10, no. 41, pp. 24410–24418, 2020.

[80] T. Wakasugi, Y. Hirose, S. Nakao, Y. Sugisawa, D. Sekiba, and T. Hasegawa, "High-quality heteroepitaxial growth of thin films of the perovskite oxynitride CaTaO2N: importance of interfacial symmetry matching between films and substrates," ACS omega, vol. 5, no. 22, pp. 13396–13402, 2020.

[81] C. Bubeck et al., "Observation of a possible diluted ferromagnetism above room temperature in cobalt-substituted LaTa (O, N) 3-d," arXiv Prepr. arXiv2003.14259, 2020.

[82] T. Sakata, R. Yoshiyuki, S. Urushidani, N. Tarutani, K. Katagiri, and K. Inumaru, "Ammonia-free synthesis and color tuning of oxynitride perovskite SrTaO2N-SrTiO3 solid solution by using alkoxide-derived Ta-Ti binary oxide gel precursors," J. Sol-Gel Sci. Technol., vol. 104, no. 3, pp. 685–693, 2022.

[83] J. Seo and K. Domen, "Perovskite and layered perovskite oxynitrides for efficient sunlight-driven artificial synthesis," Mater. Chem. Front., vol. 8, no. 6, pp. 1451–1479, 2024.

[84] A. Mohammadi et al., "Copper-perovskite interfacial engineering to boost deNOx activity," Chem. Eng. J., vol. 498, p. 155425, 2024.

[85] S. Nqayi and B. Sondezi, "B-Site Cu2+ Substitution and Strain-Mediated Magnetic Evolution in La2CoRuO6 Double Perovskite: Insights from Experiment and DFT+ U-Corrected Calculations," ACS Appl. Mater. Interfaces, vol. 17, no. 51, p. 69610, 2025.

[86] Y.-I. Kim, P. M. Woodward, K. Z. Baba-Kishi, and C. W. Tai, "Characterization of the structural, optical, and dielectric properties of oxynitride perovskites AMO2N (A= Ba, Sr, Ca; M= Ta, Nb)," Chem.

Mater., vol. 16, no. 7, pp. 1267–1276, 2004.

[87] M. Yang, J. Oró-Solé, J. A. Rodgers, A. B. Jorge, A. Fuertes, and J. P. Attfield, “Anion order in perovskite oxynitrides,” Nat. Chem., vol. 3, no. 1, pp. 47–52, 2011.

[88] X. Wang, B. Jiang, Y. Zhang, Y.-I. Kim, and K. Page, “Influence of cation size on the local atomic structure and electronic properties of Ta perovskite oxynitrides,” Inorg. Chem., vol. 60, no. 18, pp. 14190–14201, 2021.

[89] S. Trolier-McKinstry, H. Hu, S. B. Krupanidhi, P. Chindaudom, K. Vedam, and R. E. Newnham, “Spectroscopic ellipsometry studies on ion beam sputter deposited Pb (Zr, Ti) O3 films on sapphire and Pt-coated silicon substrates,” Thin Solid Films, vol. 230, no. 1, pp. 15–27, 1993.

[90] M. Hojamberdiev, R. Vargas, F. Zhang, K. Teshima, and M. Lerch, “Perovskite BaTaO2N: from materials synthesis to solar water splitting,” Adv. Sci., vol. 10, no. 33, p. 2305179, 2023.

[91] S. G. Ebbinghaus, H.-P. Abicht, R. Dronskowski, T. Müller, A. Reller, and A. Weidenkaff, “Perovskite-related oxynitrides–Recent developments in synthesis, characterisation and investigations of physical properties,” Prog. Solid State Chem., vol. 37, no. 2–3, pp. 173–205, 2009.

[92] K. D. Salman, H. H. Abbas, and H. A. Aljawad, “Synthesis and characterization of MgO nanoparticle via microwave and sol-gel methods,” in Journal of physics: conference series, IOP Publishing, 2021, p. 12104.

[93] K. Moorthi, B. Sivakumar, B. Chokkiah, H. Valdes, and S. Mohan, “Morphological impact of perovskite-structured lanthanum cobalt oxide (LaCoO3) nanoflakes toward supercapacitor applications,” ACS Appl. Nano Mater., vol. 7, no. 16, pp. 18511–18522, 2024.

[94] B. N. J. Persson, “On the use of surface roughness parameters,” Tribol. Lett., vol. 71, no. 2, p. 29, 2023.

[95] B. Bhushan, “Surface roughness analysis and measurement techniques,” in Modern tribology handbook, two volume set, CRC press, 2000, pp. 79–150.

[96] V. Alar, A. Razumić, B. Runje, I. Stojanović, M. Kurtela, and B. Štrbac, “Application of areal topography parameters in surface characterization,” Appl. Sci., vol. 15, no. 12, p. 6573, 2025.

[97] P. Innocenzi, “Sol-gel processing for advanced ceramics, a perspective,” Open Ceram., vol. 16, p. 100477, 2023.

[98] X. G. Tang, A. L. Ding, and W. G. Luo, “Surface morphology and chemical

states of highly oriented PbZrO3 thin films prepared by a sol–gel process," Appl. Surf. Sci., vol. 174, no. 2, pp. 148–154, 2001.

[99] E. Haye, V. Pierron, S. Barrat, F. Capon, F. Munnik, and S. Bruyère, "Nitrogen redistribution in annealed LaFeOxNy thin films investigated by FTIR spectroscopy and EELS mapping," Appl. Surf. Sci., vol. 427, pp. 1041–1045, 2018.

[100] M. E. Sweers et al., "Synthesis and symmetry of perovskite oxynitride CaW (O, N) 3," Mater. Horizons, vol. 11, no. 17, pp. 4104–4114, 2024.

[101] K. Nakamoto, Infrared and Raman spectra of inorganic and coordination compounds, part B: applications in coordination, organometallic, and bioinorganic chemistry. John Wiley & Sons, 2009.

[102] A. E. Lavat and E. J. Baran, "IR-spectroscopic characterization of A2BB′ O6 perovskites," Vib. Spectrosc., vol. 32, no. 2, pp. 167–174, 2003.

[103] A. R. West, Solid state chemistry and its applications. John Wiley & Sons, 2022.

[104] G. Socrates, Infrared and Raman characteristic group frequencies: tables and charts. John Wiley & Sons, 2004.

الخلاصة

هدفت هذه الدراسة إلى تحضير وتوصيف اثني عشر مادة نانوية من أكاسيد النتريد للمعادن الانتقالية، تعتمد على Ba و Ca و Mg و Pb في الموقعA ، مع Cu أو Co أو مزيج متكافئ مولياً من Cu/Co في الموقع B، باستخدام طريقة السول–جل. تم توصيف المواد المحضرة باستخدام حيود الأشعة السينية (XRD) ، والمجهر الإلكتروني الماسح ذي الانبعاث الحقلي المقترن بمطيافية الأشعة السينية المشتتة للطاقة (FESEM–EDS)، ومجهر القوة الذرية (AFM) ، ومطيافية الأشعة تحت الحمراء بتحويل فورييه (FTIR)، ومطيافية الأشعة فوق البنفسجية–المرئية(UV–Vis) ، والتحليل الوزني الحراري المقترن بالتحليل الوزني الحراري التفاضلي (TGA/DTG) ، وقياسات تأثير هول، وقياسات كثافة التيار–الجهد (J–V). أظهرت النتائج أن الخواص التركيبية والمورفولوجية والبصرية والحرارية والكهربائية والفوتوفولطية تأثرت بشكل واضح بتركيب الموقعين A و B. أظهر تحليل XRD أعلى نسبة تبلور للمركب $PbCoO_2N$ بلغت (88.81%)، وأدنى نسبة تبلور للمركب $BaCu_{0.5}Co_{0.5}O_2N$ بلغت (64.1%)، مع أحجام جسيمات نانوية. وأظهرت تحاليل UV–Vis أن فجوة الطاقة البصرية تراوحت بين 1.63 و3.25eV ، في حين كشف تحليل TGA/DTG عن سلوك حراري يعتمد على تركيب المادة، مع تسجيل أعلى طاقة تنشيط للمركب$MgCuO_2N$ ، إذ بلغت kJ/mol.362.19 أكدت قياسات تأثير هول أن جميع المواد أظهرت سلوكاً من النوع الموجب(p-type) ، حيث سجل المركب $BaCoO_2N$ أعلى توصيلية كهربائية بلغت $S\cdot cm^{-1}$8.05 ، في حين أظهر المركب $MgCu_{0.5}Co_{0.5}O_2N$ أعلى حركة لحوامل الشحنة بلغت 4.85 × 10^3 . $cm^2\cdot V^{-1}\cdot s^{-1}$ وأظهرت القياسات الفوتوفولطية أن كفاءة التحويل تراوحت بين 8.44 و15.77%. وقد حقق المركب $BaCoO_2N$ أعلى كفاءة بلغت 15.77%، إلى جانب توصيلية كهربائية مرتفعة، مما يجعله المادة الأكثر ملاءمة للتطبيق الفوتوفولطي المدروس. في المقابل، سجل المركب $MgCu_{0.5}Co_{0.5}O_2N$ أدنى كفاءة بلغت 8.44%، وأدنى كثافة تيار قصر بلغت 11.83 mA/cm^2. كما أظهر المركب $PbCu_{0.5}Co_{0.5}O_2N$ أداءً فوتوفولطياً مرتفعاً، إذ بلغت كفاءته 15.08%. وبصورة عامة، أظهرت النتائج أن التحكم في كاتيون الموقع A ونسبة Cu/Co في الموقع B يُعد وسيلة فعالة للتحكم في الخواص والأداء الفوتوفولطي للمواد النانوية من أكاسيد النتريد للمعادن الانتقالية.

جمهورية العراق
وزارة التعليم العالي والبحث العلمي
جامعة القادسية
كلية العلوم
قسم الكيمياء

تخليق وتشخيص بيروفسكيتات أكاسيد-نتريدات المعادن الانتقالية الجديدة لتطبيقات الخلايا الشمسية

رسالة

مقدمة إلى مجلس كلية العلوم /جامعة القادسية وهي جزء من متطلبات نيل درجة الماجستير في علوم الكيمياء

من قبل

زهراء علي رحمن عبيس

(BSc. Chemistry, 2021)

بإشراف

الأستاذ الدكتور أحمد كاظم الصفار

٢٠٢٦ م ١٤٤٨ هـ